공학박사 학위논문

# Design and fabrication of unconventional soft materials for implantable medical and optoelectronic devices

**2017년 2월**

삽입형 의료 장치 및 광전자 소자를 위한

차세대 유연 물질의 설계와 제작


서울대학교 대학원

화학생물공학부 에너지환경화학융합기술전공

이 종 하

# Design and fabrication of unconventional soft materials for implantable medical and optoelectronic devices

지도 교수 김 대 형

이 논문을 공학박사 학위논문으로 제출함
**2017 년 1 월**

서울대학교 대학원
화학생물공학부 에너지환경화학융합기술전공
이 종 하

이종하의 공학박사 학위논문을 인준함
**2017 년 1 월**

위 원 장 _____ (인)

부위원장 _____ (인)

위 원 _____ (인)

위 원 _____ (인)

위 원 _____ (인)

# Abstract

# Design and fabrication of unconventional soft materials for implantable medical and optoelectronic devices

Jongha Lee

School of Chemical and Biological Engineering

Chemical Convergence for Energy & Environment

The Graduate School

Seoul National University

Soft electronics provide new opportunities on biomedical devices and optoelectronic devices since they offer flexible and conformable mechanical properties. Compared to commercialized rigid electronics, the soft electronics enables more accurate sensing from the curvilinear biological interface and tunable light incidence for optoelectronics. In this thesis, fabrication and application of soft medical devices and unconventional optoelectronic devices are developed based on the design and synthesis of

bioresorbable and perovskite materials.

Firstly, soft bioresorbable medical devices are designed and fabricated, which provide novel therapeutic guideline to overcome many challenges remaining for the treatment of glioblastoma. The integrated bioresorbable devices are composed of wireless heater, wireless temperature sensor and synthesized bioresorbable drug reservoir conformally adhered to the brain tissue provides localized, highly penetrative and controllable intracranial drug delivery.

Based on the fabrication technique of bioresorbable materials, transient memory system is proposed and developed, which shows fast and complete chemical destruction of stored data by wide-range optical stimulation. The system can be established by the integration of transient ultrathin resistive random access memory (RRAM) with multi-dye-sensitized upconverting nanoparticles (UCNPs) and provides new opportunities in mobile and defense application.

The final goal of this study is high-definition patterning of inorganic-organic hybrid perovskite thin films which have attracted great attention since it is regarded as an alternative to silicon in the optoelectronic devices. A new method so called “Spin-on-patterning (SoP)” enables the patterning of perovskite thin film which has hardly been accomplished due to their

extreme instability in solvents like bioresorbable materials. The patterned perovskite photodiode is fabricated and has potential for future ultrathin image sensor array.

**Keywords: flexible, electronics, bioresorbable, medical, transient, perovskite**

**Student Number: 2012-31300**

# Contents

**Abstract** ..... i

**Contents** ..... iv

**List of Figures** ..... vi

**List of Tables** ..... xii

**Chapter 1. Introduction ..... 1**

1.1 Soft electronics ..... 1

1.2 Soft bioresorbable electronics ..... 7

1.3 Soft perovskite electronics ..... 15

1.4 References ..... 16

**Chapter 2. Design, synthesis and fabrication of bioresorbable electronic patch for glioblastoma ..... 24**

2.1 Introduction ..... 25

2.2 Result and Discussion ..... 27

2.3 Conclusion ..... 48

2.4 Experimental ..... 49

2.5 References ..... 58

**Chapter 3. Integration of destructible resistive memory and multi-dye-sensitized upconverting nanoparticles for information security application .....64**

3.1 Introduction ..... 64

3.2 Result and Discussion ..... 67

3.3 Conclusion ..... 99

3.4 Experimental ..... 100

3.5 References ..... 112

**Chapter 4. High-resolution spin-on-patterning of perovskite thin films for optoelectronic device array....121**

3.1 Introduction ..... 121

3.2 Result and Discussion ..... 124

3.3 Conclusion ..... 144

3.4 Experimental ..... 145

3.5 References ..... 150

**Biblography** ..... 155

**국문 초록 (Abstract in Korean)** ..... 157

# List of Figures

**Figure 1.1** Rigid single crystalline silicon based commercial electronics.....2

**Figure 1.2** Soft electronics for recording device (left) of curvilinear brain surface and the recorded signal (right).....4

**Figure 1.3** Soft wearable electronics for recording biological signal. .....5

**Figure 1.4** Unconventional optoelectronics made of silicon photodiode array .....6

**Figure 1.5** Disposable electronics fabricated on biodegradable materials.....8

**Figure 1.6** Triggered degradation of the electronics. .....9

**Figure 1.7** Bioresorbable electronics for sensing and therapy …… .....10

**Figure 1.8** Edible electronics .....11

**Figure 1.9** Bioresorbable semiconductor.....13

**Figure 2.1** Design and application protocol of the bioresorbable electronic patch (BEP) .....28
**Figure 2.2** Exploded scheme of electronic components of a BEP .....30
**Figure 2.3** Schematic overview of the fabrication process of the BEP .....31
**Figure 2.4** Reaction schemes of the drug reservoir.....33
**Figure 2.5** Schematic comparison of drug delivery from flexible patch and rigid wafer. .....35
**Figure 2.6** Monitoring of BEP containing ferrimagnetic iron oxide contrast agents by magnetic resonance imaging..36
**Figure 2.7** Biocompatibility of OST investigated by intracranial implantation of BEP *in vivo* .....37
**Figure 2.8** Thermal actuation by wireless heater.....40
**Figure 2.9** Effect of drug exposure without (left) and with heating (right) on Survivin expression in U87 tumor tissue. 41
**Figure 2.10** Effect of the thermal actuation in U87 tumor tissue .....43
**Figure 2.11** Differential scanning calorimetry curve and capacitance change around the glass transition temperature

of PLGA .....44

**Figure 2.12** Mean tumor volume of four different groups (left) and its magnified view (right).....47

**Figure 3.1** Characterization of the β-$NaYF_4$:20%Yb, 0.5%Tm UCNPs.....68

**Figure 3.2** Design of multi-dye-sensitized UCNPs and integration with ultrathin nonvolatile memory for advanced information security .....69

**Figure 3.3** Molecular structure and absorption coefficient of fluorescent dye sensitizers for multi-dye-sensitized UCNPs .....71

**Figure 3.4** Characterization and optimization of the sequential energy transfer in multi-dye-sensitized UCNPs ..76

**Figure 3.5** Inter-ligand FRETs in double-ligand nanoparticles .....79

**Figure 3.6** Plot of measured (dots) and calculated (lines) energy transfer efficiency versus inter-ligand distance in the solid state film.....81

**Figure 3.7** Calculated number of conjugated sensitizer II and III on UCNP with respect to the molar ratio control.....85

**Figure 3.8** Design and application protocol of the bioresorbable electronic patch (BEP) .....86

**Figure 3.9** Integration of UCNPs with the ultrathin RRAM

.....88

**Figure 3.10** Comparison of dissolution speed between Mg and ZnO:Mn.....91

**Figure 3.11** Characterization of photo-acid-generator (PAG) .....92

**Figure 3.12** Resistance distribution of the HRS (left) and LRS (right) of 1T1R array.....94

**Figure 3.13** Integration of UCNPs with the ultrathin RRAM.. .....95

**Figure 3.14** Photo-induced destructible RRAM in the wearable and wireless form.....98

**Figure 4.1** Schematic illustration of the spin-on-patterning process ..... 125
**Figure 4.2** Snapshot images at various states of the SoP process captured from a slow-motion video ..... 126
**Figure 4.3** Patterned perovskite thin film ..... 129
**Figure 4.4** X-ray diffraction (XRD) data of the patterned (red) and unpatterned (black) on the FTO substrate ..... 130
**Figure 4.5** Optimization and modelling of the SoP process ..... 132
**Figure 4.6** Modelling of the SoP ..... 133
**Figure 4.7** Effect of the distance from the pattern edge and the pattern area on the grain size ..... 138
**Figure 4.8** Patterned perovskite photodiode ..... 140
**Figure 4.9** Energy level diagram of the patterned perovskite photodiode ..... 141
**Figure 4.10** Frequency response of the patterned perovskite photodiode ..... 142

# List of Tables

**Table 1.1** List of bioresorbable polymer.....14

**Table 2.1** Component materials information of BEPs .....32

**Table 3.1** Optimized inter-ligand distances .....83

**Table 3.2** List of the selected layer information for memory application.....90

**Table 3.1** Contact angle measurements of representative solvents (DMSO, DMF, and γ-butyrolactone) on various substrates treated by the ODPA (n-octadecylphosphonic acid), ODTS (n-octadecyltrichlorosilane), and oxygen plasma .....128

# Chapter 1. Introduction

## 1.1 Soft electronics

Current high-performance electronics are mainly based on inorganic semiconductor materials such as silicon and germanium. The main advantages of these single crystalline inorganic materials are high mobility originated from their crystalline structure, and controllable carrier concentration by changing the impurity doping[1,2]. The integrated circuit (IC) chip made of such inorganic materials can be assembled onto the circuit board to combine with other various commercial electronic components. However, they have been considered as rigid and brittle. The major reason for this mechanical limitation is (1) brittle nature of the single crystalline inorganic semiconductor materials[3], (2) thick encapsulation (~ 1 mm) of the integrated circuit chip[4] and (3) printed circuit board (~ several mm) (**Figure 1.1**).

Recent development of commercial electronics has focused on the personalized devices such as mobile electronics and personal health-care biomedical devices. However, their rigid property hinders the integration of commercial electronics with soft and curvilinear biological interface and

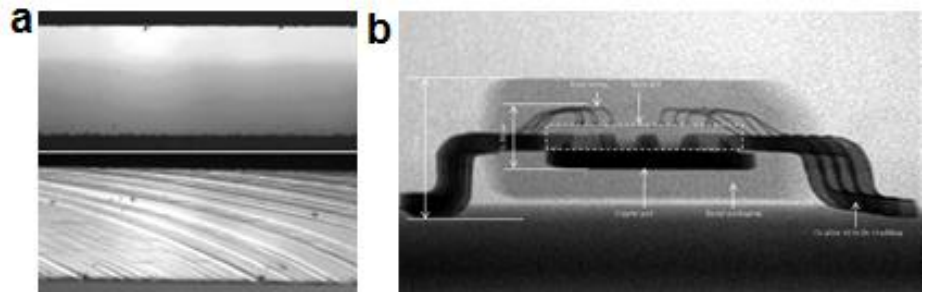


**Figure 1.1 Rigid single crystalline silicon based commercial electronics**

(a) Fracture of the silicon wafer by (top) uniform compression and bending (bottom) (ref 3). (b) X-ray image of commercialized integrated circuit chip made of silicon wafer (ref 4).

other conformable optoelectronics. Therefore, development of soft electronics is highly demanding although they require higher cost and weaker electrical encapsulation than those of rigid electronics. For example, conformable sensor array significantly improved the quality of sensing information from the body (*e.g.* brain and skin)[5-7] (**Figure 1.2**) and allows continuous monitoring of strain[8], electromyography[4] and sweat[9,10] for healthcare (**Figure 1.3**). Soft electronic devices, therefore, have great advantages on biomedical fields and it can be extended to future implantable devices. Another excellent contribution of soft electronics is on the unconventional optoelectronic application. Recent advances in stretchable electronics extend the new concept of image sensor, hemispherical photodetector array inspired by human[11] and arthropod eye[12] for better sight angle and more accurate image quality (**Figure 1.4**). In order to develop this unconventional image sensor, changing the sensing materials from silicon to other light-sensitive materials (e.g. perovskite, organic semiconductor, and GaAs) and fabrication technique for high-density array is required.

In this thesis, fabrication of soft electronic devices using bioresorbable materials and perovskite materials will be described. The soft bioresorbable devices is applied for implantable devices and soft image sensor made of perovskite materials is explained for future ultrathin image sensor.

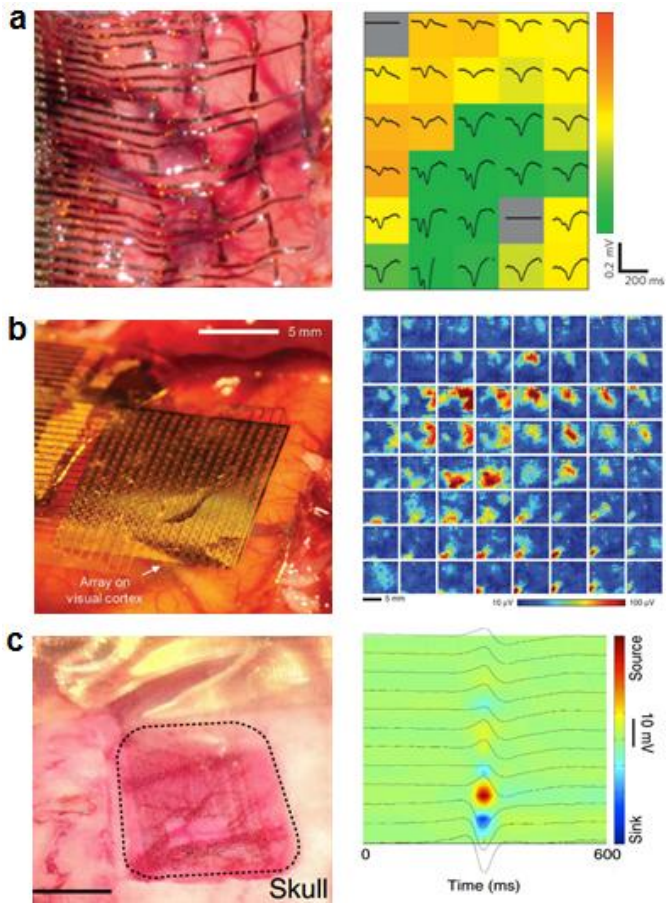


**Figure 1.2 Soft electronics for recording device (left) of curvilinear brain surface and the recorded signal (right)**

Electrocorticogram (ECoG) signal recording by using (a) conformable metal recording line on the bioresorbable substrate (ref 5) (b) active array of silicon electronics (ref 6) and (c) active array of organic electronics.

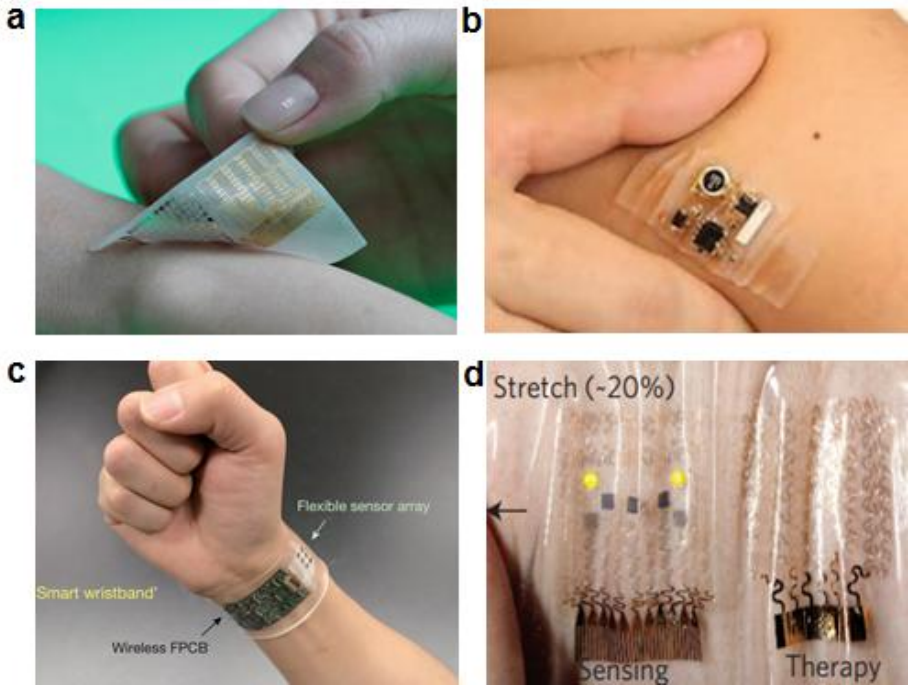


**Figure 1.3 Soft wearable electronics for recording biological signal**

(a) Multifunctional wearable system for monitoring movement disorders. (ref 8) (b) Multifunctional wearable system for recording electromyography. (ref 4) (c) Wearable sweat analysis system for various ion concentration (ref 9) and (d) diabetes monitoring (ref 10).

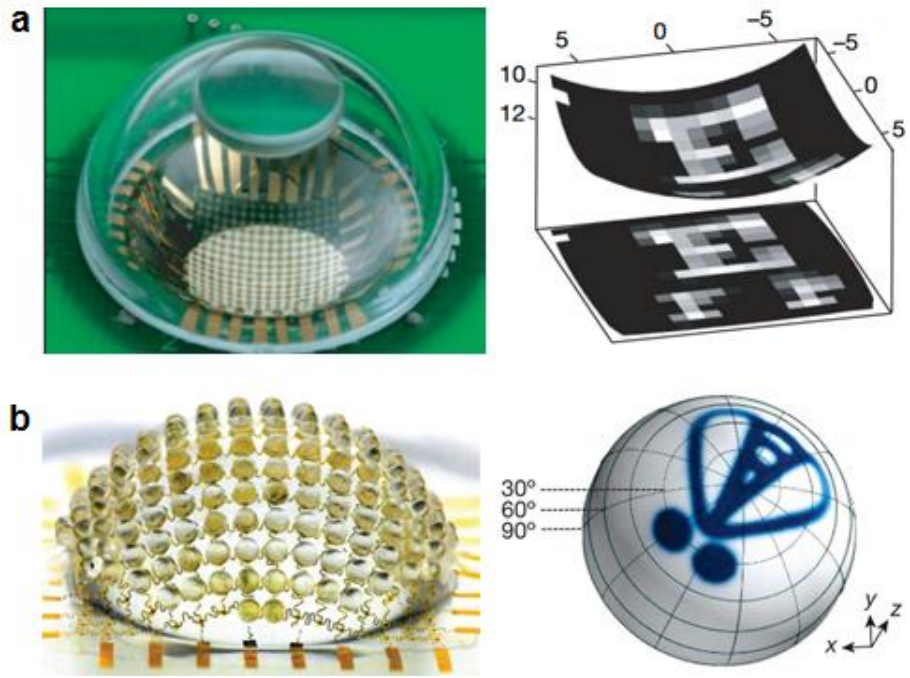


**Figure 1.4 Unconventional optoelectronics made of silicon photodiode array**

(a) Human-eye inspired curvilinear silicon photodiode array (b) Anthropod-eye inspired curvilinear silicon photodiode array combined with spherical microlens.

## 1.2 Soft bioresorbable electronics

Transient electronics are electronic system that disappears physically or chemically when it is needed[13] for various application such as the fields of eco-friendly disposable electronics[14-16] (**Figure 1.5**), security application[17-19] (**Figure 1.6**), biomedical application[20-22] (**Figure 1.7**) and even edible electronics[23-25] (**Figure 1.8**). "Bioresorbable electronics" or "Biodegradable electronics" are the electronics which provide electric functions during desired periods and degrades inside the body when it is not needed[13]. This system is highly demanding since they are used to provide diagnostic and therapeutic functions for a while after implantation and their disappearance makes them free from the removal surgery of them. Many of bioresorbable materials hydrolyzed by natural hydrolysis or enzymatic function and their degradation products should be metabolized or excreted inside the body without any cytotoxicity and inflammatory reaction.

As for the constituent materials, all the components of bioresorbable electronics are classified into conductor, semiconductor, insulator and encapsulation/substrate. The conductor, semiconductor and insulator establish the integrated circuits for electrical functions while the encapsulation and substrate materials protect and support the circuit. Typically, vacuum deposited magnesium (Mg), zinc (Zn), iron (Fe) and their

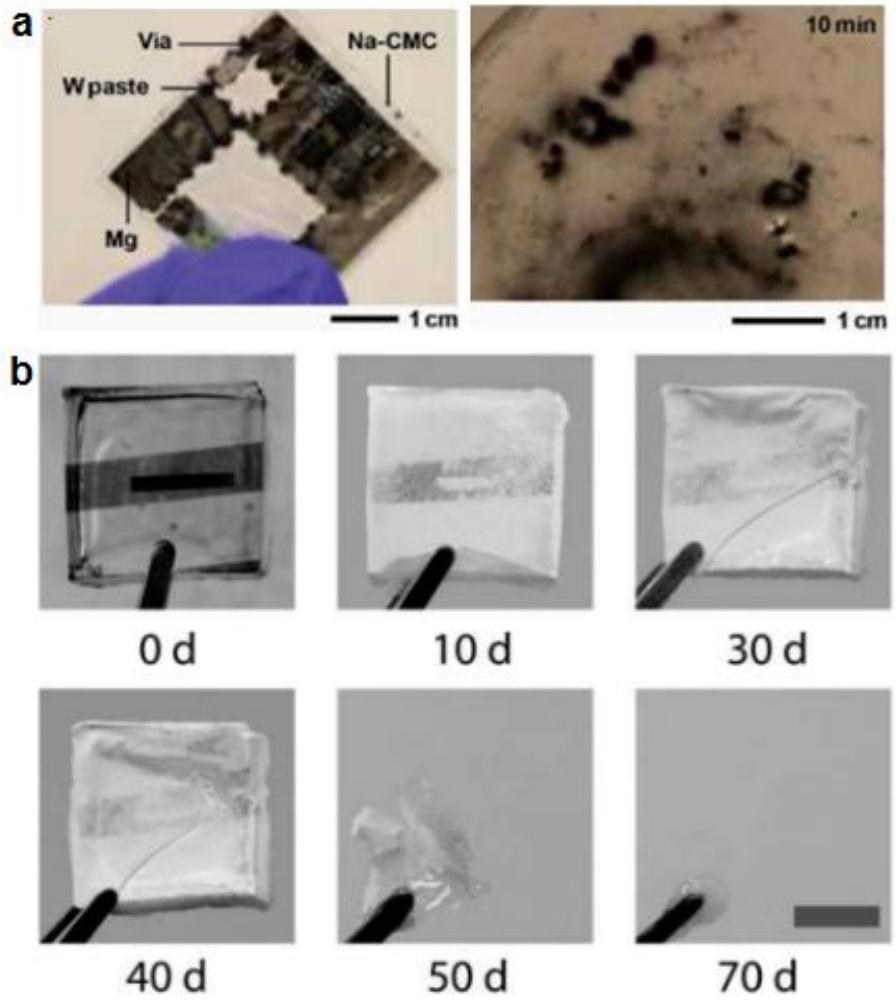


**Figure 1.5 Disposable electronics fabricated on biodegradable materials**

(a) Cellulose substrate (ref 14) (b) Poly (lactic acid-co-glycolic acid) (PLGA) (ref 15)

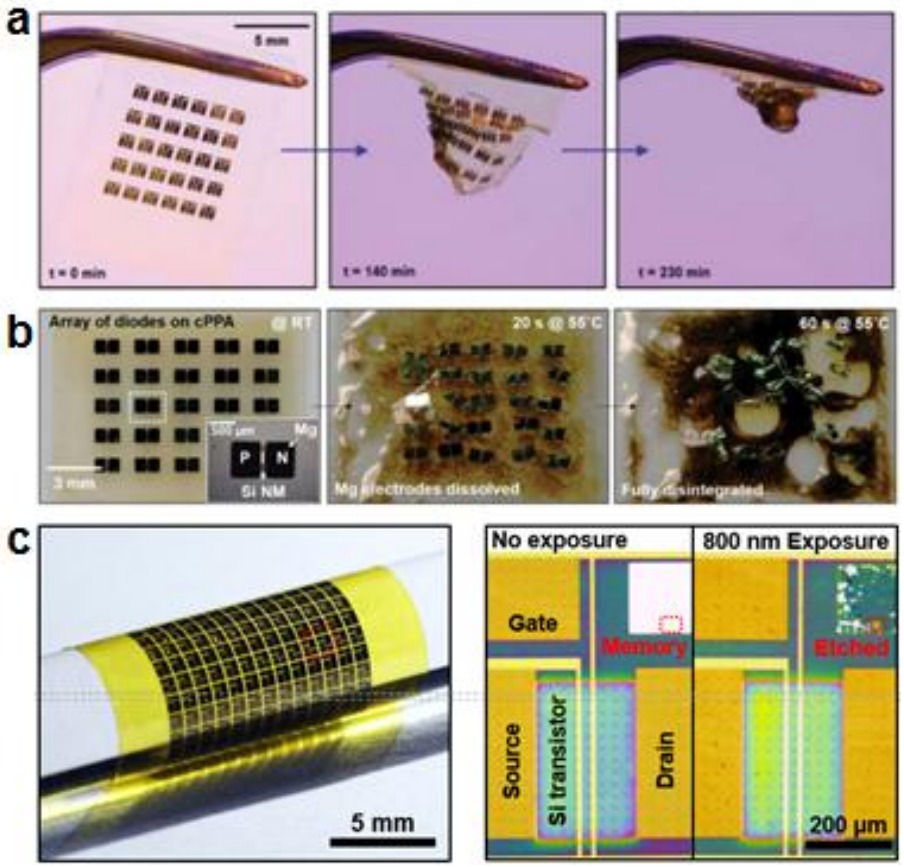


**Figure 1.6 Triggered degradation of the electronics**

(a) Photo-triggered degradation of the electronic circuit board (ref 17) (b) thermally triggered degradation of the electronic circuit board (ref 18) (c) Photo-triggered degradation of resistive random access memory (RRAM) (ref 19)

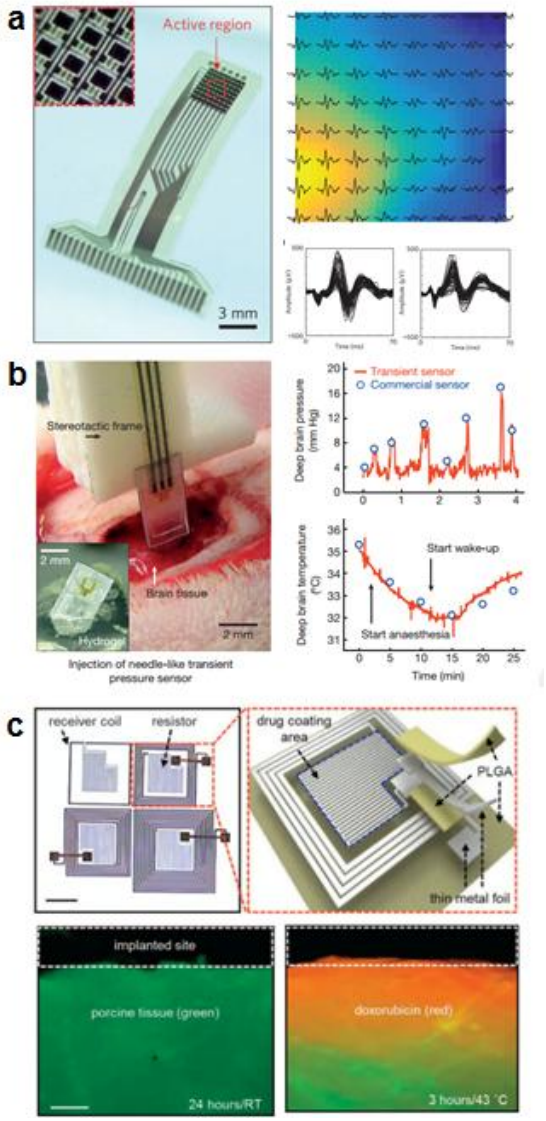


**Figure 1.7 Bioresorbable electronics for sensing and therapy**

(a) Bioresorbable active matrix sensor array for ECoG recording (ref 21) (b) Bioresorbable pressure sensor for brain monitoring (ref 22) (c) Bioresorbable heater for drug actuation (ref 20).

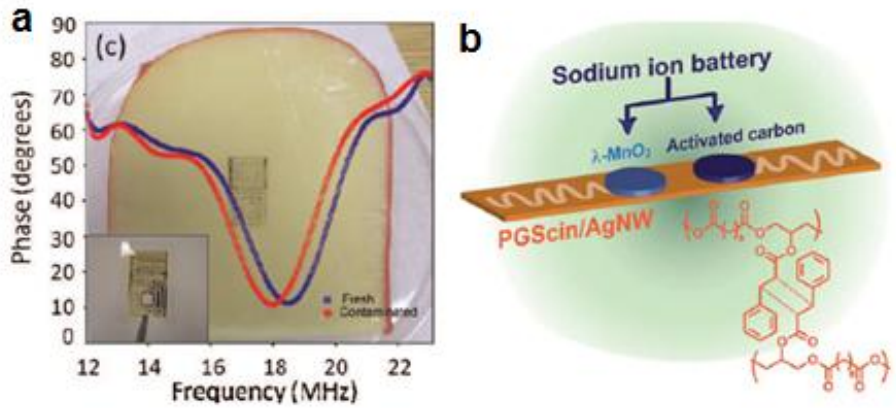


**Figure 1.8 Edible electronics**

(a) Edible silk sensor for food monitoring (ref 23) (b) Edible primary sodium ion battery (ref 24).

alloys[26] are used for bioresorbable conductor since their aqueous cation play important role in human metabolism and establish the orthopedic and muscular system of human body. Biologically derived melanin, which is natural pigment inside the body, can also be used for the conducting electrode[27]. For electronic functions, three kinds of bioresorbable semiconductor have been reported. Synthetic organic semiconductor[16], natural organic semiconductor[25], and silicon nanomembrane[13] (**Figure 1.9**). Especially silicon nanomembrane degrades in biofluid within several ten of days and possess the highest mobility, therefore, is best materials for bioresorbable semiconductor. Most of bioresorbable polymer materials are insulators and can be used for encapsulation layer and substrate. Polyester and polyanhydride is the most common bioresorbable polymer sine the linkage between two monomers can be naturally hydrolyzed in the body. The list of bioresorbable polymer is in table 1.1.

In chapter 2, bioresorbable electronic patch for advanced brain cancer therapy will be presented using soft bioresorbable electronics. In chapter 3, biodegradable resistive memory combined with upconverting nanoparticles and photo-acid generator which degrades when it is needed will be presented.

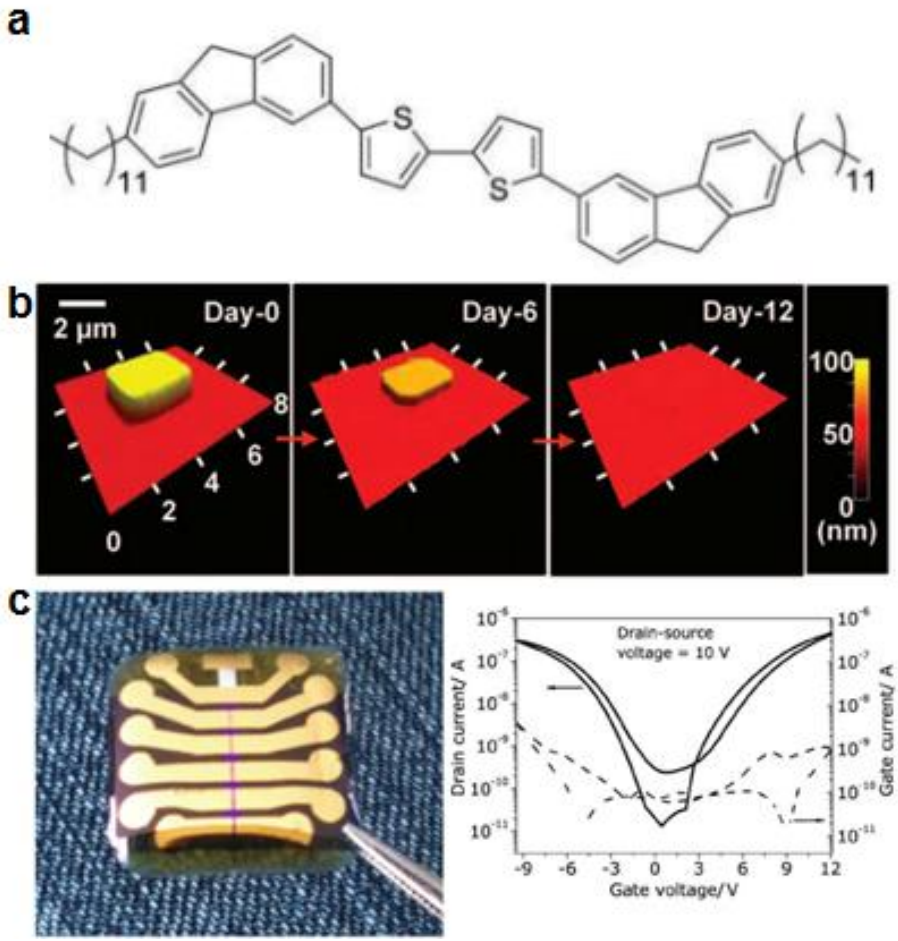


**Figure 1.9 Bioresorbable semiconductor**

(a) Artificial organic semiconductor (ref 16) (b) Biodegradation of the silicon nanomembrane (ref 13) (c) Natural pigment based organic semiconductor (ref 25)

| | | |
|---|---|---|
| **Natural** | saccharide | alginic acid, carrageenan, chitin, chitosan, chondroitin sulfate, dextran, dextran sulfate, dextrose, glycogen, hyaluronic acid, maltose, pectin, pullulan, starch, starch ester, starch ether, cellulose, agar |
| | protein | avidin, biotin, collagen, elastin, silk |
| | lipid | phopholipid, triglycerides |
| **Artificial** | polyester | polylactic acid (PLA),polyglycolic acid (PGA), poly (D,L-lactic-co-glycolic) acid (PLGA), polycaprolactone (PCL), polydioxanone (PDO), poly-β-hydroxybutyrate (PHB), polytrimethylenecarbonate (PTMC) |
| | polyanhyride | poly[1,3-bis(p-carboxyphenoxy)propane: sebacic acid] (PCPP:SA), poly(sebacic acid), poly(azelaic anhydride) |
| | polyamino acids | poly-L-lysine, poly-L-glutamic acid, poly-L-alanine, poly-γ -aminobutylic acid (GABA) |

**Table 1.1 List of bioresorbable polymer**

## 1.3 Perovskite electronics

Recently, organic/inorganic hybrid perovskite materials have attracted great attention because of their outstanding performance as an active material of photovoltaic cells. The main reason of this property originated from high carrier mobility, low trap density and long diffusion length, which is also appropriate for photodetector application. Compared to commercial silicon photodetector, perovskite materials have higher absorption coefficient which means they are much sensitive to the incident light[28] as well as lower noise[28,29]. Since the thickness of the photodetector can be decreased, fabrication process for flexible image sensor is much easier than that of silicon. Up to now, silicon has been regarded as the best materials for the image sensor array, however, the materials properties of perovskite has more advantage on flexible image sensor and can be fabricated with cheaper cost.

The main challenge of the perovskite image sensor is the patterning technique for high density photosensor array. Such perovskite devices have been studied only as large single cell based on bulk crystal[30-32] or spin-coated film[33]. Since organic/inorganic hybrid perovskite materials are vulnerable for almost every polar or protic solvent like water, alcohol, acetone due to their both organic and inorganic nature. In chapter 4, the patterning technique of perovskite thin film will be discussed.

## 1.4 References


1 Khang, D.-Y., Jiang, H., Huang, Y. & Rogers, J. A. A stretchable form of single-crystal silicon for high-performance electronics on rubber substrates. *Science* **311**, 208-212 (2006).

2 Kim, D.-H., Lu, N., Ma, R., Kim, Y.-S., Kim, R.-H., Wang, S., Wu, J., Won, S. M., Tao, H., Islam, A., Yu, K. J., Kim, T.-i., Chowdhury, R., Ying, M., Xu, L., Li, M., Chung, H. -J., Keum, H., McCormick, M., Liu, P., Zhang, Y.-W., Omenetto, F. G., Huang, Y., Coleman, T. & Rogers., J. A. Epidermal electronics. *Science* **333**, 838-843 (2011).

3 Hauch, J. A., Holland, D., Marder, M. P. & Swinney, H. L. Dynamic fracture in single crystal silicon. *Phys. Rev. Lett.* **82**, 3823-3826 (1999).

4 Xu, S., Zhang, Y., Jia, L., Mathewson, K. E., Jang, K.-I., Kim, J., Fu, H., Huang, X., Chava, P., Wang, R., Bhole, S., Wang, L., Na, Y. J., Guan, Y., Flavin, M., Han, Z., Huang, Y. & Rogers, J. A. Soft microfluidic assemblies of sensors, circuits, and radios for the skin. *Science* **344**, 70-74 (2014).

5 Kim, D.-H., Viventi, J., Amsden, J. J., Xiao, J., Vigeland, L., Kim, Y.-S., Blanco, J. A., Panilaitis, B., Frechette, E. S., Contreras, D., Kaplan, D. L., Omenetto, F. G., Huang, Y., Hwang, K.-C., Zakin, M. R., Litt, B. &

Rogers, J. A. Dissolvable films of silk fibroin for ultrathin conformal bio-integrated electronics. *Nat Mater* **9**, 511-517 (2010).

6 Viventi, J., Kim, D.-H., Vigeland, L., Frechette, E. S., Blanco, J. A., Kim, Y.-S., Avrin, A. E., Tiruvadi, V. R., Hwang, S.-W., Vanleer, A. C., Wulsin, D. F., Davis, K., Gelber, C. E., Palmer, L., Van der Spiegel, J., Wu, J., Xiao, J., Huang, Y., Contreras, D., Rogers, J. A. & Litt, B. Flexible, foldable, actively multiplexed, high-density electrode array for mapping brain activity *in vivo*. *Nat. Neurosci.* **14**, 1599-1605 (2011).

7 Khodagholy, D., Doublet, T., Quilichini, P., Gurfinkel, M., Leleux, P., Ghestem, A., Ismailova, E., Hervé, T., Sanaur, S., Bernard, C. & Malliaras, G. G. *In vivo* recordings of brain activity using organic transistors. *Nat. Commun.* **4**, 1575 (2013).

8 Son, D., Lee, J., Qiao, S., Ghaffari, R., Kim, J., Lee, J. E., Song, C., Kim, S. J., Lee, D. J., Jun, S. W., Yang, S., Park, M., Shin, J., Do, K., Lee, M., Kang, K., Hwang, C. S., Lu, N., Hyeon, T. & Kim, D.-H. Multifunctional wearable devices for diagnosis and therapy of movement disorders. *Nat. Nanotech.* **9**, 397-404 (2014).

9 Gao, W., Emaminejad, S., Nyein, H. Y. Y., Challa, S., Chen, K., Peck, A., Fahad, H. M., Ota, H., Shiraki, H., Kiriya, D., Lien, D.-H., Brooks, G. A., Davis, R. W. & Javey, A. Fully integrated wearable sensor arrays for

multiplexed *in situ* perspiration analysis. *Nature* **529**, 509-514 (2016).

10 Lee, H., Choi, T. K., Lee, Y. B., Cho, H. R., Ghaffari, R., Wang, L., Choi, H. J., Chung, T. D., Lu, N., Hyeon, T., Choi, S. H. & Kim, D.-H. A graphene-based electrochemical device with thermoresponsive microneedles for diabetes monitoring and therapy. *Nat. Nanotech.* **11**, 566-572 (2016).

11 Ko, H. C., Stoykovich, M. P., Song, J., Malyarchuk, V., Choi, W. M., Yu, C.-J., Geddes Iii, J. B., Xiao, J., Wang, S., Huang, Y. & Rogers, J. A. A hemispherical electronic eye camera based on compressible silicon optoelectronics. *Nature* **454**, 748-753 (2008).

12 Song, Y. M., Xie, Y., Malyarchuk, V., Xiao, J., Jung, I., Choi, K.-J., Liu, Z., Park, H., Lu, C., Kim, R.-H., Li, R., Crozier, K. B., Huang, Y. & Rogers, J. A. Digital cameras with designs inspired by the arthropod eye. *Nature* **497**, 95-99 (2013).

13 Hwang, S.-W., Tao, H., Kim, D.-H., Cheng, H., Song, J.-K., Rill, E., Brenckle, M. A., Panilaitis, B., Won, S. M., Kim, Y.-S., Song, Y. M., Yu, K. J., Ameen, A., Li, R., Su, Y., Yang, M., Kaplan, D. L., Zakin, M. R., Slepian, M. J., Huang, Y., Omenetto, F. G. & Rogers, J. A. A physically transient form of silicon electronics. *Science* **337**, 1640-1644 (2012).

14 Irimia-Vladu, M. "Green" electronics: biodegradable and biocompatible materials and devices for sustainable future. *Chem. Soc. Rev.*

**43**, 588-610 (2014).

15 Huang, X., Liu, Y., Hwang, S.-W., Kang, S.-K., Patnaik, D., Cortes, J. F. & Rogers, J. A. Biodegradable materials for multilayer transient printed circuit boards. *Adv. Mater.* **26**, 7371-7377 (2014).

16 Bettinger, C. J. & Bao, Z. Organic thin-film transistors fabricated on resorbable biomaterial substrates. *Adv. Mater.* **22**, 651-655 (2010).

**17** Hernandez, H. L., Kang, S.-K., Lee, O. P., Hwang, S.-W., Kaitz, J. A., Inci, B., Park, C. W., Chung, S., Sottos, N. R., Moore, J. S., Rogers, J. A. & White, S. R. Triggered transience of metastable poly(phthalaldehyde) for transient electronics. *Adv. Mater.* **26**, 7637-7642 (2014).

18 Park, C. W., Kang, S.-K., Hernandez, H. L., Kaitz, J. A., Wie, D. S., Shin, J., Lee, O. P., Sottos, N. R., Moore, J. S., Rogers, J. A. & White, S. R. Thermally triggered degradation of transient electronic devices. *Adv. Mater.* **27**, 3783-3788 (2015).

19 Lee, J., Yoo, B., Lee, H., Cha, G. D., Lee, H.-S., Cho, Y., Kim, S. Y., Seo, H., Lee, W., Son, D., Kang, M., Kim, H. M., Park, Y. I., Hyeon, T. & Kim, D.-H. Ultra-wideband multi-dye-sensitized upconverting nanoparticles for information security application. *Adv. Mater.* **(advanced online publication)** (2016) DOI : 10.1002/adma.201603169.

20 Lee, C. H., Kim, H., Harburg, D. V., Park, G., Ma, Y., Pan, T., Kim,

J. S., Lee, N. Y., Kim, B. H., Jang, K.-I., Kang, S.-K., Huang, Y., Kim, J., Lee, K.-M., Leal, C. & Rogers, J. A. Biological lipid membranes for on-demand, wireless drug delivery from thin, bioresorbable electronic implants. *NPG Asia Mater.* **7**, e227 (2015).

21 Yu, K. J., Kuzum, D., Hwang, S.-W., Kim, B. H., Juul, H., Kim, N. H., Won, S. M., Chiang, K., Trumpis, M., Richardson, A. G., Cheng, H., Fang, H., Thompson, M., Bink, H., Talos, D., Seo, K. J., Lee, H. N., Kang, S.-K., Kim, J.-H., Lee, J. Y., Huang, Y., Jensen, F. E., Dichter, M. A., Lucas, T. H., Viventi, J., Litt, B. & Rogers, J. A. Bioresorbable silicon electronics for transient spatiotemporal mapping of electrical activity from the cerebral cortex. *Nat. Mater.* (**advance online publication)** (2016). DOI: doi:10.1038/nmat4624

22 Kang, S.-K., Murphy, R. K. J., Hwang, S.-W., Lee, S. M., Harburg, D. V., Krueger, N. A., Shin, J., Gamble, P., Cheng, H., Yu, S., Liu, Z., McCall, J. G., Stephen, M., Ying, H., Kim, J., Park, G., Webb, R. C., Lee, C. H., Chung, S., Wie, D. S., Gujar, A. D., Vemulapalli, B., Kim, A. H., Lee, K.-M., Cheng, J., Huang, Y., Lee, S. H., Braun, P. V., Ray, W. Z. & Rogers, J. A. Bioresorbable silicon electronic sensors for the brain. *Nature* **530**, 71-76 (2016).

23 Tao, H., Brenckle, M. A., Yang, M., Zhang, J., Liu, M., Siebert, S.

M., Averitt, R. D., Mannoor, M. S., McAlpine, M. C., Rogers, J. A., Kaplan, D. L. & Omenetto, F. G. Silk-based conformal, adhesive, edible food sensors. *Adv. Mater.* **24**, 1067-1072 (2012).

24 Kim, Y. J., Chun, S.-E., Whitacre, J. & Bettinger, C. J. Self-deployable current sources fabricated from edible materials. *J. Mater. Chem. B* **1**, 3781-3788 (2013).

25 Irimia-Vladu, M., Głowacki, E. D., Troshin, P. A., Schwabegger, G., Leonat, L., Susarova, D. K., Krystal, O., Ullah, M., Kanbur, Y., Bodea, M. A., Razumov, V. F., Sitter, H., Bauer, S. & Sariciftci, N. S. Indigo - A natural pigment for high performance ambipolar organic field effect transistors and circuits. *Adv. Mater.* **24**, 375-380 (2012).

26 Zberg, B., Uggowitzer, P. J. & Loffler, J. F. MgZnCa glasses without clinically observable hydrogen evolution for biodegradable implants. *Nat. Mater.* **8**, 887-891 (2009).

27 Kim, Y. J., Wu, W., Chun, S.-E., Whitacre, J. F. & Bettinger, C. J. Biologically derived melanin electrodes in aqueous sodium-ion energy storage devices. *Proc. Nat. Acad. Sci.* **110**, 20912-20917 (2013).

28 Koppens, F. H. L., Mueller, T., Avouris, P., Ferrari, A. C., Vitiello, M. S. & Polini, M. Photodetectors based on graphene, other two-dimensional materials and hybrid systems. *Nat. Nanotech.* **9**, 780-793 (2014).

29 Lin, Q., Armin, A., Lyons, D. M., Burn, P. L. & Meredith, P. Low Noise, IR-blind organohalide perovskite photodiodes for visible light detection and imaging. *Adv. Mater.* **27**, 2060-2064 (2015).

30 Fang, Y., Dong, Q., Shao, Y., Yuan, Y. & Huang, J. Highly narrowband perovskite single-crystal photodetectors enabled by surface-charge recombination. *Nat. Photon.* **9**, 679-686 (2015).

31 Shi, D., Adinolfi, V., Comin, R., Yuan, M., Alarousu, E., Buin, A., Chen, Y., Hoogland, S., Rothenberger, A., Katsiev, K., Losovyj, Y., Zhang, X., Dowben, P. A., Mohammed, O. F., Sargent, E. H. & Bakr, O. M. Low trap-state density and long carrier diffusion in organolead trihalide perovskite single crystals. *Science* **347**, 519-522 (2015).

32 Dong, Q., Fang, Y., Shao, Y., Mulligan, P., Qiu, J., Cao, L. & Huang, J. Electron-hole diffusion lengths > 175 μm in solution-grown $CH_3NH_3PbI_3$ single crystals. *Science* **347**, 967-970 (2015).

33 Nie, W., Tsai, H., Asadpour, R., Blancon, J.-C., Neukirch, A. J., Gupta, G., Crochet, J. J., Chhowalla, M., Tretiak, S., Alam, M. A., Wang, H.-L. & Mohite, A. D. High-efficiency solution-processed perovskite solar cells with millimeter-scale grains. *Science* **347**, 522-525 (2015).

34 Wang, G., Li, D., Cheng, H.-C., Li, Y., Chen, C.-Y., Yin, A., Zhao, Z., Lin, Z., Wu, H., He, Q., Ding, M., Liu, Y., Huang, Y. & Duan, X. Wafer-

scale growth of large arrays of perovskite microplate crystals for functional electronics and optoelectronics. *Sci. Adv.* **1**, e1500613 (2015).

# Chapter 2. Design, synthesis and fabrication of bioresorbable electronic patch for glioblastoma treatment

## 2.1 Introduction

Treatment of glioblastoma multiforme (GBM) has been highly challenging even after all the aggressive neurosurgery with subsequent radio- and chemo-therapies[1]. This is because the malignant tumor cells that invaded into surrounding normal brain tissues survive through the surgical resection[2,3] and cause the tumor recurrence[4]. The radiation therapy with exposure under the dose limit is not sufficient to remove residual tumors completely[5,6]. Additional chemo-therapies are oftentimes unsuccessful, since the blood-brain barrier (BBB) blocks the delivery of drugs with effective concentrations to brain tumors diffused into surrounding brain tissues[7,8]. A localized drug delivery to the tumor site through implantation of biodegradable polymer containing carmustine (Gliadel® wafer, Arbor Pharmaceuticals, USA) was proposed as a promising alternative[9-11]. It delivered the drug bypassing the BBB and exhibited modest enhancement of the survival rate[12]. However, many challenges still remain toward the dramatic improvement of the

prognosis. This polymer implant mainly relies on the natural drug diffusion that results in the limited penetration depth[13,14]. This can lead to tumor recurrence near the surgery and/or implantation site[15]. The short-term drug release, uncontrollable drug delivery to cerebrospinal fluid (CSF), hydrophobic nature, and mechanical rigidity of the wafer are additional factors that reduce the efficacy of the drug delivery into the curvilinear-shape brain tissues at the surgery site.

Here, we report the material synthesis, device design, and application protocol of a bioresorbable electronic patch (BEP) for the GBM treatment. The system consists of a flexible drug-containing oxidized starch (OST) patch, a magnesium (Mg) wireless heater for the wirelessly-controlled drug delivery, and an onboard wireless temperature sensor to prevent the excessive heating of brain tissues. The release rate of the drug, doxorubicin (DOX), is sustained under the normal condition through its covalent bonding to the OST chain network for the prolonged delivery period. But the drug release is periodically accelerated by the wireless thermal actuation based on the pre-programmed protocol. The increase of temperature is not high (~5 °C) to minimize the thermal damage to normal brain tissues but induces a significant increase of the penetration depth (~7 times) compared to the natural diffusion. The hydrophilic surface of OST, hydrophobic encapsulation layer, and flexibility

of the patch enable its conformal adhesion and localized drug delivery to surgical sites. All constituent materials are hydrolyzed into bioresorbable units, such as glucose, Mg, lactic acid, and glycolic acid, which are components of the human body and metabolism. Since the bioresorbable electronic system leaves no device component[16-18] in the brain, side-effects after implantation of device[19-21] can be prevented, which gives an influence on the prognosis. The system implanted in the mouse and canine brain tumor model successfully inhibits the recurrence of the tumor *in vivo*. After 26 days of the implantation, the BEP-implanted group shows a 2-fold decrease of the original tumor volume, while the control group exhibited a 56-fold increase.

## 2.2 Result and Discussion

### 2.2.1 System design and application protocol

**Figure 2.1a** presents an optical camera image of the BEP. The diameter and thickness of the BEP is 18 mm and ~200 μm, respectively. The BEP contains 12 mg DOX for the GBM therapy and bioresorbable electronic components are transfer-printed onto a OST patch. **Figure 2.2** illustrates multi-layered materials information; **Figure 2.3** describes the detailed fabrication process of the electronics on the patch. All functional units are composed of bioresorbable materials, such as Mg (conductor), poly(lactic-co-glycolic acid)/poly(lactic acid) (PLGA/PLA; dielectric layer or barrier), and OST (drug-containing patch). Products after the hydrolysis and resulting amounts are described in **Table 2.1**. For the drug delivery over an extended period of time, drugs are physically and chemically bonded to OST polymer chains (**Figure 2.4**). A key advantage of the wirelessly controlled drug delivery system is that the suppressed drug release due to the physical and chemical bonding can be actively accelerated through the periodic wireless induction heating by the Mg heater. The array of the hole pattern on the heater plays a critical role on the uniform thermal. The temperature sensor is located at the center of the patch to monitor the temperature. The electronics and patch also can be applied to the delivery of other anti-cancer drugs (*i.e.,* temozolomide).

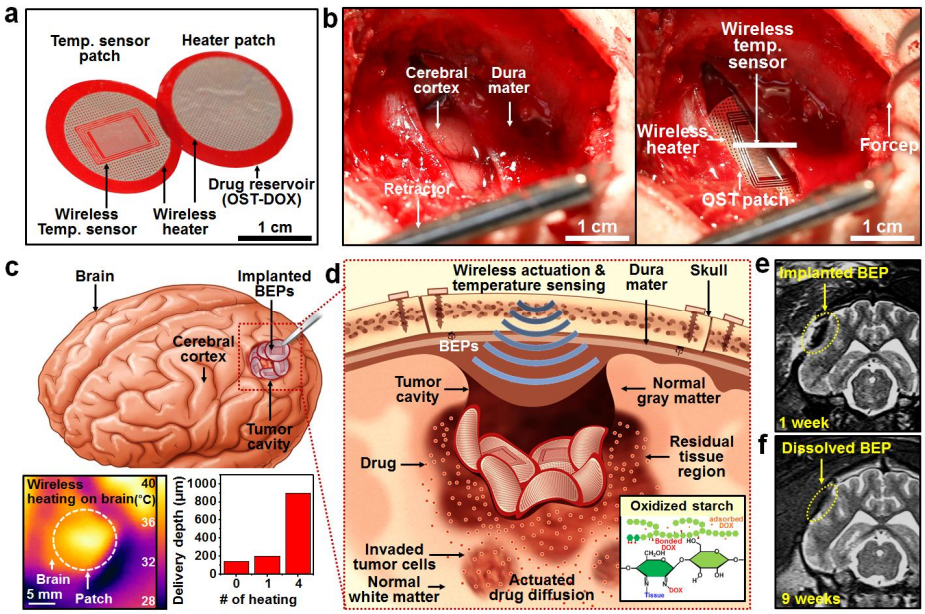


**Figure 2.1 Design and application protocol of the bioresorbable electronic patch (BEP).**

(a) Optical camera image of the BEP. The BEP includes a bioresorbable wireless heater and temperature sensor on a oxidized starch (OST) patch containing doxorubicin (DOX). (b) Image of the brain tumor resection surgery in the canine model before (left) and after (right) implantation of the BEP. (c) Schematic illustration of the BEP implanted on the target site (top), infrared camera image of the patch during the thermal actuation (left inset), and enhanced penetration depth of drug by the thermal actuation (right inset). (d) Schematic illustration of the localized and penetrative drug delivery into the deep brain tissues by the BEP. Inset shows the chemical structure of the drug-

conjugated OST. (e) Non-invasive monitoring of the implanted BEP under bioresorption after 1 week (left) and 9 weeks (right) implantation. The BEP contains ferrimagnetic iron oxide nanoparticles (FION) as a contrast agent of magnetic resonance imaging (MRI).

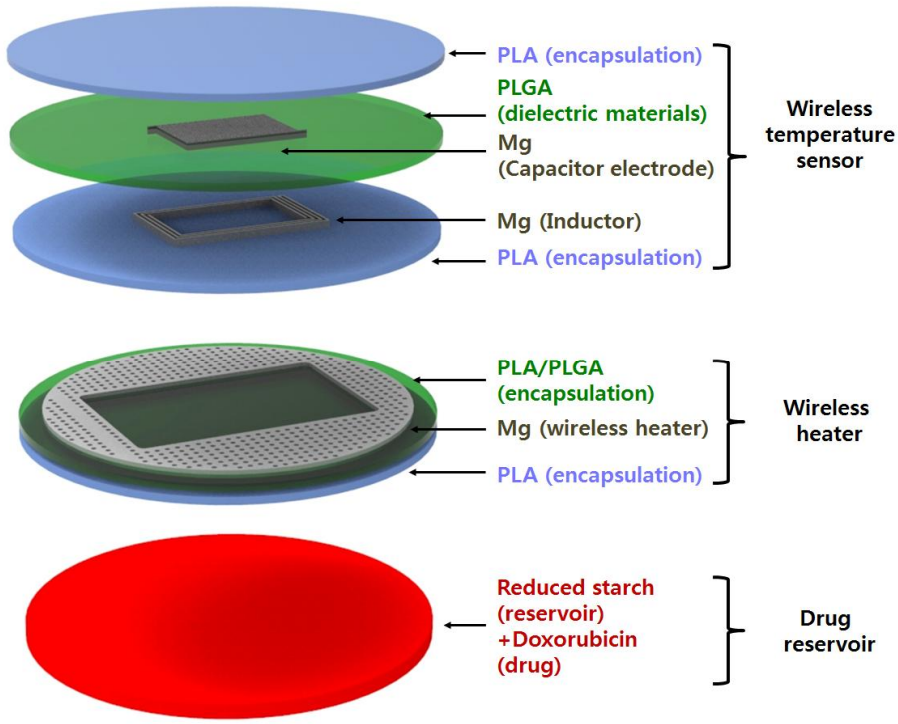


**Figure 2.2 Exploded scheme of electronic components of a BEP.**

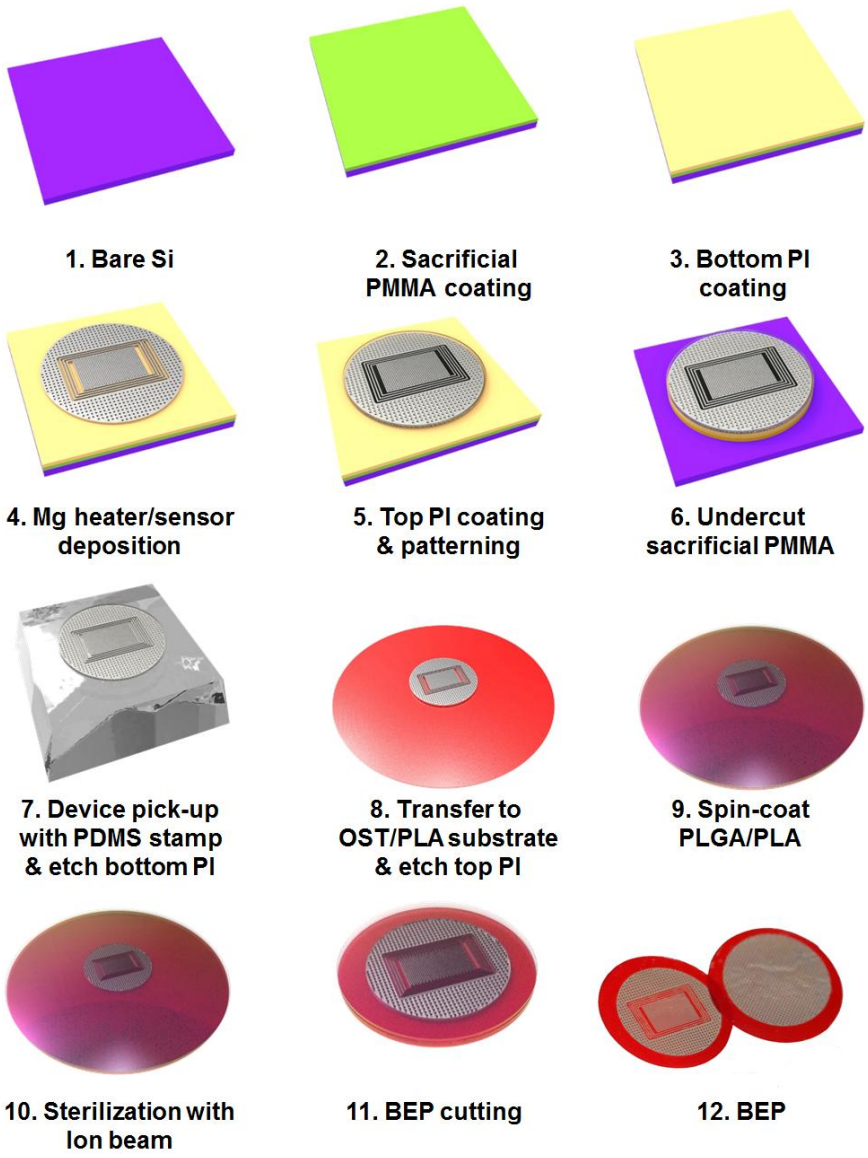


**Figure 2.3 Schematic overview of the fabrication process of the BEP.**

| Elements | Thickness | Products | Mass | μM |
|---|---|---|---|---|
| **Mg** | 3 μm | $Mg^{2+}$ | 0.78 mg | 32.5 |
| **Starch** | 200 μm | Glucose | 360 mg | 2000 |
| **Glycerol** | | Glycerol | 108 mg | 1173 |
| **PLA** | 3 μm | Lactic acid | 0.58 mg | 18.6 |
| **PLGA** | 7 μm | Lactic acid | 1.10 mg | |
| | | Glycolic acid | 0.31 mg | 4.08 |
| **DOX** | | Doxorubicin | 12 mg | 20.7 |

**Table 2.1 Component materials information of BEPs.**

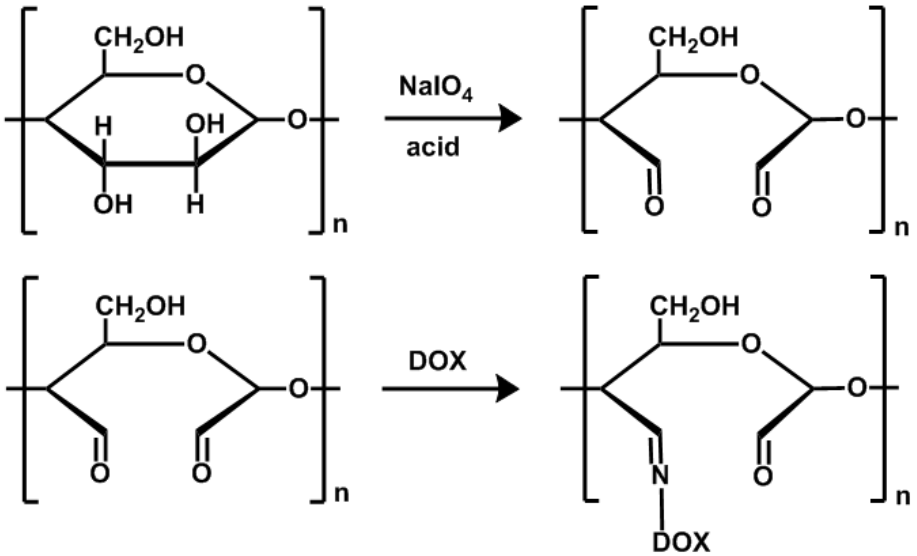


**Figure 2.4 Reaction schemes of the drug reservoir.**

(top) Oxidized starch (OST) (bottom) OST conjugated with doxorubicin (OST-DOX).

After the surgical resection of malignant glioma (**Figure 2.1b** left), BEPs are conformally laminated on the cavity-shape surgery site (**Figure 2.1b** right). Because of the sticky and flexible nature of the OST patch, it makes a strong and conformal adhesion to the curved brain cavity surface (**Figure 2.5**; Schematic illustration in comparison with a rigid, thick and hydrophobic patch). **Figure 2.1c** illustrates that the thermal actuation by the wireless heater (bottom left; infrared camera image) after the implantation of BEPs (top; schematic illustration) enhances the release rate and penetration depth of DOX (bottom right; graph). Due to this actuation, DOX reaches residual tumors invaded deeply in normal tissues (**Figure 2.1d**), which have been difficult to be treated under current clinical practice guidelines[22,23]. The wireless temperature sensor monitors the temperature and inhibits overheating of normal brain tissues. The intracranial resorption of the BEP is visually monitored using a MRI contrast agent of ferrimagnetic iron oxide nanotubes (FION). Compared to the case at one week after the surgery (**Figure 2.1e**), the volume of the patch is significantly decreased (**Figure 2.1f**) after nine weeks due to its gradual hydrolysis and resorption by the brain (**Figure 2.6**). This bioresorption process exhibited no significant immune responses (**Figure 2.7**).

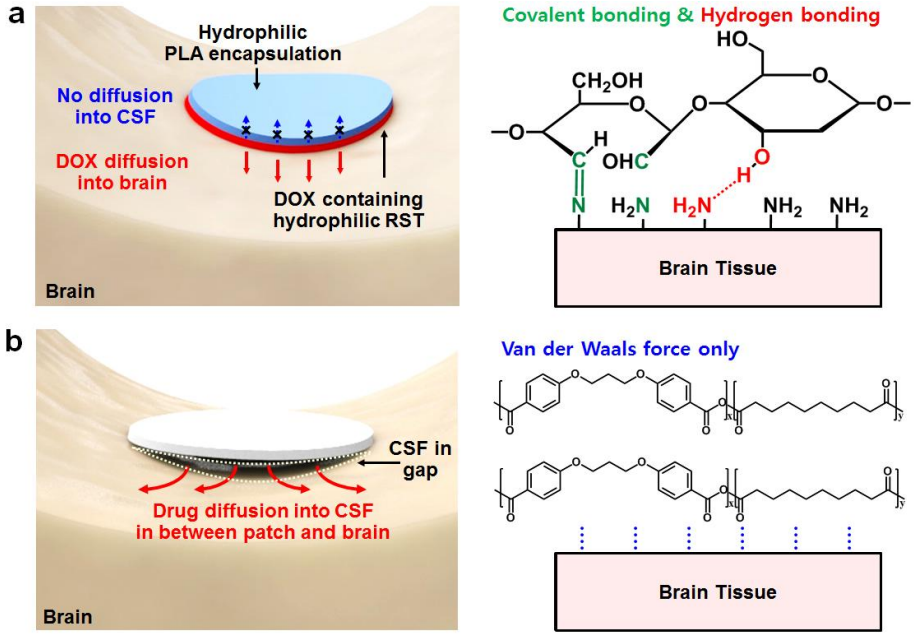


**Figure 2.5 Schematic comparison of drug delivery from flexible patch and rigid wafer.**

(a) Illustration of the interface between flexible BEP and curvilinear brain surface (left) and its molecular aspect (right). (b) Illustration of the interface between rigid bioresorbable wafer and curvilinear brain surface (left) and its molecular aspect (right).

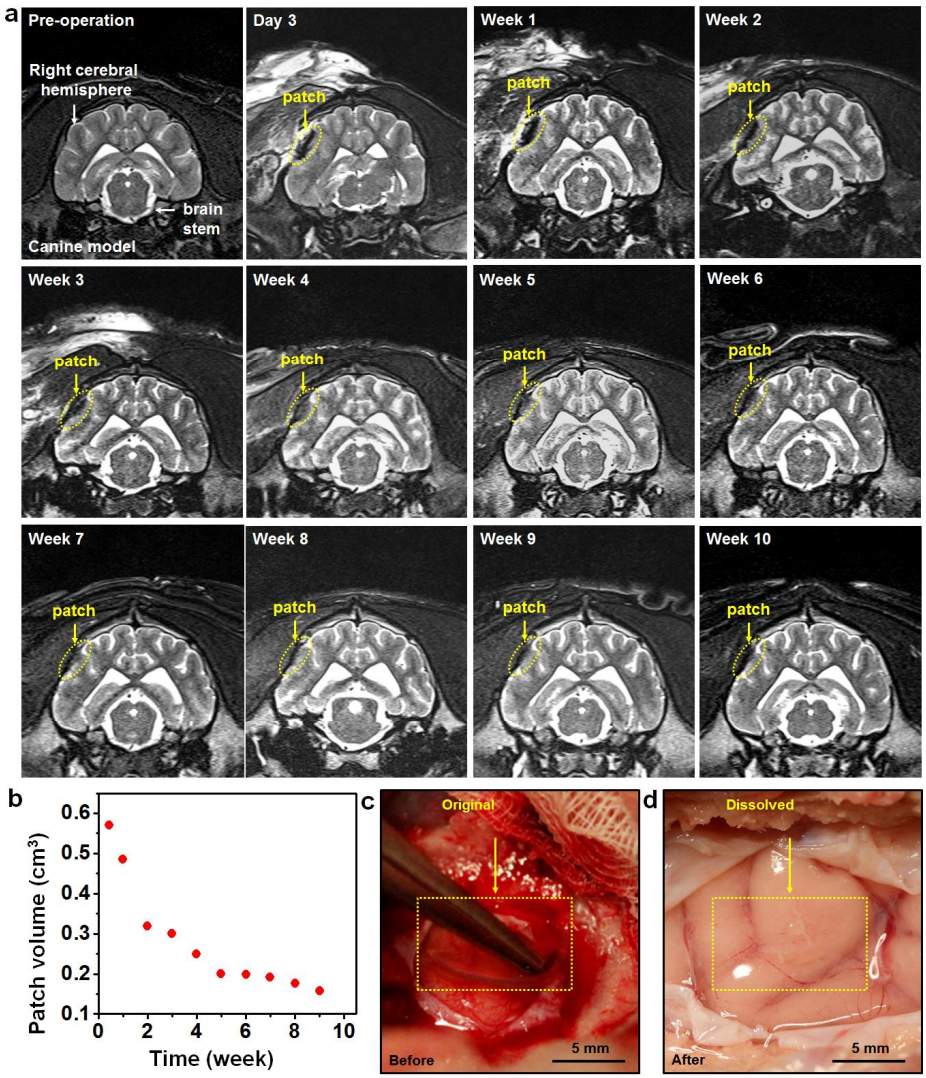


**Figure 2.6 Monitoring of BEP containing ferrimagnetic iron oxide contrast agents by magnetic resonance imaging (MRI).**

(a) The MRI before and after BEP implantation. (b) Calculated patch volume as a function of time (c) Optical image during intracranial OST patch implantation surgery (d) Optical image of implantation site after 10 weeks.

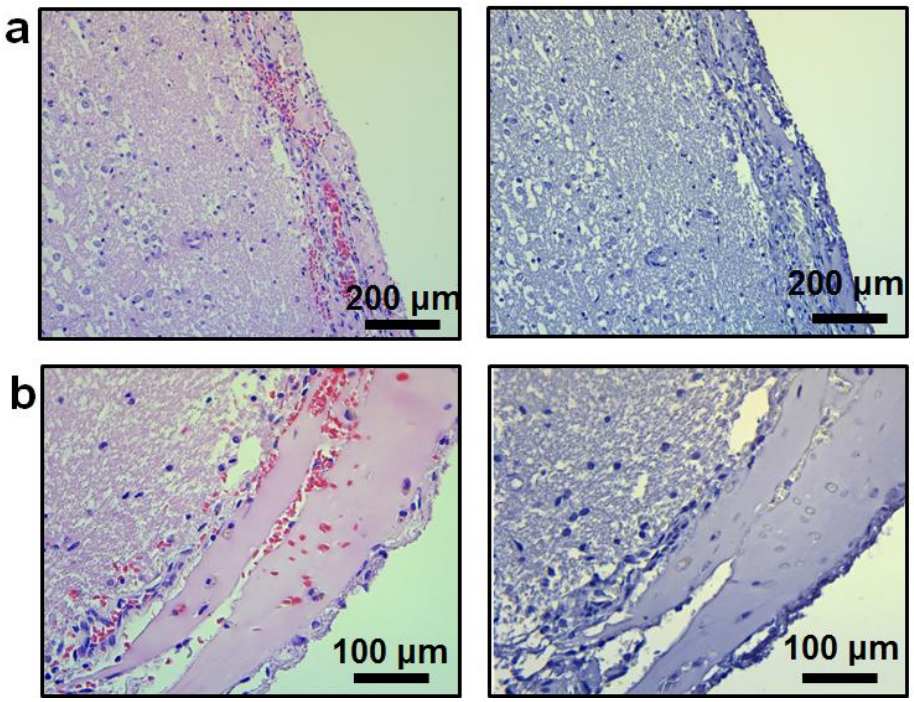


**Figure 2.7 Biocompatibility of OST investigated by intracranial implantation of BEP *in vivo.*** Hematoxylin and eosin (H&E) stained histological image (left) and F4/80 stained immunolabeling image (right). (**a**) ×100 magnification and (**b**) ×100 magnification.

### 2.2.2 Fabrication and characterization of the OST patch and the device

The OST patch is fabricated by dissolving the synthesized OST powder, glycerol (plasticizer), and DOX in water at 65 °C and then by drying the solution under a humid condition (65 °C, 80%). The conformal contact (**Figure 2.5**) enables the efficient heat and drug transport from the patch as well as the focused drug delivery to the area where the patch attached. The fluorescence microscope image shows that the patch conformally adheres to the brain tissue (2.6a), and the drug diffuses well at the interface. The conformal and strong adhesion between tissue and OST patch is originated by hydrophilic nature of starch and additional imine conjugation between protein and the polymer chain (**Figure 2.5a** right).

### 2.2.3 Penetrative by wireless thermal actuation

The encapsulation layer added on the top of the OST patch suppresses the direct drug release to the cerebrospinal fluid (CSF), which causes side effects[24]. Wireless thermal actuation enhances the penetration depth (**Figure 2.1e**) of DOX *in vivo*. **Figure 2.8a** shows the fluorescence microscope images of DOX penetrated from the BEP patch to the U87 glioblastoma xenograft tissue in a nude mouse model for 15 h without (left) and with (right) the wireless heating ($\Delta T$ = 5 °C, 30 min; 1 pulse) *in vivo*. DOX successfully reaches the deep inside the tissue, resulting in the death of cancer cells (**Figure 2.8b** and **Figure 2.9**). The DOX concentration at various diffusion lengths is quantified by integrating the equidistant fluorescence intensity (**Figure 2.8c and 2.8d**). While only a small diffusion length and amount are observed in the natural diffusion (**Figure 2.8c**), mild thermal actuations dramatically enhance the diffusion length and amount of DOX (**Figure 2.8d**). The origin of significant diffusion enhancement is mainly because the DOX permeability of cell membrane is dramatically enhanced[25,26] while the increase of diffusion coefficient is negligible.

Appropriate thermal actuation significantly promotes the drug diffusion, but an excessive heating may cause neuronal apoptosis[27] of normal brain tissues. The temperature of the heater depends on a coil-to-patch distance, a radius of

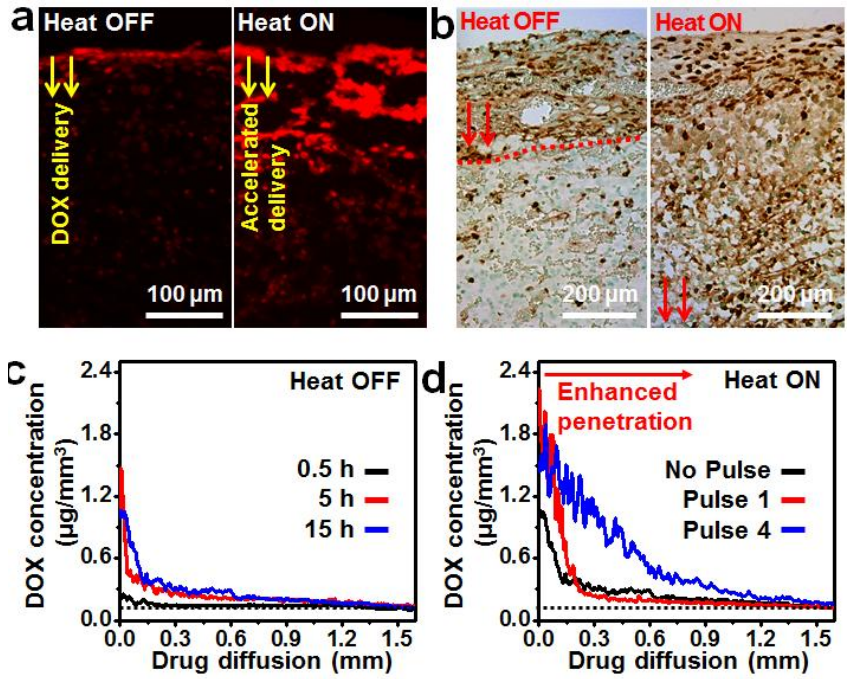


**Figure 2.8 Thermal actuation by wireless heater**

(a) Fluorescence images that show the diffused DOX from the BEP into the U87 GBM tissue of the mouse model *in vivo* without (left) and with (right) the thermal actuation. (b) Effect of the drug delivery without (left) and with (right) the thermal actuation on the HUVEC expression in U87 tumor tissues. (c) DOX concentration in U87 tumor tissues 0.5 h (black), 5 h (red), and 15 h (blue) after the implantation of the BEP without the thermal actuation. (d) DOX concentration in U87 tumor tissues 15 h after the implantation of the BEP with the 30 min pulsed control (black; no pulse), 1 pulse (red), and 4 pulses(blue).

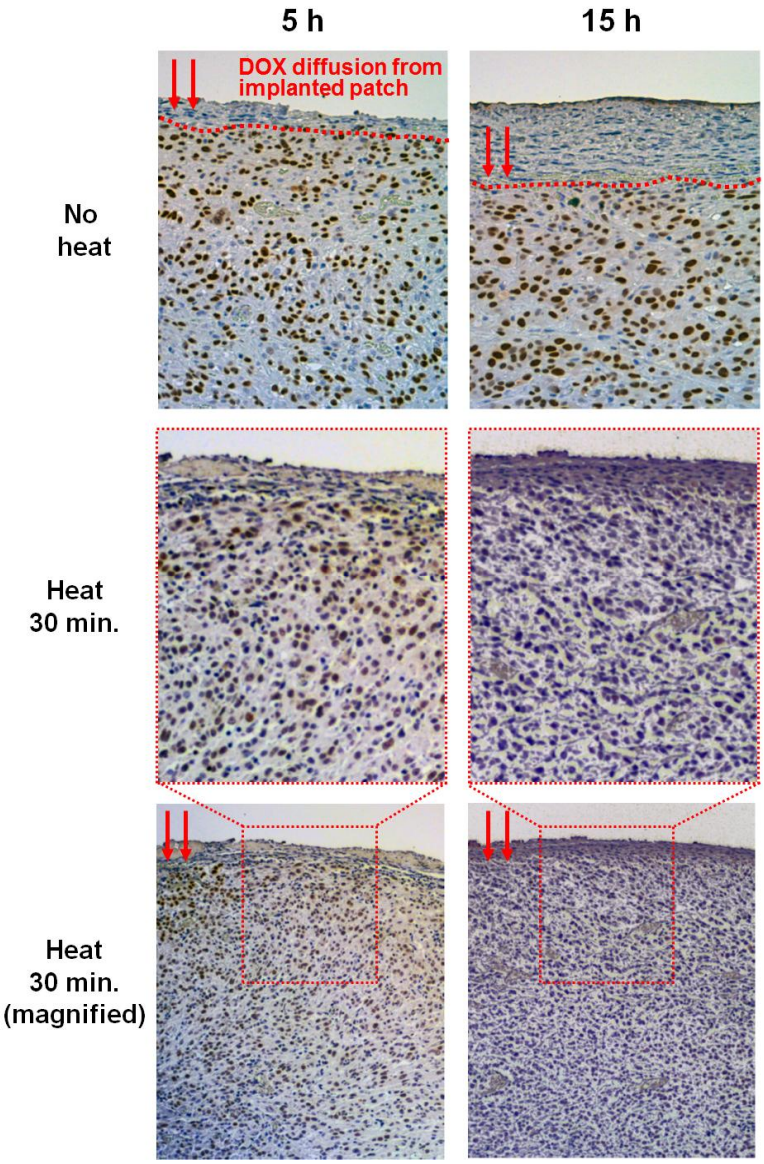


**Figure 2.9 Effect of drug exposure without (left) and with heating (right) on Survivin expression in U87 tumor tissue.**

the patch, and the current of a RF generator. The thermal damage on the tissues is investigated by histology analysis with the apoptosis inhibitor (Survivin) at different temperatures by changing coil-to-patch distance (**Figure 2.10a**). A temperature increase of 5 °C (41.5 °C) for 30 min induces minimal cell apoptosis at the interface, while a 10 °C and 15 °C increase cause significant cell death. The thermal damage is focused on the patch interface, since heat is dissipated by the blood flow in distant regions. Therefore, the temperature should be 41.5 °C ($\Delta T = 5$ °C) or below to prevent thermal damages. For the real-time temperature monitoring, a RLC oscillator, composed of a Mg inductor and PLGA capacitor, is integrated on the patch. PLGA (65:35 = lactic acid: glycolic acid) exhibited a glass transition ($T_g$) around 39 °C (**Figure 2.11**), and dielectric permeability and thus the capacitance changes around this $T_g$. This change induces the resonance frequency change of the sensor and can be read by a coupled reader coil (**Figure 2.10b**).

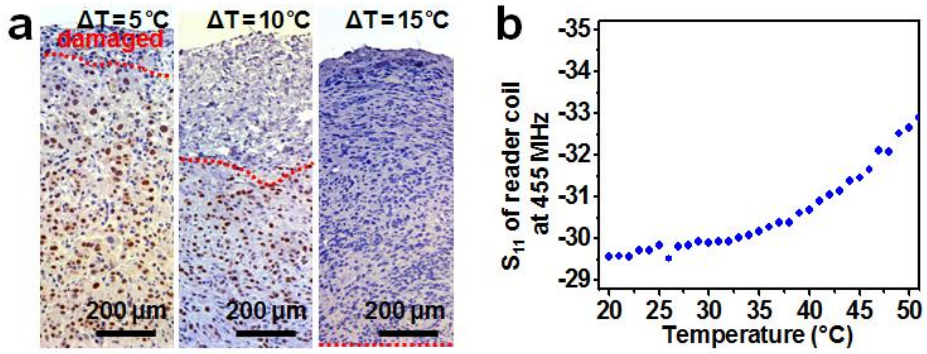


**Figure 2.10 Effect of the thermal actuation in U87 tumor tissue.**

(a) Effect of the elevated temperature on the Survivin expression in U87 tumor tissues. (b) $S_{11}$ of the reader coil at 455 MHz versus temperature of the heater. Inset shows the $S_{11}$ change of the reader coil.

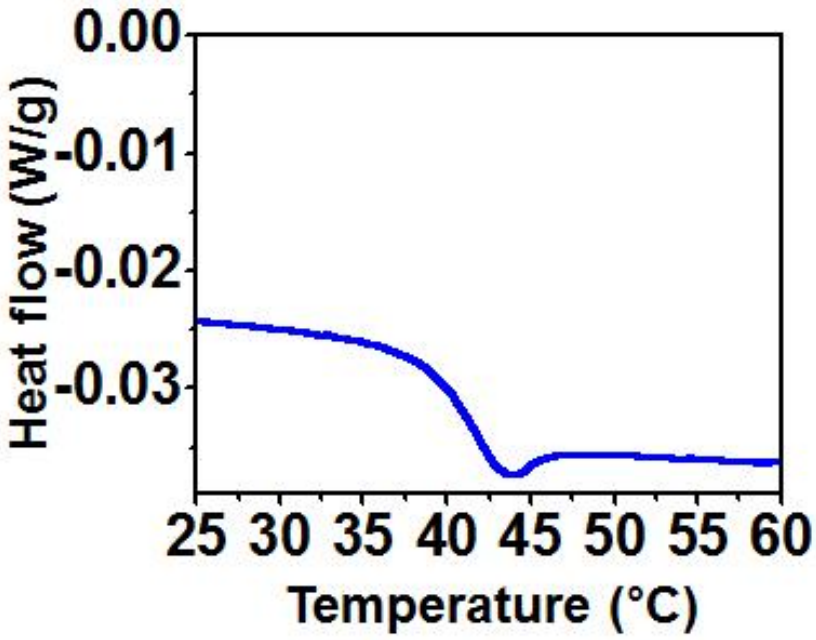


**Figure 2.11 Differential scanning calorimetry curve and capacitance change around the glass transition temperature of PLGA**

### 2.2.4 Therapeutic effect of the BEP in the mouse tumor model

To evaluate the therapeutic efficacy of the BEP *in vivo*, we used the human xenograft GBM model in immune-deficient mice. The model is established by subcutaneous implantation of U87 human GBM cells near the thigh of 6 weeks balb/c nude mouse. Details for the model and surgical procedure are described in Experimental section. The tumor is grown for 3 weeks to be a spherical shape of ~4 mm radius and resected with ~20 $mm^3$ mean residual volume. Then, a BEP contains 0.408 mg DOX (0.02 mg per a gram body weight of the mouse) is implanted on the residual tumor. Mice are divided into four groups with different treatments: (1) intravenous injection of DOX, (2) implantation of the BEP with the wireless heating but without DOX, (3) implantation of the BEP with DOX but no heating (OST group), and (4) implantation of the BEP with DOX and heating (OST+Heating group). The number of mice of each group is 6, 7, 7, and 6, respectively. We analyzed therapy results by comparing the tumor volume (**Figure 2.12**) which is estimated by using MR imaging.

U87 cells are highly aggressive, and thereby the prognosis is poor in the "IV" and "Heating" group. However, the "OST" group exhibits meaningful suppression of the tumor recurrence ($p=0.042$) due to the penetrative and localized drug delivery. The BEP with the thermal actuation ("OST+Heating"

group) shows even more significant reduction of the tumor volume than others ($p=0.0036$). This is largely because the thermal actuation successfully increases the penetration depth of DOX to reach deep residual tumors. At the day 25 after the implantation, the mean tumor volume of the "OST+Heating" group exhibits a two-fold decrease, from 31 $mm^3$ to 14 $mm^3$.

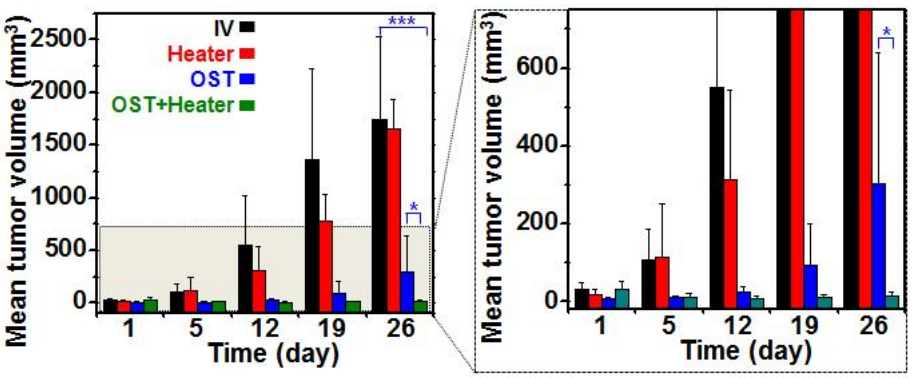


**Figure 2.12 Mean tumor volume of four different groups (left) and its magnified view (right).**

## 2.3 Conclusion

We reported novel materials synthesis, device designs, and therapeutic efficacy of a bioresorbable electronic patch (BEP) for the malignant glioma treatment. The BEP consists of doxorubicin-conjugated oxidized starch (OST) integrated with a wireless thermal actuator and temperature sensor. All constituent materials are bioresorbable in the brain. The rate and depth of the doxorubicin delivery can be wirelessly controlled by the integrated electronics. The enhanced diffusion depth and elongated delivery period of the drug dramatically improved the tumor volume suppression in the mouse model. The BEP applied to the canine glioblastoma model *in vivo* successfully inhibited the tumor recurrence.

## 2.4 Experimental

### 2.4.1 Biocompatibility of materials

A BEP patch is composed of the electronic part and drug reservoir part. Mg is an electronic conductor, PLGA and PLA are the dielectric and water-proof barrier, oxidized starch (OST) as a drug reservoir. The hydrolyzed products are $Mg^{2+}$, lactic acid, glycolic acid and glucose which are used in metabolism of the brain. The amount of constituent materials is listed in Table 1. OST and Mg degrades within 4~6 weeks, while PLA and PLGA takes longer time to degrade. The degradation of OST appears to be biocompatible both *in vitro* and *in vivo*. Subcutaneous implantation in balb/c nude mouse and intracranial implantation in canine. OST is implanted symmetrically into the thighs of same animal. The inflammatory responses subsided with time. The thickness of inflammatory zone in both implantation sites was approximately the same with non-implantation site.

### 2.4.2 Wireless temperature sensor

LC oscillator, the wireless temperature sensor, was fabricated using Mg conductor and PLGA as capacitor. Poly lactic-co-glycolic acid (PLGA) with 65:35 of lactide to glycolide ratio was used as dielectric materials. The glass

transition temperature of PLGA is about 39 °C which is similar to the temperature of the human body. The capacitance of PLGA changes around the glass transition due to the morphological change. The resonant frequency of LC oscillator changes and this change can be read out by observing the resonance peak of the reader coil coupled to the wireless heater using network analyzer (Agilent B1500A, Agilent Technologies, USA).

### 2.4.3 Mouse brain tumor model

All animal experiments were carried out under approval of Institutional Animal Care and Use Committees at Seoul National University Hospital. Human glioblastoma cell line (U87 MG) was purchased from the American Type Culture Collection (ATCC, Rockville, MD, USA) and stored in RPMI medium with 10% fetal bovine serum (FBS) at 37 °C. U87 MG glioblastoma cells ($2\times10^6$ cells/100 mL medium/mice) were subcutaneously transplanted into the thigh of 6-week old BALB/c nude mice (n = 26). 2 weeks after injection, the tumor tissue is monitored by MRI to measure tumor size and exact location.

### 2.4.4. Materials

All the materials were used as purchased unless stated. Starch from corn

(unmodified waxy corn starch of essentially pure amylopectin), sodium periodate ($NaIO_4$), poly lactic acid (PLA; $M_w$ ~260,000), Poly lactic-co-glycolic acid (PLGA; lactide:glycolide = 65:35, $M_w$ 40,000-75,000), phosphate buffered saline (PBS, 0.01M), polyimide (PI) precursor solution (poly(pyromellitic dianhydride-co-4,4′-oxydianiline), amic acid solution, electronic grade), and 1-metyl-2-pyrrolidinone (>99%) were purchased from Sigma Aldrich (USA). Also, glycerol is purchased from Samchun chemical (Korea), doxorubicin hydrochloride (DOX·HCl, Ildong pharm. Korea) was purchased from BK pharm (Korea) and polydimethylsiloxane base with curing agent (PDMS, sylgard 184) were purchased from Dow Corning (USA). For device fabrication, thermal evaporating source of Mg (>99.5%) was purchased from Taewon Scientific Co. (Korea), sputter target of ZnO (99.99%) was purchased from Thifine (Korea), Si wafer was purchased from 4Science (Korea), poly(methylmethacrylate) (PMMA A11) was purchased from MicroChem (USA) and positive photoresist S1805, AZ5214 and AZ4620 were purchased from AZ electronics Materials (USA).

### 2.4.5 Synthesis of oxidized starch (OST)

Sodium periodate ($NaIO_4$) was used for the oxidation agent for the synthesis of OST. Firstly, 2.14 g $NaIO_4$ was dissolved in 250 mL water. Then, various

amounts of starch depending were put into the solution. Next, 35-37 % hydrochloric acid was added to set the pH 3~4. The solution was strongly stirred under 40 °C overnight, synthesized OST was filtered and washed with DI water for 3 times. Final products were dried at 40 °C for 24 h under vacuum.

### 2.4.6 Fabrication of starch and OST patch containing DOX

For fabrication of normal starch patch, 1.5 g starch powder, 50 mg of DOX, 0.45 g of glycerol were dissolved in 40 g of water at 80 °C. The mixed solution is stirred for 30 min until a clear solution was obtained. The solution is then poured into 90 mm diameter petri dish and dried under 65 °C and 80% humidity for 48 h.

For the fabrication of OST patch containing DOX, 1.5 g OST powder and 50 mg DOX were dissolved in DI water and strongly stirred under 80 °C for the formation of imine linkage between OST and DOX. After 1 day, 0.45 g glycerol was dropwise into the solution. After 1 h, the solution was poured into the petri dish and dried under same condition.

### 2.4.7 DOX release profile from starch and OST *in vitro*

All the release profiles of DOX were measured by the absorbance of the

solution at 480 nm by using SpectraMax M3 (Molecular Devices, USA). All the patches had same size (square 20×20 $mm^2$) and contained 3.387 mg of DOX. Each patch was stored in 50 mL of 0.01 M phosphate-buffered saline (PBS) solution. The DOX concentration at each time was converted from the absorbance.

### 2.4.8 Fabrication of bioresorbable electronics on OST patch

Same mass of PI precursor solution and 1-metyl-2-pyrrolidinone were mixed to achieve diluted PI precursor solution. A sacrificial layer of PMMA was spin-coated (3000 rpm, 30s) on a Si wafer substrate and cured at 180 °C for 3 min. Then, the diluted PI precursor solution was spin-coated (3,000 rpm, 60 s) and cured at 250 °C for 2 h to form bottom PI layer. A ZnO thin film (2 nm) was deposited by RF sputtering under an Ar atmosphere (15 mTorr, 30W) as an adhesion layer. In sequence, 1.5 μm of Mg was deposited using a thermal evaporator (Scientech, Korea). Then, AZ5214 photoresist (PR) was spin-coated and patterned. The Mg was etched using an hand-made Mg etchant (nitric acid:DI water:ethylene glycol = 1:1:3 solution) to form electronic heater and temperature sensor metal pattern. The diluted PI precursor solution was again, spin-coated on the substrate (3,000 rpm, 60 s) and cured at 250 °C for 2 h to form top PI layer. Then, the sample was patterned using AZ4620 PR.

The PI was etched by oxygen plasma using a reactive-ion etcher (RIE, $O_2$, 100 sccm, 0.1 Torr, 100W; Scientech, Korea). After patterning the PI, the sacrificial layer of PMMA was undercut etched using boiling acetone. The floated device was then picked up by PDMS stamp (Sylgard 184, A:B = 10:1). The bottom PI layer was etched by oxygen plasma.

On the other hand, 3 wt% PLA or 8 wt% PLGA was spin-coated on top of the OST patch. The patch was exposed to the vapor of boiling chloroform to make the PLA or PLGA sticky. The device on the PDMS stamp was transferred onto the OST patch. Then, top PI layer was etched by oxygen plasma. Finally, PLA/PLGA was spin-coated (500 rpm, 30 s) again as a top encapsulation layer for protecting Mg-based electronic device.

### 2.4.9 Magnetic resonance imaging (MRI) protocol

For *in vivo* animal MR study, the tail vein was catheterized after anesthesia with 1.5-2% isoflurane/oxygen (v/v), and the animals were placed in the 9.4T MRI scanner (Agilent Technologies, USA). Throughout each imaging session, animals were wrapped in a warm water blanket and oxygen saturation and heart rate were monitored. A Milliped Coil (1-ch coil (Both RF transmission and signal reception); Agilent Technologies, Santa Clara, CA, USA) and a FSE (Fast Spin Echo) sequence for T2-weighted image was used. The

measurement parameters were as follows: TR = 3000 ms, effective TE = 30.82 ms, FOV = 20×35 mm, ETL = 4, matrix = 256×256, slice thickness = 1.0 mm.

### 2.4.10 BEP treatment procedure of mouse brain tumor model

Human brain tumors (U87-MG) implanted in BALB/c nude mice were grown to be ~4 mm radius for 3 weeks and resected, remaining tumor volume of ~20 $mm^2$. Then a BEP of 12 mm diameter containing 0.408 mg DOX (0.02 mg/g for body weight of mouse) was implanted on the residual tumors. After 1 day, thermal actuation of 30 min was treated once a day for 2 weeks. During the treatment, the volume of tumors was tracked using MRI every week. Four different types of treatment groups were set to investigate the therapeutic effects of BEP. The group of mice treated by an intravascular injection of DOX (IV), an implantation of BEP with RF heating but containing no DOX (Heater), an implantation of BEP containing DOX but no RF heating (Patch), and an implantation of BEP containing DOX combined with RF heating (Patch+Heater) were compared. IV group was set as an intravascular injection of an equivalent dosage of DOX right after the resection surgery.

### 2.4.11 *In vivo* biocompatibility of BEP

BEPs were implanted under the brain of the canine. After 10 weeks, the brain tissues containing the patch were extracted and stained with H&E and F4/80 antibody which is a macrophage marker.

### 2.4.12 DOX diffusion into tumor cells

*in vivo* DOX diffusion into tumor cells can be monitored by fluorescence imaging. BEP containing 20 mg DOX was implanted in subcutaneous tissue of mice. After each implantation time, BEP was detached from the tissue and the tissue was extracted for DOX assessment. A pulse which indicates thermal actuation of 30 min RF heating ($\Delta T = 5$ °C) was performed for experimental groups. Pulse 1 indicates one time of 30 min RF heating at the middle of implantation time, and pulse 4 indicates that multiple pulses were performed at each quarter of the total implantation time. Diffusion profiles of DOX in tissue were generated using LAS AF Lite (LEICA, USA) with a quadrangle block starting from the BEP-tissue interface and passing into the region of tissue containing DOX. Average fluorescence intensities at each distance were transformed into concentration through calibrations. For obtaining calibrations, excised fresh tumors with size of $3\times3\times2$ $mm^3$ were placed into a well with 34 μM of DOX in phosphate-buffered saline for 72 hours. The tumors were

removed from solution and prepared for frozen sectioning. DOX concentration remaining in the wells was measured using SpectraMax M3 (Molecular Devices, USA) as previously described. Actual concentration of DOX uptake by tumors was then calculated by subtraction and the value was corresponded with the sum of fluorescence intensity of tumor tissue.

## 2.5 References


1 Krex, D., Klink, B., Hartmann, C., von Deimling, A., Pietsch, T., Simon, M., Sabel, M., Steinbach, J. P., Heese, O., Reifenberger, G., Weller, M. & Schackert, G. Long-term survival with glioblastoma multiforme. *Brain* **130**, 2596-2606 (2007).

2 Cuddapah, V. A., Robel, S., Watkins, S. & Sontheimer, H. A neurocentric perspective on glioma invasion. *Nat. Rev. Neurosci.* **15**, 455-465 (2014).

3 Osswald, M., Jung, E., Sahm, F., Solecki, G., Venkataramani, V., Blaes, J., Weil, S., Horstmann, H., Wiestler, B., Syed, M., Huang, L., Ratliff, M., Karimian Jazi, K., Kurz, F. T., Schmenger, T., Lemke, D., Gömmel, M., Pauli, M., Liao, Y., Häring, P., Pusch, S., Herl, V., Steinhäuser, C., Krunic, D., Jarahian, M., Miletic, H., Berghoff, A. S., Griesbeck, O., Kalamakis, G., Garaschuk, O., Preusser, M., Weiss, S., Liu, H., Heiland, S., Platten, M., Huber, P. E., Kuner, T., von Deimling, A., Wick, W. & Winkler, F. Brain tumour cells interconnect to a functional and resistant network. *Nature* **528**, 93-98 (2015).

4 Chen, J., Li, Y., Yu, T.-S., McKay, R. M., Burns, D. K., Kernie, S. G. & Parada, L. F. A restricted cell population propagates glioblastoma growth after chemotherapy. *Nature* **488**, 522-526 (2012).

5 Stupp, R., Hegi, M. E., Mason, W. P., van den Bent, M. J., Taphoorn, M. J. B., Janzer, R. C., Ludwin, S. K., Allgeier, A., Fisher, B., Belanger, K., Hau, P., Brandes, A. A., Gijtenbeek, J., Marosi, C., Vecht, C. J., Mokhtari, K., Wesseling, P., Villa, S., Eisenhauer, E., Gorlia, T., Weller, M., Lacombe, D., Cairncross, J. G. & Mirimanoff, R.-O. Effects of radiotherapy with concomitant and adjuvant temozolomide versus radiotherapy alone on survival in glioblastoma in a randomised phase III study: 5-year analysis of the EORTC-NCIC trial. *Lancet Oncol.* **10**, 459-466 (2009).

6 Lawrence, Y. R., Li, X. A., el Naqa, I., Hahn, C. A., Marks, L. B., Merchant, T. E. & Dicker, A. P. Radiation dose–volume effects in the brain. *Int. J. Rad. Oncol* **76**, S20-S27 (2010).

7 Lesniak, M. S. & Brem, H. Targeted therapy for brain tumours. *Nat. Rev. Drug. Discov.* **3**, 499-508 (2004).

8 Parrish, K. E., Sarkaria, J. N. & Elmquist, W. F. Improving drug delivery to primary and metastatic brain tumors: Strategies to overcome the blood–brain barrier. *Clin. Pharmacol. Ther.* **97**, 336-346 (2015).

9 Westphal, M., Hilt, D. C., Bortey, E., Delavault, P., Olivares, R., Warnke, P. C., Whittle, I. R., Jääskeläinen, J. & Ram, Z. A phase 3 trial of local chemotherapy with biodegradable carmustine (BCNU) wafers (Gliadel wafers) in patients with primary malignant glioma. *Neuro Oncol.* **5**, 79-88

(2003).

10 McGirt, M. J., Than, K. D., Weingart, J. D., Chaichana, K. L., Attenello, F. J., Olivi, A., Laterra, J., Kleinberg, L. R., Grossman, S. A., Brem, H. & Quiñones-Hinojosa, A. Gliadel (BCNU) wafer plus concomitant temozolomide therapy after primary resection of glioblastoma multiforme. *J. Neurosurg.* **110**, 583-588 (2009).

11 Brem, H., Mahaley, M. S., Vick, J. N. A., Black, K. L., Schold, J. S. J., Burger, P. C., Friedman, A. H., Ciric, I. S., Eller, T. W., Cozzens, J. W. & Kenealy, J. N. Interstitial chemotherapy with drug polymer implants for the treatment of recurrent gliomas. *J. Neurosurg.* **74**, 441-446 (1991).

12 Woodworth, G. F., Dunn, G. P., Nance, E. A., Hanes, J. & Brem, H. Emerging insights into barriers to effective brain tumor therapeutics. *Front. Oncol.* **4** (2014).

13 Fung, L. K., Shin, M., Tyler, B., Brem, H. & Saltzman, W. M. Chemotherapeutic drugs released from polymers: Distribution of 1,3-bis(2-chloroethyl)-l-nitrosourea in the rat brain. *Pharm. Res.* **13**, 671-682 (1996).

14 Fung, L. K., Ewend, M. G., Sills, A., Sipos, E. P., Thompson, R., Watts, M., Colvin, O. M., Brem, H. & Saltzman, W. M. Pharmacokinetics of interstitial delivery of carmustine, 4- hydroperoxycyclophosphamide, and paclitaxel from a biodegradable polymer implant in the monkey brain.

*Cancer Res.* **58**, 672-684 (1998).

15 Hochberg, F. H. & Pruitt, A. Assumptions in the radiotherapy of glioblastoma *Neurology* **30**, 907-911 (1980).

16 Bettinger, C. J. & Bao, Z. Organic thin-film transistors fabricated on resorbable biomaterial substrates. *Adv. Mater.* **22**, 651-655 (2010).

17 Hwang, S.-W., Tao, H., Kim, D.-H., Cheng, H., Song, J.-K., Rill, E., Brenckle, M. A., Panilaitis, B., Won, S. M., Kim, Y.-S., Song, Y. M., Yu, K. J., Ameen, A., Li, R., Su, Y., Yang, M., Kaplan, D. L., Zakin, M. R., Slepian, M. J., Huang, Y., Omenetto, F. G. & Rogers, J. A. A physically transient form of silicon electronics. *Science* **337**, 1640-1644 (2012).

18 Boutry, C. M., Nguyen, A., Lawal, Q. O., Chortos, A., Rondeau-Gagné, S. & Bao, Z. A sensitive and biodegradable pressure sensor array for cardiovascular monitoring. *Adv. Mater.* **27**, 6954-6961 (2015).

19 Son, D., Lee, J., Lee, D. J., Ghaffari, R., Yun, S., Kim, S. J., Lee, J. E., Cho, H. R., Yoon, S., Yang, S., Lee, S., Qiao, S., Ling, D., Shin, S., Song, J.-K., Kim, J., Kim, T., Lee, H., Kim, J., Soh, M., Lee, N., Hwang, C. S., Nam, S., Lu, N., Hyeon, T., Choi, S. H. & Kim, D.-H. Bioresorbable electronic stent integrated with therapeutic nanoparticles for endovascular diseases. *ACS Nano* **9**, 5937-5946 (2015).

20 Kang, S.-K., Murphy, R. K. J., Hwang, S.-W., Lee, S. M., Harburg,

D. V., Krueger, N. A., Shin, J., Gamble, P., Cheng, H., Yu, S., Liu, Z., McCall, J. G., Stephen, M., Ying, H., Kim, J., Park, G., Webb, R. C., Lee, C. H., Chung, S., Wie, D. S., Gujar, A. D., Vemulapalli, B., Kim, A. H., Lee, K.-M., Cheng, J., Huang, Y., Lee, S. H., Braun, P. V., Ray, W. Z. & Rogers, J. A. Bioresorbable silicon electronic sensors for the brain. *Nature* **530**, 71-76 (2016).

21 Yu, K. J., Kuzum, D., Hwang, S.-W., Kim, B. H., Juul, H., Kim, N. H., Won, S. M., Chiang, K., Trumpis, M., Richardson, A. G., Cheng, H., Fang, H., Thompson, M., Bink, H., Talos, D., Seo, K. J., Lee, H. N., Kang, S.-K., Kim, J.-H., Lee, J. Y., Huang, Y., Jensen, F. E., Dichter, M. A., Lucas, T. H., Viventi, J., Litt, B. & Rogers, J. A. Bioresorbable silicon electronics for transient spatiotemporal mapping of electrical activity from the cerebral cortex. *Nat. Mater.* (**advance online publication)** DOI: doi:10.1038/nmat 4624

22 Stupp, R., Brada, M., van den Bent, M. J., Tonn, J.-C., Pentheroudakis, G. on be half of the ESMO Guidelines Working Group. High-grade glioma: ESMO clinical practice guidelines for diagnosis, treatment and follow-up. *Annals Oncol.* **25**, iii93-iii101 (2014).

23 Omuro, A. & DeAngelis, L. M. Glioblastoma and other malignant gliomas: A clinical review. *J. Am. Med. Assoc.* **310**, 1842-1850 (2013).

24 Tangpong, J., Miriyala, S., Noel, T., Sinthupibulyakit, C., Jungsuwadee, P. & St. Clair, D. K. Doxorubicin-induced central nervous system toxicity and protection by xanthone derivative of Garcinia Mangostana. *Neuroscience* **175**, 292-299 (2011).

25 J Bischof, J. C., Padanilam, J., Holmes, W. H., Ezzell, R. M., Lee, R. C., Tompkins, R. G., Yarmush, M. L. & Toner, M. Dynamics of cell membrane permeability changes at supraphysiological temperatures. *Biophys. J.* **68**, 2608-2614 (1995).

26 Landon, C. D., Park, J.-Y., Needham, D. & Dewhirst, M. W. Nanoscale drug delivery and hyperthermia: The materials design and preclinical and clinical testing of low temperature-sensitive liposomes used in combination with mild hyperthermia in the treatment of local cancer. *Open Nanomed. J.* **3**, 38-64 (2011).

27 White, M. G., Luca, L. E., Nonner, D., Saleh, O., Hu, B., Barrett, E. F. & Barrett, J. N. *Progress in Brain Research*, 347-371, Elsevier, Netherland (2007).

# Chapter 3. Integration of destructible resistive memory and multi-dye-sensitized upconverting nanoparticles for information security application

## 3.1 Introduction

Upconverting nanoparticles (UCNPs) are anti-Stokes-shift type light-emitting materials that absorb several long-wavelength-photons and convert them into a short-wavelength-photon[1,2]. Because of their high photochemical stability, sharp emission bandwidth, and large anti-Stokes shift (up to several hundred nanometers), these UCNPs have been highlighted as key materials in several photonic applications including biomedical imaging probes,[3-6] *in vivo* therapeutics[7-10], optogenetics[11,12], and optoelectronic devices[13,14]. However, well-known UCNPs, such as those based on a $NaYF_4$ matrix with lanthanide ion (*e.g.*, $Yb^{3+}$)[15,16], have a narrow and weak absorption band at ~975 nm by the quantized electron transition between the energy levels of $^2F_{7/2}$ and $^2F_{5/2}$ in the $Yb^{3+}$ ion[17,18]. The extension of their applications in emerging fields, including multi-modal imaging and high-performance electronics/optoelectronics, have been oftentimes limited by their narrow absorption bandwidth in the NIR range and weak photo-absorption[19].

Although efforts have been made to expand the absorption range of UCNPs, such as co-doping of $Nd^{3+}$ [17,20,21] or introduction of an organic dye[22-25], wide-wavelength-range absorption remains a challenge, and there is a need to widen the absorption band further towards the visible range. This expansion will enable UCNPs to take advantage of diverse light sources, which can facilitate their diverse applications and maximize the intensity of the upconverted light.

Here, we report multi-dye-sensitized UCNPs with dramatically widened photo-absorption bandwidths using sequential energy transfer. Multiple inter-ligand energy transfers between bound organic fluorescent dyes on the UCNP surface form an energy gradient, harvest photons of wide spectral ranges, and convey their energy to the nanoparticle. The absorption band of UCNPs is thereby extended from the near-infrared (NIR) to the entire visible range including red, green, and blue (RGB). Optimized inter-ligand energy transfer on the nanoparticle surface by controlling the spacing (total number of ligands on a UCNP) and ratio of the dye ligands maximizes the energy migration efficiency. As a representative application example, we demonstrate an information security technology by integrating the multi-dye-sensitized UCNPs mixed with ultraviolet (UV)-responsive photo-acid-generators (PAGs) on a destructible ultrathin resistive random access

memory (RRAM) device. Although the destruction of the transient electronics can be achieved by addition of triggering materials[26], the photo-triggered destruction based on a photo-sensitive solid state film provides a more facile erasure route of the data in RRAM device, which is great advantage in the mobile applications. The illumination of NIR and/or visible light on UCNPs triggers the emission of UV, and the photons are immediately transferred to the PAGs. Photo-acid is then generated and induces fast and complete chemical destruction of stored data in the RRAM device. The integration with multi-dye-sensitized UCNPs can diversify the activation light source of PAGs from only UV to broader range including UV, entire visible, and NIR. In addition, wavelength-selective and spatially-controlled device destruction and thereby localized etching of different electronic parts (*e.g.,* memory units and processing units) are enabled. This integrated system provides a novel concept of information security in nonvolatile data storage devices for consumer electronics, wearable electronics, and/or defense applications.

## 3.2 Result and Discussion

### 3.2.1 Overall system description

The UCNPs co-doped with $Yb^{3+}$ ions and UV/blue-emitting $Tm^{3+}$ ions (β-$NaYF_4$:20%Yb, 0.5%Tm) initially exhibit a narrow absorption band near ~975 nm and an emission spectrum at ~361 nm (~UV) and 450–471 nm (~blue) (**Figure 3.1a**), which is involved with a multi-photon absorption process (**Figure 3.1b**)[18]. Three types of sensitizers (sensitizer I: BODIPY-FL, sensitizer II: Cy3.5, sensitizer III: IR806), each composed of an energy harvesting aromatic fluorophore and a carboxylic acid for linkage to nanoparticles (the chemical structures are shown in **Figure 3.2a** and **Figure 3.3**), are bound to the surface of the UCNPs. As illustrated in **Figure 3.2a**, sensitizer I absorbs short-wavelength-photons (blue) and transfers the energy to sensitizer II (i). This energy is again delivered to sensitizer III (ii) and finally to the UCNP (iii). Similarly, longer-wavelength-photons (green and red) are absorbed by sensitizer II and III, and the corresponding energies are sequentially transferred to the UCNP. Photons in the NIR range are directly absorbed by the UCNP. Then, $Yb^{3+}$ ions in the particle upconvert the harvested energy and transfer to $Tm^{3+}$ ions in the same particle to yield a high energy (UV) photon (iv). Based on this energy transfer mechanism, the absorption band can be extended from a narrow range near ~975 nm to the

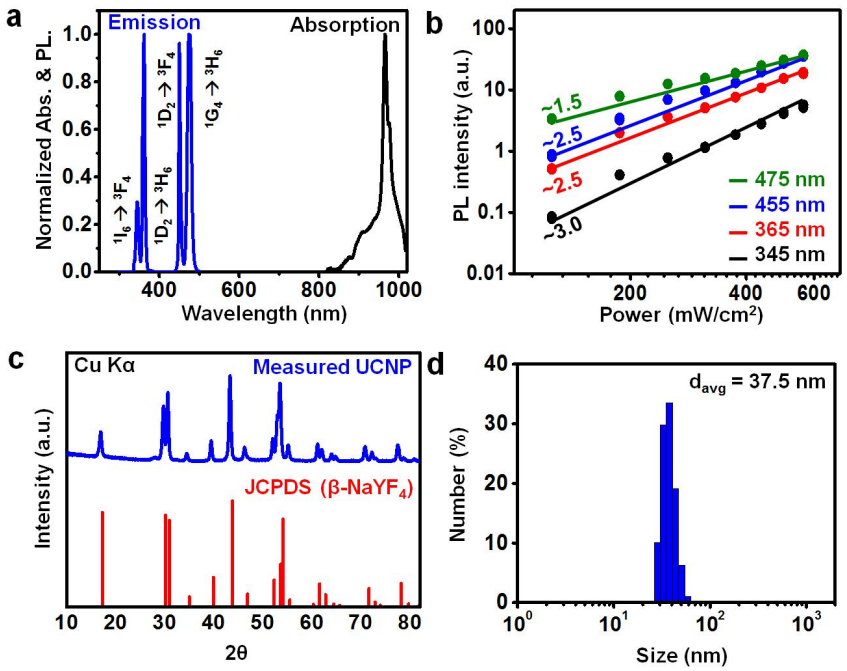


**Figure 3.1 Characterization of the β-$NaYF_4$:20%Yb,0.5%Tm UCNPs**

(a) Normalized absorption (~980 nm; black) and photoluminescence (~361 nm; UV / 471 nm; blue) spectrum of UCNPs. The photoluminescence is measured with the 980 nm laser at the power of 1 $mW/cm^2$. (b) Plot of the intensity of upconverted photoluminescence versus the laser power. (c) Synthesized (blue) and reported (red) X-ray diffraction pattern for hexagonal $NaYF_4$ nanoparticles. (d) Normalized size measurement of the synthesized nanoparticle using DLS.

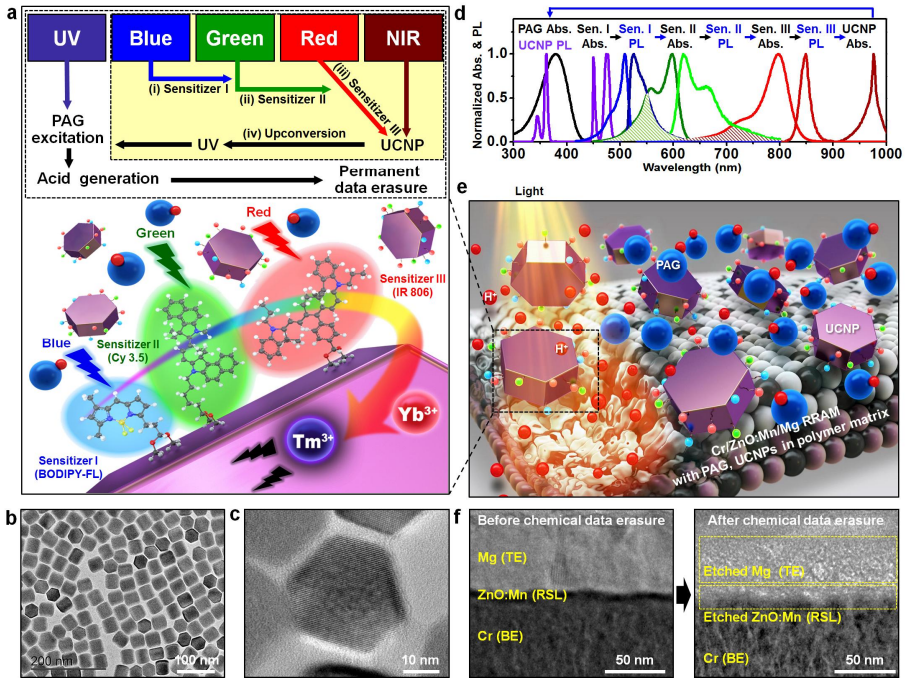


**Figure 3.2 Design of multi-dye-sensitized UCNPs and integration with ultrathin nonvolatile memory for advanced information security**

(a) Design of multi-dye-sensitized UCNPs for wide-range photo-absorption and upconversion. Schematic diagram of the energy flow (top) and three dye sensitizers bound to a UCNP (bottom). (b) TEM image of the multi-dye-sensitized UCNPs. (c) High-resolution TEM image of the multi-dye-sensitized UCNP. (d) Normalized absorption and photoluminescence spectra of the UCNP, sensitizers I, II, III, and normalized absorption spectrum of the PAG. (e) Schematic illustration of the photo-induced unrecoverable data erasure in the ultrathin nonvolatile memory device with UCNPs for

advanced information security. (f) Cross-sectional TEM images before (left) and after (right) light-induced chemical destruction of the ultrathin nonvolatile memory.

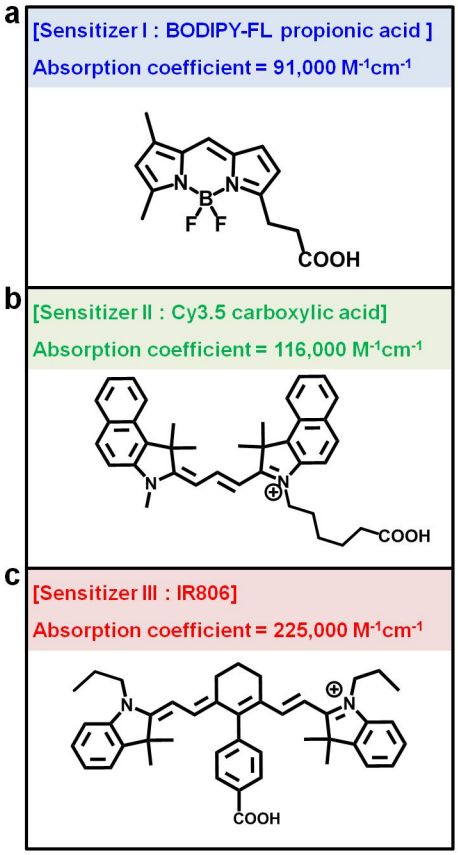


**Figure 3.3 Molecular structure and absorption coefficient of fluorescent dye sensitizers for multi-dye-sensitized UCNPs**

(a) Sensitizer I (blue). (b) Sensitizer II (green). (c) Sensitizer III (red).

entire visible and NIR range. Furthermore, maximizing the chance of energy absorption by utilizing a large photo-absorption bandwidth with high absorption coefficients increases the upconverted output emission intensity in the UV range. The sequential energy migration between sensitizer I, II, III, and the UCNP is mainly based on Förster resonance energy transfer (FRET), whose efficiency is maximized when the distances between coupled dyes are maintained at less than the critical FRET distance[27]. Other types of energy transfer (*e.g.* Dexter electron transfer) may occur, however, are less likely dominant process since the inter-ligand distance of fluorescent dyes is around several nm.

Spatially-confined sensitization of multiple dyes on a single nanoparticle through the controlled ligand exchange reactions is thereby a key factor of this sequential energy transfer. Minimization of the inter-ligand distance on the nanoparticle surface by changing the reactant amount (total number of ligands on a UCNP) and the ratio of dyes increases the energy migration efficiency. The UCNPs were synthesized by following the previously reported method[4]. High-resolution transmission electron microscopy (TEM) images of these multi-dye-sensitized UCNPs are presented in **Figure 3.2b** and **3.2c** (the crystal structure and size of the nanoparticles are shown in **Figure 3.1c** and **3.1d**, respectively). Multi-dye-sensitization of UCNPs is performed *via* ligand

exchange reactions (see Experimental section for details). Three fluorescent dyes (sensitizer I, II, and III) are chosen to be sensitized on UCNPs. These dyes have sufficient overlaps between their emission and absorption spectra (**Figure 3.2d**) and high absorption coefficients (**Figure 3.3**). The absorption spectrum of sensitizer I is in the 420–530 nm range (~blue), and its emission spectrum (500–650 nm) is well overlapped with the absorption spectrum of sensitizer II (470–650 nm). Therefore, sensitizers I and II act as a FRET donor and acceptor pair. Similarly, sensitizers II and III are paired as a FRET donor and acceptor, respectively. The three ligands and the UCNP itself cover the entire visible and NIR spectral range for the photo-absorption process.

As a representative application example, the multi-dye-sensitized UCNPs were applied for advanced information security of data storage devices. As mobile electronics such as wearable electronics[28,29] and personal smart devices[30], have emerged in many applications, nonvolatile data storage devices[31,32] have become key modules in electronic systems. However, the security of the information stored in mobile electronics is not sufficient. Although the data stored in nonvolatile memory can be electrically erased for security purpose, they can be easily restored[33]. Important information in missing and/or stolen memory chips cannot be protected. Alternatively, chemical destruction of the nonvolatile memory device[34] and/or related

electronics[26,35-37] under emergency situations makes the data unrecoverable. A simple coating of a multi-dye-sensitized UCNP/PAG/poly(ethylene oxide) (PEO) matrix on an ultrathin acid-destructible RRAM enables wide-excitation-range photo-induced acid generation and subsequent chemical destruction in an integrated system (**Figure 3.2e**). The ultrathin RRAM is composed of a Mg top electrode (TE), a sub-10-nm-thick ZnO (doped with 3 wt% Mn) resistance switching layer (RSL), and a Cr bottom electrode (BE) (**Figure 3.2f left**). Photons in wide range radiated onto the matrix are converted into UV light that triggers acid-generation (**Figure 3.2e**). The ultrathin Mn-doped ZnO RSL exhibits stable operation, while rapidly disappearing in an acidic environment[38] for the chemical data erasure (**Figure 3.2f right**).

### 3.2.2 Characterization of upconverting nanoparticles

The sensitizer ligands and the UCNP itself harvest photons whose energies correspond to ~2.4 (~blue), ~2.0 (~green), ~1.6 (~red), and ~1.3 eV (NIR). The energy levels are located adjacent to each other and form an energy gradient through which absorbed energy is sequentially transferred to the UCNPs (**Figure 3.4a**). The collected energy from multiple photons of various wavelengths is conveyed to $Yb^{3+}$ ions and used for upconversion into a high-energy UV photon through the $Tm^{3+}$ activator. The multi-dye-sensitization is successfully achieved and widens photo-absorption from the NIR range only (non-sensitized UCNPs) to the NIR, R, G, and B ranges (sensitized UCNPs) (**Figure 3.4b**).

Because all sensitizers are co-located on the spatially confined surface of a nanoparticle, the distances between ligands are close enough for FRETs to occur. The inter-ligand FRETs are confirmed through time-resolved photoluminescence (PL) decay measurements. For double-ligand nanoparticles with a ligand ratio of 1:1 (sensitizer I:II), time-resolved PL measurement at 550 nm (emission of sensitizer I) shows a decreased decay time-constant ($\tau$) from 4.94 ns (control; without sensitizer II) to 3.31 ns (experiment; with sensitizer II), which is due to an additional decay path *via* FRET between sensitizer I and II (**Figure 3.5a**)[39]. Another type of double-

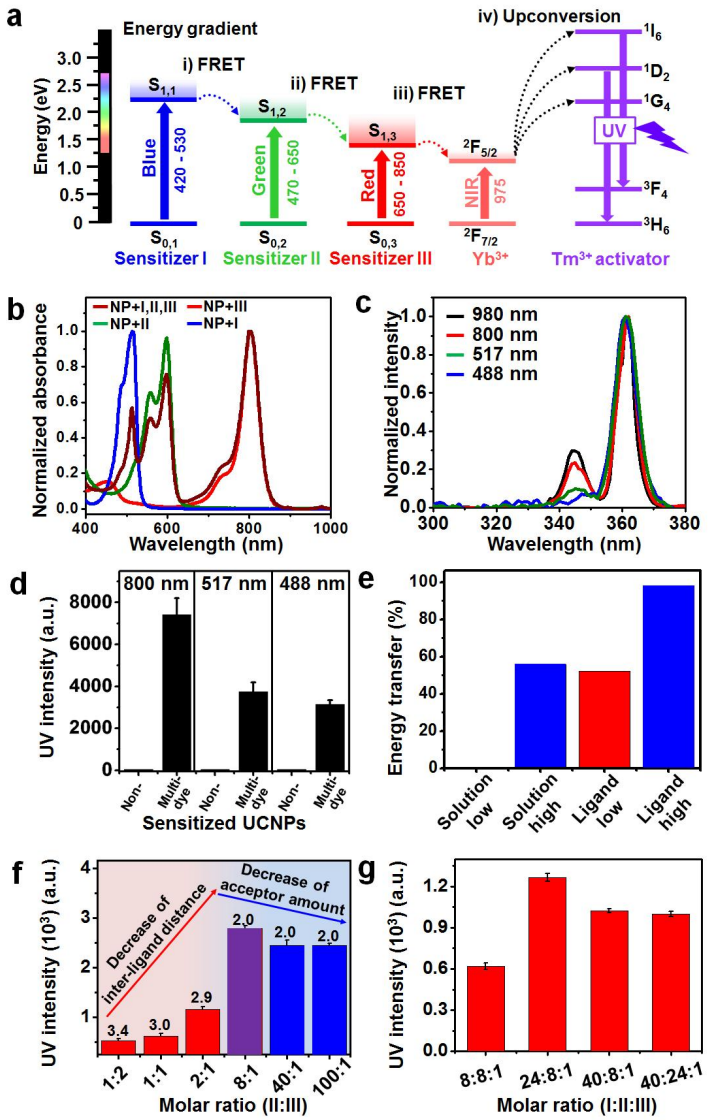


**Figure 3.4 Characterization and optimization of the sequential energy transfer in multi-dye-sensitized UCNPs**

(a) Energy diagram of the three sensitizers and ions of the UCNP. The bold bars represent the energy levels, and the arrows represent the sequential

energy transfer. (b) Normalized absorption spectra of the UCNPs for various sensitizing conditions. The inset shows a 25-times magnified view of the spectra at ~975 nm. (c) Normalized emission spectra of multi-dye-sensitized UCNPs under 980, 800, 517, and 488 nm laser excitations. The laser power density is 25 $mW/mm^2$ in all cases. (d) Output UV intensity (361 nm) of the non-sensitized and multi-dye-sensitized UCNPs (1.6 mg/mL) which are excited by 800, 517, and 488 nm laser sources. The laser power density is 25 $mW/mm^2$ in all cases. (e) Comparison of energy transfer efficiencies of sensitizer I and II dispersed in the solution (left) and bound to the nanoparticle surface (right). The efficiencies were measured by using the donor (sensitizer I) fluorescence intensity in absence and presence of the acceptor (sensitizer II). The concentration of both ligands are $10^{-5}$ M for the low concentration and $10^{-3}$ M for high. (f) Upconverted UV emission intensity from double-ligand UCNPs (1.6 mg/mL). Molar ratios of sensitizer II and III range from 1:2 to 100:1. The 517 nm laser power density is 25 $mW/mm^2$. The number written above the red bar indicates the calculated inter-ligand distances (nm). (g) Upconverted UV emission intensity from UCNPs (1.0 mg/mL) under various molar ratios of sensitizer I, II, and III. The 488 nm laser power density is 25 $mW/mm^2$.

ligand nanoparticles (sensitizers II:III with a molar ratio of 1:1) exhibits a similar decrease in $\tau$ of sensitizer II from 1.7 to 1.11 ns (**Figure 3.5b**). Sensitization of UCNPs with sensitizer I, II and III enables UV emission excited by various light sources ranging from the visible to NIR range (488, 517, 800, and 980 nm), as demonstrated in **Figure 3.4c**. The multi-dye-sensitized UCNPs exhibit UV emission by excitation at 800 nm, 517 nm, and 488 nm (**Figure 3.4d**) while the non-sensitized UCNPs show no emission. The upconversion using previously unused photons (RGB) will provide many new possibilities in various applications. FRET is mediated by the dipole-dipole coupling between an energy donor and acceptor, and its efficiency is inversely proportional to the sixth power of the distance between ligands[40]. Therefore, control of the optimized distance between dyes on the nanoparticle plays a critical role in the efficient energy transfer and upconversion process. Thus, we characterized the FRET efficiencies between sensitizers I and II, and sensitizers II and III, respectively, under various inter-ligand distances. The sensitizers were dispersed in a poly(methyl methacrylate) (PMMA) matrix since the distance between sensitizers can be controlled by changing the concentration, and calculated by dividing the volume of PMMA by the total number of dye molecules.

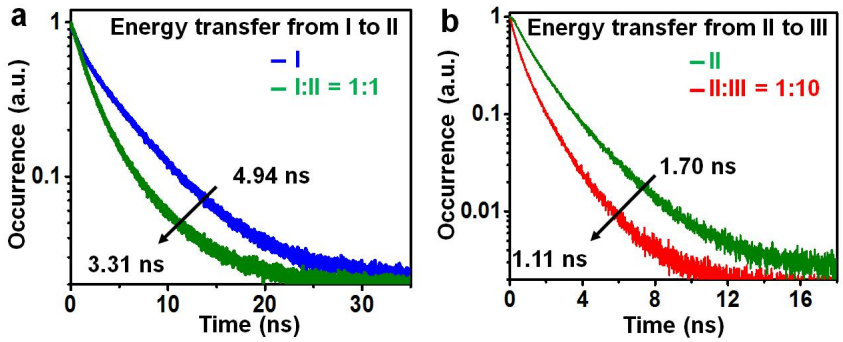


**Figure 3.5. Inter-ligand FRETs in double-ligand nanoparticles**

(a) Time-dependent decay of the emission from UCNP/sensitizer I and UCNP/sensitizer I+II measured at 550 nm with an excitation source of 400 nm. (b) Time-dependent decay of the emission from UCNPs/sensitizer II and UCNPs/sensitizer II+III measured at 650 nm with an excitation source of 500 nm.

As the inter-molecular distance decreases, the energy transfer efficiency increases with a sudden jump at ~6 nm for sensitizers I and II and at ~4 nm for sensitizers II and III (**Figure 3.6**). These intermolecular distances correspond to the critical FRET distance for each sensitizer pair. To achieve this short inter-ligand distance, spatial confinement of ligands on nanoparticles is important. **Figure 3.4e** compares the measured FRET efficiencies between donor (sensitizer I) and acceptor (sensitizer II) dispersed in the solution and sensitized on UCNPs. The efficiency ($E$) is measured by $E = 1 - (F / F_0)$, where the $F$ and $F_0$ indicate the donor fluorescence intensity with and without an acceptor, respectively. In each case, two different concentrations of dyes (low and high; both ligands have the same concentration of $10^{-5}$ M and $10^{-3}$ M, respectively) were used to compare the effect of inter-ligand distances. The most effective energy transfer is achieved when the ligands are bound to the surface of UCNPs at high concentration because the inter-molecular distance between two different ligands on the surface of the UCNPs is shortest among all four cases. Even at the low dye concentration, FRET occurs effectively when the ligand is bound to the surface of UCNPs. We also optimized ligand exchange reactions on the nanoparticle surface to maximize the light absorption and by increasing the number of dyes on a single UCNP. The total number of dyes on the surface of

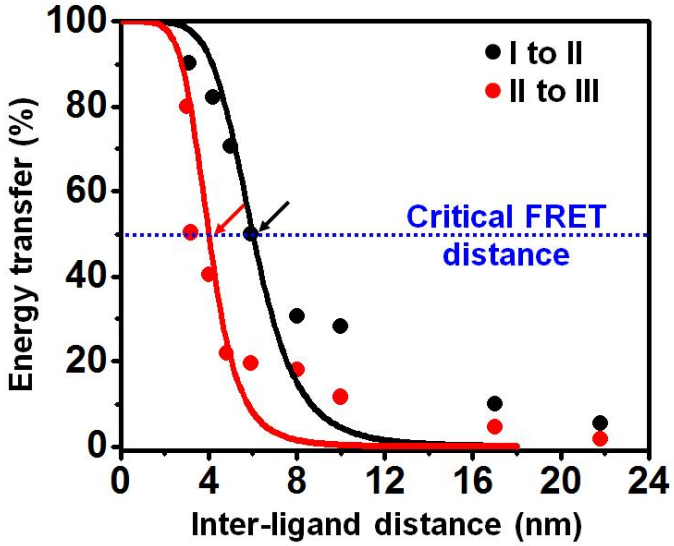


**Figure 3.6 Plot of measured (dots) and calculated (lines) energy transfer efficiency versus inter-ligand distance in the solid state film.**

each UCNP was calculated by dividing the concentration of the dye-sensitizer (calculated from photo-absorbance data) by the number density of nanoparticles (calculated from ICP data). The area assigned for a dye was determined by dividing the surface area of a UCNP by the number of dye-sensitizers bound to it. Then, the inter-ligand distance is derived by taking a square root of the calculated value. More detailed calculation procedures of the inter-ligand distance are described in Experimental Section. The optimized inter-ligand distance is 2.87 nm, which is similar to the critical FRET distance (**Figure 3.6**). This short inter-ligand distance plays an important role in maximizing the FRET efficiency and sequential energy transfer to UCNPs. In this optimized reaction condition, the UV emission intensities of double-ligand nanoparticles with various ratios of sensitizers II and III were compared. The UV emission by the upconversion is maximized at II(donor):III(acceptor) molar ratio of 8:1 (**Figure 3.4f**) where the inter-ligand distance and the acceptor amount are balanced. At the left region (high III ratio), the inter-ligand distance decreases since the total number of ligands increases (**Figure 3.7**). When the inter- ligand distance reaches the minimum, the total amount of energy transfer decreases as the acceptor amount decreases (right region). This experimental result agrees well with the calculated values that are numerically derived from the FRET data using a model of a round-

| Sample | Absorbance | Concentration of UCNPs (nM) | # of ligand on UCNP surface | Area/ligand ($nm^2$) | Average inter-ligand distance (nm) |
|---|---|---|---|---|---|
| **Acid, 3:30** | 1.394 | 7.90 | 646 | 8.2 | 2.87 |

**Table 3.1 Optimized inter-ligand distances.**

shaped nanoparticle with randomly-spread ligands (**Figure 3.8a, 3.8b and 3.8c**, details are in Experimental Section). Based on this optimized II:III ratio, we further optimized the sensitizer I:II:III ratio for the excitation at 488 nm. The maximum UV intensity excited at 488 nm is achieved at the molar ratio of 24:8:1 (sensitizer I:II:III) as shown **Figure 3.4g**. Excess amount of sensitizer I can reduce the quantum yield due to enhanced back energy transfer between $Tm^{3+}$ and sensitizers (**Figure 3.7,** details are in Experimental Section). The UV emission quantum yield is less than 0.1%, which is mainly due to the low quantum yield[41] of UCNP itself.

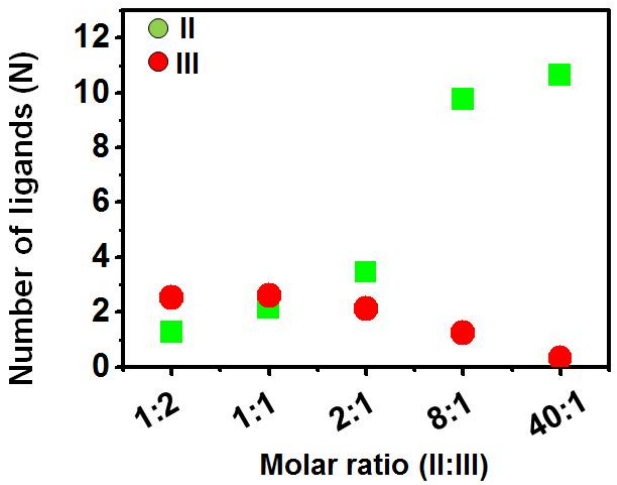


**Figure 3.7 Calculated number of conjugated sensitizer II and III on UCNP with respect to the molar ratio control.**

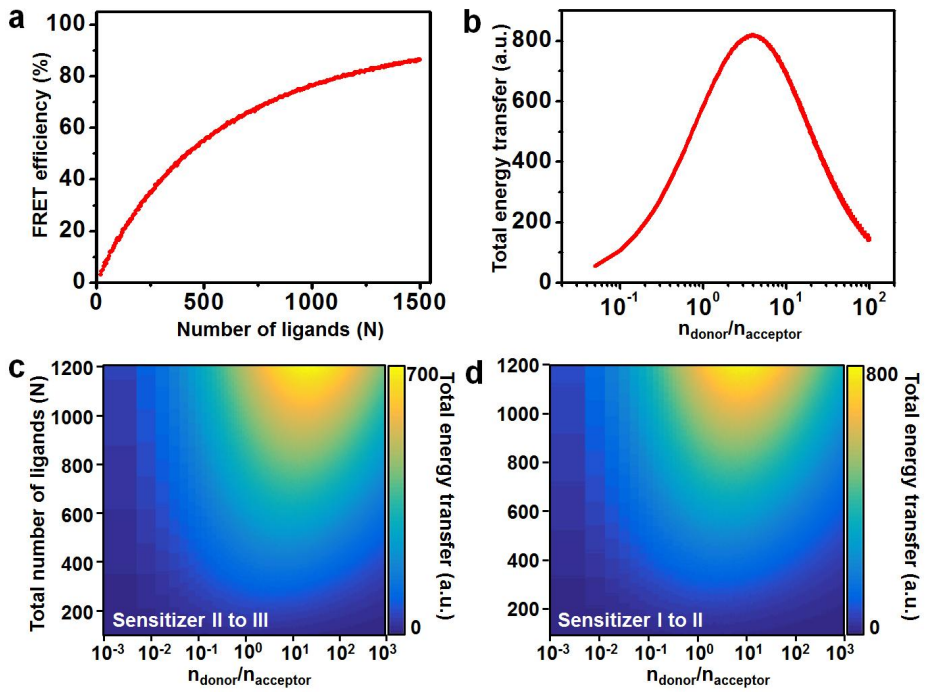


**Figure 3.8 Simulated FRET efficiency and total energy transfer**

(a) Plot of simulated FRET efficiency versus number of ligands in case of $r$ = 30 nm, $R_0$ = 6 nm, and the ratio of donor to acceptor ratio of 1 to 5. (b) Plot of simulated total energy transfer versus donor to acceptor ratio in case of $r$ = 30 nm, $R_0$ = 6 nm, and $N$ = 1200. (c) Plot of simulated total energy transfer versus donor to acceptor ratio, the number of ligands on a UCNP in case of the FRET from II to III. (d) Plot of simulated total energy transfer versus donor to acceptor ratio, the number of ligands on a UCNP in case of the FRET from I to II.

### 3.2.3 Characterization of upconverting nanoparticles

We integrated the multi-dye-sensitized UCNPs with ultrathin data storage devices (RRAM) to develop a memory system featured with a novel function of unrecoverable data erasure. The system was constructed by integrating a photo-induced acid-generating layer with an ultrathin RRAM. The memory module was fabricated on an array of single-crystalline silicon (Si) transistors and is coated with the acid-generating layer, which was a mixture of the UCNPs and PAG dispersed in PEO medium (see **Figure 3.9a** for a cross-sectional TEM image of the integrated system). We designed and fabricated an ultrathin RRAM (Cr/ZnO:Mn/Mg; inset of **Figure 3.9a,** others in **Table 3.2**) that can be rapidly dissolved under the acidic condition. In addition to the intrinsic dissolvable nature of Mg and ZnO, the ultrathin thickness of the RSL (< 10 nm) facilitates fast chemical destruction[35]. It is important to minimize the thickness of the ZnO:Mn layer, because the dissolution rate of ZnO is 3–4 times slower than that of Mg (**Figure 3.10**). Detailed information about the chemical reaction mechanisms (**Figure 3.11a**) and characterization results of PAG (**Figure 3.11b** for UV-vis spectroscopy and **Figure 3.11c** for $^{1}$H NMR) are presented in the Experimental section. **Figure 3.9b** exhibits a representative current–voltage (*I–V*) curve before (red and blue) and after (black) the chemical destruction (permanent data erasure). The forming

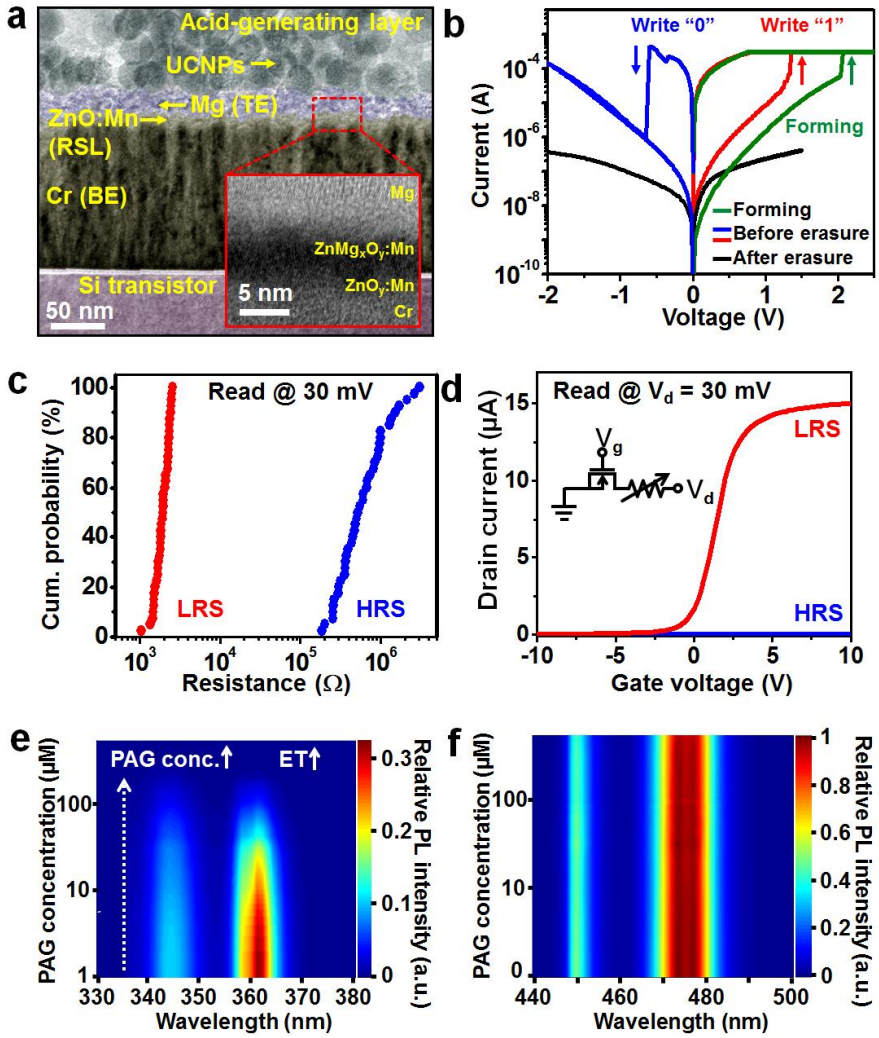


**Figure 3.9 Integration of UCNPs with the ultrathin RRAM**

(a) Cross-sectional TEM image of the integrated system (RRAM on the Si transistor coated with UCNPs/PAG/PEO layer). (b) *I–V* curve of the Cr/ZnO:Mn/Mg RRAM before and after photo-induced chemical destruction. (c) Cumulative probability plot of resistances of low resistance state (LRS)

and high resistance state (HRS) at read voltage of 30 mV. (d) Plot of drain current ($I_d$) versus gate voltage ($V_g$) of the integrated Si transistor and RRAM (1T1R) device in the LRS and HRS. The applied drain voltage ($V_d$) was 30 mV. (e) UV emission spectra from UCNPs in the solution of PAG and chloroform with various PAG concentrations. (f) Blue emission spectra from UCNPs in solution of PAG and chloroform with various PAG concentrations.

| Bottom | Oxide | Top | Switching | etc |
|---|---|---|---|---|
| **Mg** | **MgO** | **Mg** | **O** | |
| Mg | ZnO | Mg | X | |
| Mg | ZnO:Mn | Mg | X | |
| Al | MgO | Mg | X | |
| Al | ZnO | Mg | X | |
| Al | ZnO:Mn | Mg | O | unstable switching |
| Cr | MgO | Mg | X | |
| Cr | ZnO | Mg | X | |
| **Cr** | **ZnO:Mn** | **Mg** | **O** | |
| Au | MgO | Mg | O | Too high turn on voltage |
| Au | ZnO | Mg | X | |
| Au | ZnO:Mn | Mg | X | |

**Table 3.2 List of the selected layer information for memory application.**

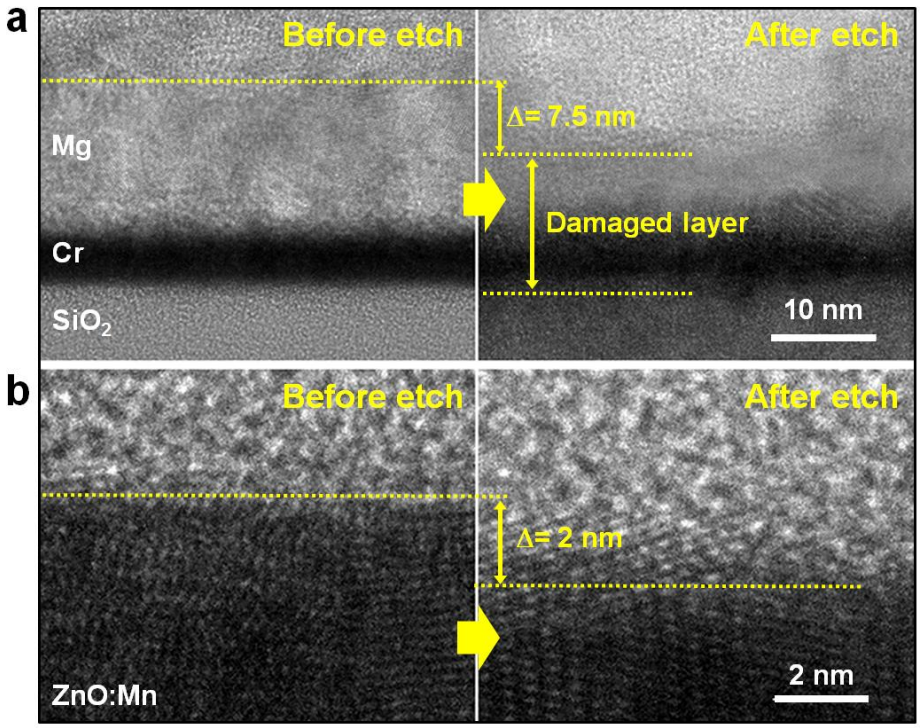


**Figure 3.10 Comparison of dissolution speed between Mg and ZnO:Mn**

(a) Cross-sectional TEM image of Mg and (b) ZnO:Mn thin film before (left) and after (right) photo-induced chemical etching. Both layers are covered with the UCNPs/PAG/PEO matrix.

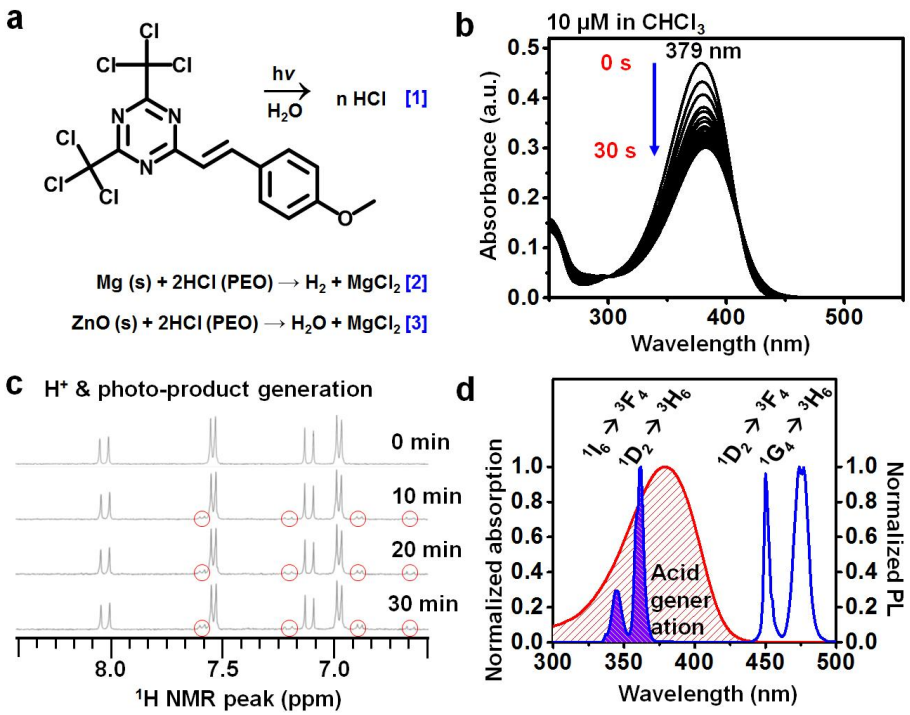


**Figure 3.11 Characterization of photo-acid-generator (PAG)**

(a) Molecular structure and chemical reactions of PAG with dissolvable materials such as Mg and ZnO. (b) Absorption spectra of PAG with different UV illumination time. (c) NMR spectra of PAG in $CDCl_3$ solution with different UV illumination time. (d) Normalized absorption of the PAG and normalized photoluminescence of the UCNPs.

process (green) induces the memory device to have a bipolar behavior with a low operating voltage (between -2 and 1.5 V). After chemically dissolving the TE and RSL, the device exhibits a zero on/off ratio, which means a permanent loss of the stored data. **Figure 3.9c** presents a cumulative probability plot, which reveals uniform switching behaviors over entire pixels in the 12 × 12 array while maintaining a large memory operation window (two orders of difference between on and off). We employed single-crystalline Si nano-membrane transistors[31,42]. By integration of the RRAM device with the Si transistor (**Figure 3.9d**), the memory array can be operated (**Figure 3.12**).

For facile and selective chemical destruction of the ultrathin RRAM, photo-responsive acid generation has been utilized[43]. UV emission from the UCNPs in the PAG solution decreases dramatically as the PAG concentration increases (**Figure 3.9e**) due to UV absorption by the PAG (left blue peaks in **Figure 3.11d**), whereas blue emission from the UCNPs, which is not absorbed by the PAG (right blue peaks in **Figure 3.11d**), maintains its original intensity (**Figure 3.9f**). The acidic environment generated by the solid-state PAG and UCNP film was strong enough to etch Mg (the TE of the RRAM), which can be inferred from the sudden increase of resistance of the Mg film (**Figure 3.13a**). The 1:2 ratio of PAG:PEO enabled the fastest dissolution of the Mg TE. Wavelength-selective and/or spatially-controlled destruction of

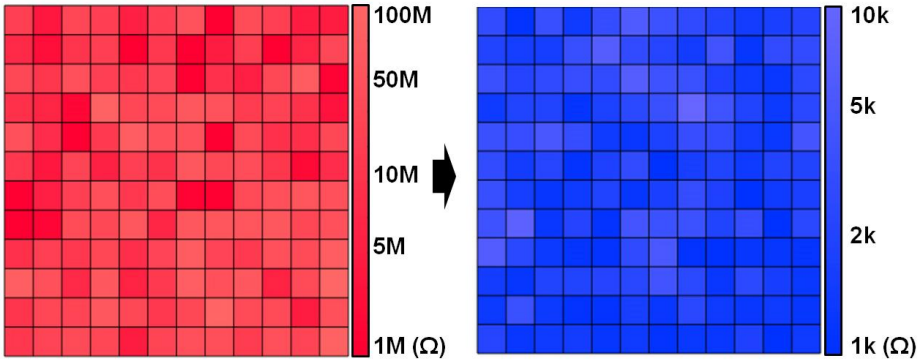


**Figure 3.12 Resistance distribution of the HRS (left) and LRS (right) of 1T1R array.**

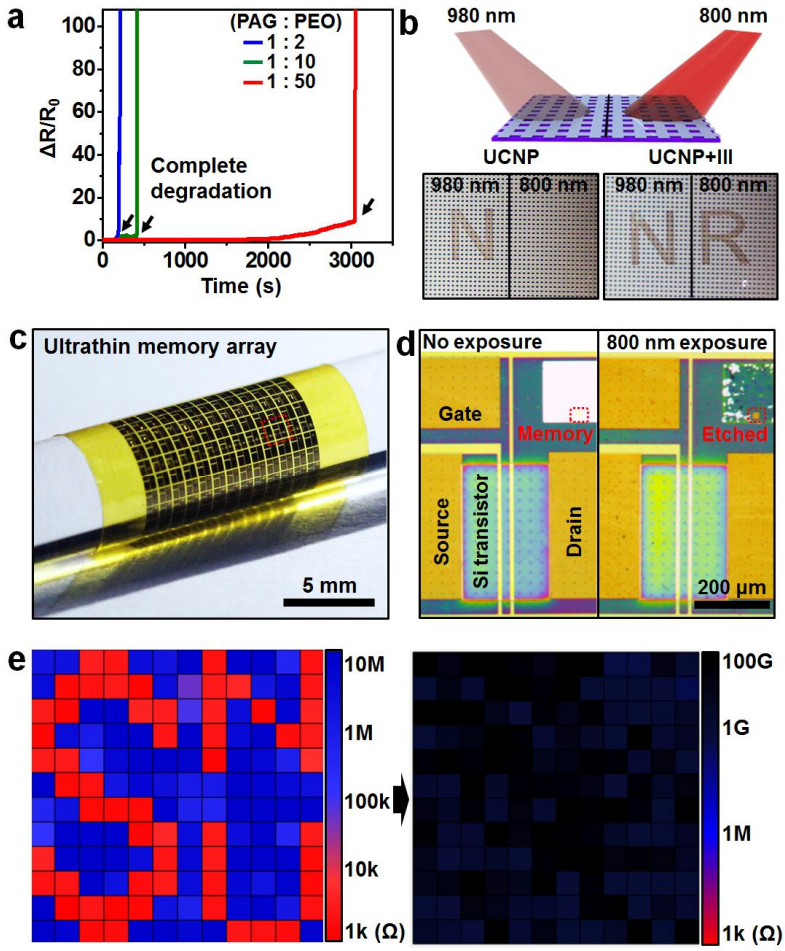


**Figure 3.13 Integration of UCNPs with the ultrathin RRAM**

(a) Resistance change of dissolvable electrodes under various PAG and PEO compositions. (b) Images of the etched Mg layer coated with UCNPs (left) and UCNP/sensitizer III (right) by exposure to 980 nm and 800 nm laser with the same power density of 25 mW/mm$^2$. (c) Image of the integrated device array on a flexible plastic substrate. (d) Magnified view of the integrated

device without light exposure (left) and with light exposure (right) for photo-induced chemical destruction. The degraded region corresponds to the TE and RSL of the memory. 800 nm laser with the power density of 25 $mW/mm^2$ was used as the light source. (e) Information (SNU) stored in the memory array (left) and unrecoverable erasure of the stored data by photo-induced chemical destruction (right) at the read voltage of 30 mV.

the electronics is also possible. Namely, several selected parts of the entire degradable electronic system (*e.g.*, memory and processing parts) can be destroyed independently by changing the illumination wavelengths and/or area. When two selected parts of the electronics are coated with different ligands at different regions (**Figure 3.13b**; non-sensitized UCNPs coated on the left side and UCNPs with sensitizer III on the right side), irradiation of the 365 nm or 980 nm light leads to etching of all electronics, whereas illumination of the 800 nm light only destroys the right side.

We integrated the UCNPs/PAG/PEO with the flexible RRAM array (**Figure 3.13c**). Because of the ultrathin nature of the electronics, the entire system is deformable and can be integrated on various curvilinear surfaces including the human skin (**Figure 3.14a**). The technologies presented in this work, can thus be applied to conventional Si-based memory modules as well as next-generation memory devices including deformable ones[28,30,31] Illumination of the 800 nm light yields successful breakdown of the system (**Figure 3.13d**). The stored data in the memory array (**Figure 3.13e left**) can be completely erased by chemically dissolving the memory device (**Figure 3.13e right**). Units for wireless triggering of photo-illumination and dissolution of electronics can also be integrated (**Figure 3.14b** and **3.14c**). This novel system achieves enhanced information security through unrecoverable data erasure.

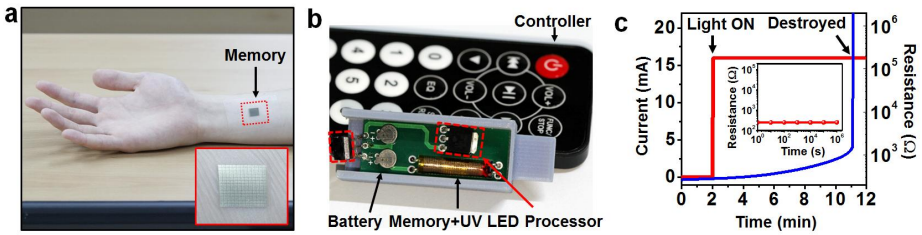


**Figure 3.14 Photo-induced destructible RRAM in the wearable and wireless form**

(a) Ultrathin destructible RRAM on the human skin. (b) Image of the integrated memory array with battery and wireless control unit for mobile applications. (c) Plot of current of the UV lamp (red) and the resistance of device (blue) versus time of a Mg electrode in the wireless device with light illumination and without (inset) light illumination.

## 3.3 Conclusion

Multi-dye-sensitization of UCNPs can dramatically widen their photon absorption window from only the NIR range (975 nm) to the entire visible and NIR range (450–975 nm). This expansion enables photons of diverse initial energies to be used for upconversion into a high energy photon. Optimization of the sensitizer ligand distance and ratio further increases the efficiency of the sequential energy transfer and photo-upconversion process. Absorption of diverse-energy photons that cannot be used in conventional UCNPs maximizes the utility of UCNPs. As a representative application example, the sensitized UCNPs together with the PAG are used as a new information security module in data storage devices with a function of unrecoverable data erasure. The upconversion by UCNPs using previously unused photons (RGB) would provide numerous new opportunities for their applications.

## 3.4 Experimental

### 3.4.1 Numerical modelling of the FRET efficiency

We used a round-shaped nanoparticle model with randomly-spread ligands to estimate the FRET efficiency. In this model, we assumed that the shape of the nanoparticle is spherical, the radius of $r$, the energy transfer dominantly occurs between the two closest ligands, and the ligands are randomly located on the surface of the nanoparticle with the total number of $N = N_D + N_A$ and the donor:acceptor ratio of $R_{D/A} = N_D / N_A$ (where $N_D$ and $N_A$ are the number of donor and acceptor, respectively). The location of ligands on the nanoparticle is determined by a random function using the Matlab program (MathWorks, USA). The closest inter-ligand distance ($d_n$) of two sensitizers is defined as follows.

$$d_n = \min_{\forall acceptor} \| \text{point}_{donor^{(n)}} - \text{point}_{acceptor} \|_2 \quad (1)$$

Based on the measurement data, $R_0$ was calculated. The FRET efficiency depends on the intermolecular distance between the donor and acceptor based on the law of dipole–dipole coupling

$$\varepsilon_n = \frac{1}{1 + \left( \frac{d_n}{R_0} \right)^6} \quad (2)$$

where $R_0$ represents the critical FRET distance between the donor and acceptor which affects the energy absorbed initially. Iteration of the $\mathrm{cycle}$ imposes an averaging effect of the random samplings. Therefore, $\bar{\varepsilon}$ is expressed as a following equation.

$$\bar{\varepsilon} = \frac{1}{cycle} \sum_{cycle=1}^{cycle} \sum_{n=1}^{n_{donor}} \varepsilon_n \quad (3)$$

The total energy transfer ($E$) can be achieved by multiplying the efficiency with the number of donor ($n_{donor}$).

$$E = n_{donor} \bar{\varepsilon} \quad (4)$$

The $E$ and thereby the FRET efficiency increase as the number of ligands increases (**Figure 3.9a**). As $R_{D/A}$ decreases, the simulated FRET efficiency ($\bar{\varepsilon}$) decreases while the absorption of the donor increases. Therefore, the amount of total energy transfer ($E$) which is related to the UV intensity reaches its maximum (**Figure 3.9b**). It agrees well with the experimental result in Figure 2f. $E$ as a function of $R_{D/A}$ and $N$ are plotted in **Figure 3.9c** (FRET from sensitizer II to III) and **Figure 3.9d** (FRET from sensitizer I to II).

### 3.4.2 Characterization of the PAG

Illumination of the UV light by using the 365 nm lamp to the PAG induces acid generation, resulting from photo-degradation of PAG molecules. Because the degraded products of PAG molecules exhibit lower photo-absorption coefficients than the initial non-reacted PAG molecules, the UV absorption decreases as the light exposure time increases. As the degraded products increases, which appear during photo-acid generation, new peaks arise in the $^{1}H$ NMR spectra (the red circles in **Figure 3.12**; Avance-300, Bruker, Germany).

### 3.4.3 Demonstration of the mobile data storage with a wireless triggering unit

A wireless controller chip, phototransistor, ultrathin RRAM, and UV light-emitting diode (LED) were integrated on a USB-sized printed circuit board (**Figure 2.15b**). The LED covered the entire area of the RRAM for efficient illumination. The command signal for the destruction is transmitted from the controller to mobile data storage devices integrated with LEDs, which turns on the UV LED and leads to the complete chemical destruction of the dissolvable parts of memory devices (**Figure 3.15c**). Without this actuation, the memory data are preserved over $10^{6}$ s (inset of **Figure 3.15c**).

### 3.4.4 Materials for device fabrication

The 340 nm (100) p-type SOI wafer was purchased from Soitec (France), and spin-on-dopant (P509) for N-doping was purchased from Filmtronics (USA). The pure Cr and Mg pellet for thermal evaporation were purchased from Taewon Scientific Co., Ltd. (Korea). Cr and 99.99% ZnO:Mn (Mn contents: 3 wt%) sputter targets were purchased from Thifine (Korea).

### 3.4.5 Synthesis and characterization of IR806

IR806 was synthesized using previously reported method[22] All the reactions were performed under an Ar atmosphere using Schlenk-line techniques. IR780 iodide (0.75 mmol) was mixed with 4-mercaptobenzoic acid (1.50 mmol) in DMF (20 mL) by vigorous stirring at room temperature for 20 h. Then DMF was removed from the solution under vacuum. The residual product was dissolved in DCM (5 mL) and then filtered through a 0.45-μm PTFE syringe filter. Diethyl ether (150 mL) was slowly added to the filtered solution, and the purified and precipitated IR806 was retrieved by centrifugation.

### 3.4.6 Ligand exchange reaction of sensitizers I, II, and III on UCNPs

For multi-dye-sensitization of the UCNPs, the UCNPs in chloroform (3 mg/mL) were mixed with dyes (0.3 mg/mL) with various mixing ratios. Then the mixture was stirred under mild heating at 45 ºC for 15 h. The resulting solution was washed with acetonitrile (20 mL), and the product was retrieved by centrifugation. The washing process was repeated twice to completely remove free-standing unreacted dyes. The precipitated final product was successfully dispersed in chloroform.

### 3.4.7 Characterization of the UCNPs

TEM-2010 (JEOL, Japan) was used for collecting TEM images, and X-ray diffraction patterns ($2\theta$ scans) were obtained using an X-ray diffractometer (XRD, D/Max-3C, Rigaku, Japan) with Cu $K\alpha_1$ radiation ($\lambda$ = 1.5418 Å). Inductively coupled plasma atomic emission spectroscopy (ICPS-7500, Shimadzu, Japan) was used to measure the concentration of lanthanide ions in the UCNPs. $^1$H NMR spectra were recorded on an Avance-300 (Bruker, Germany).

### 3.4.8 Absorption/Emission spectra of multi-dye-sensitized UCNPs

For optical characterization, a UV/visible absorption spectrophotometer (Cary 5000, Agilent, USA) and photoluminescence spectrometer (FLS980, Edinburgh Photonics Ltd., UK) were used. Absorption spectra of UCNPs in chloroform or ethanol were obtained at the same scan rate of 600 nm/min. Photoluminescence spectra of UCNPs were obtained under the irradiation of a laser at an appropriate wavelength and power for each experiment. The 980 nm laser (MDL-III-980-1W) and 800 nm laser (MDL-III-800-1W) were purchased from CNI Laser (China), and the 517 nm laser (LVI-517-500mW) and 488 nm (LVI-488-150mW) laser were purchased from JMJ Korea (Korea). When needed, a short-pass filter was used to protect the detector from damage by scattered laser light. All the filters were purchased from Edmund Optics (USA). A quartz cuvette (Hellma, Germany) with light path of 10×10 mm was used for all the optical measurements.

### 3.4.9 Estimation of the total number of dye-sensitizers on a single UCNP

The total number of dye-sensitizers on a single UCNP was calculated using the concentration of substituted dye-sensitizers ($C_{ligand}$) divided by the

number density of nanoparticles ($C_{nanoparticle}$). The detailed calculation procedure is as follows. (i) Concentration of substituted dye-sensitizers ($C_{ligand}$): We assume that the absorption coefficient of the dyes does not change during the ligand exchange reaction. The photo-absorbance of the dye-sensitizers was measured using UV/vis spectroscopy. Dividing the measured absorbance by the molar absorption coefficient yielded the molar concentration of the dye-sensitizers bound to the UCNP surface ($C_{ligand}$). (ii) Number density of nanoparticle ($C_{nanoparticle}$): $C_{nanoparticle}$ in the solution was calculated by dividing the molar concentration of lanthanide ions (mM) ($C_{ion}$, calculated from inductively coupled plasma atomic emission spectroscopy results) by the number of lanthanide ions in a single nanoparticle ($N_{ion}$). $N_{ion}$ was calculated by dividing the average volume of nanoparticles (measured by TEM imaging) by the unit-cell-volume of hexagonal $NaYF_4$ (a = 0.596 nm, c = 0.353 nm) and multiplying it by 1.5 (the number of rare earth metals in a hexagonal unit cell). In case of multi-dye-sensitized nanoparticles, total number of dye-sensitizers on a single UCNP is calculated by summation of the number of each sensitizer.

### 3.4.10 Characterization of inter-ligand distances

To estimate the surface area of a UCNP, we measured the dimension of a

UCNP using TEM images. We assume that the size of every single nanoparticle is the same, and that the shape of a UCNP is a hexagonal prism. The area assigned for a dye-sensitizer was determined by dividing the obtained surface area of a UCNP by the number of dye-sensitizers bound to it. The average inter-ligand distance was then calculated by the taking square root of this value.

### 3.4.11 Measurement of time-dependent decay of emission and calculation of the energy transfer efficiency

The time-dependent decay of the emission of sensitizers I, II, and III was measured using the time-correlated single photon counting (TCSPC) method with a PicoHarp 300 photo-counting system (PicoQuant, USA). The measurements were conducted under 400 nm (for sensitizers I and II) and 500 nm (for sensitizers II and III). The dark count rates were $10^2$–$10^3$ photons per second, and the measurement count rates were $5\times10^4$ photons per second. The experiment was stopped when the photon counts reached 15000. The average lifetime was fitted using PicoHarp 300 software. The efficiency of energy transfer between two sensitizers was determined from the excited state lifetime of the donor sensitizer with/without the acceptor

sensitizer, $E = 1 - \frac{\tau(donor + acceptor)}{\tau(donor)}$. In case of weak fluorescence, the efficiency was calculated using the quantum yield of the donor sensitizer difference with/without the acceptor sensitizer, $E = 1 - \frac{F(donor + acceptor)}{F(donor)}$.

### 3.4.12 Fabrication of the destructible memory

A Cr thin film (~100 nm) was deposited by DC sputtering under an Ar atmosphere and patterned using photolithography with a S1805 photoresist (MicroChem, USA) and Cr etchant (Transene, USA). 5 cycles of $Al_2O_3$ (~1 nm) was deposited on the Cr bottom electrode (BE) using plasma-enhanced atomic layer deposition (PEALD). Then, SU-8 2000.5 (MicroChem, USA) was spin-coated and patterned on a 30 μm × 30 μm square-shaped *via* a hole array. A ZnO:Mn (Mn 3 wt%; Thifine, Korea) thin film (~5 nm) was sputtered using 50 W power under 15 mTorr Ar atmosphere. A 30 nm Mg TE was deposited by a thermal evaporator on the ZnO:Mn layer and then patterned using photolithography with a S1805 photoresist and Mg etchant (1% $HNO_3$, 24% water and 75% ethylene glycol).

### 3.4.13 Reliability tests (memory endurance, retention) of the memory

The reliability of the memory, the endurance was examined by repetitive voltage sweep from -2 to 1.5 V with current compliance of 300 μA for programming low-resistance state (LRS). Resistances of the high-resistance state (HRS) and LRS were measured at a read voltage of 30 mV, which exhibited stable operation (Figure S12a). For the retention characterization, set and reset processes were performed by voltage sweeping (0 to 1.5 V for set and 0 to -2 V for reset), and the current levels were read at 30 mV every 5 s (Figure S12b).

### 3.4.14 Fabrication of the Si transistor array

A $SiO_2$ doping mask layer was deposited on a p-type silicon-on-insulator (SOI) (340 nm top Si; Soitec, France) wafer using plasma-enhanced chemical vapor deposition (PECVD). Selected regions of the $SiO_2$ mask were patterned by photolithography and etched to define the doping area. P509 spin-on dopant (Filmtronics, USA) was spin-coated and annealed at 200 °C for 15 min and 975 °C for 1.5 min. After removing the $SiO_2$ doping mask and residual spin-on-dopant, the buried oxide of the SOI wafer was undercut etched using HF solution. The doped Si nano-membrane was then

transferred to a polyimide substrate (Poly(pyromellitic dianhydride-co-4,4′-oxydianiline) coating on $SiO_2$ substrate). The transferred Si nano-membrane was patterned and etched for electrical isolation between adjacent transistors. The gate dielectric (60 nm $SiO_2$) was deposited by PECVD and then patterned and etched to form source and drain windows. Then, Cr was deposited and patterned for the source, drain and gate electrodes. The solution of acid-generating layer containing UCNPs in chloroform is then spin-coated or dip-coated and annealed at 65 °C for 1 min. Finally, the device was picked up with a 3M tape and transferred to the desired substrate.

### 3.4.15 Preparation of acid-generating UCNP/PAG/PEO layer

The acid-generating layer was prepared by simple mixing of the UCNPs, PAG, and PEO. The PAG (20 mg), and PEO (40 mg) were dissolved in 1 g of the UCNP solution (10 mg/mL) and stirred overnight. The resulting mixed solution was spin- or dip-coated on the RRAM substrate and cured at 65 °C for 1 min. After the chemical dissolution, the sample was dipped in ethanol overnight to clean acid-generating layer for the electrical measurement.

### 3.4.16. Preparation of the TEM specimen for cross-sectional image of the integrated system

A Pt thin film or carbon protecting layer was deposited on the devices coated with the UCNP/PAG/PEO matrix by DC sputtering under an Ar atmosphere. Focused ion beam (SII NanoTechnology Inc., USA) methods for TEM sample preparation were used with $Ga^{3+}$ ion current under 30 kV. The sample was stored under vacuum condition before obtaining the TEM images.

## 3.5 References

The work in chapter 3 was published in *Advanced Materials (Advance Online Publication, DOI: 10.1002/adma.201603169)*


1 Liu, X., Yan, C.-H. & Capobianco, J. Photon upconversion nanomaterials. *Chem. Soc. Rev.* **44**, 1299-1301 (2015).

2 Wu, S., Han, G., Milliron, D. J., Aloni, S., Altoe, V., Talapin, D. V., Cohen, B. E. & Schuck, P. J. Non-blinking and photostable upconverted luminescence from single lanthanide-doped nanocrystals. *Proc. Nat. Acad. Sci.* **106**, 10917-10921 (2009).

3 Park, Y. I., Kim, J. H., Lee, K. T., Jeon, K.-S., Na, H. B., Yu, J. H., Kim, H. M., Lee, N., Choi, S. H., Baik, S.-I., Kim, H., Park, S. P., Park, B.-J., Kim, Y. W., Lee, S. H., Yoon, S.-Y., Song, I. C., Moon, W. K., Suh, Y. D. & Hyeon, T. Nonblinking and nonbleaching upconverting nanoparticles as an optical imaging nanoprobe and T1 magnetic resonance imaging contrast agent. *Adv. Mater.* **21**, 4467-4471 (2009).

4 Park, Y. I., Kim, H. M., Kim, J. H., Moon, K. C., Yoo, B., Lee, K. T., Lee, N., Choi, Y., Park, W., Ling, D., Na, K., Moon, W. K., Choi, S. H., Park, H. S., Yoon, S.-Y., Suh, Y. D., Lee, S. H. & Hyeon, T. Theranostic

probe based on lanthanide-doped nanoparticles for simultaneous *in vivo* dual-modal imaging and photodynamic therapy. *Adv. Mater.* **24**, 5755-5761 (2012).

5 Liu, Y., Chen, M., Cao, T., Sun, Y., Li, C., Liu, Q., Yang, T., Yao, L., Feng, W. & Li, F. A cyanine-modified nanosystem for *in vivo* upconversion luminescence bioimaging of methylmercury. *J. Am. Chem. Soc.* **135**, 9869-9876 (2013).

6 Liu, Q., Feng, W., Yang, T., Yi, T. & Li, F. Upconversion luminescence imaging of cells and small animals. *Nat. Protoc.* **8**, 2033-2044 (2013).

7 Chen, G., Qiu, H., Prasad, P. N. & Chen, X. Upconversion nanoparticles: Design, nanochemistry, and applications in theranostics. *Chem. Rev.* **114**, 5161-5214 (2014).

8 Idris, N. M., Gnanasammandhan, M. K., Zhang, J., Ho, P. C., Mahendran, R. & Zhang, Y. *In vivo* photodynamic therapy using upconversion nanoparticles as remote-controlled nanotransducers. *Nat. Med.* **18**, 1580-1585 (2012).

9 Yang, D., Ma, P. a., Hou, Z., Cheng, Z., Li, C. & Lin, J. Current advances in lanthanide ion ($Ln^{3+}$)-based upconversion nanomaterials for drug delivery. *Chem. Soc. Rev.* **44**, 1416-1448 (2015).

10 Yang, G., Yang, D., Yang, P., Lv, R., Li, C., Zhong, C., He, F., Gai, S. & Lin, J. A single 808 nm near-infrared light-mediated multiple imaging and photodynamic therapy based on titania coupled upconversion nanoparticles. *Chem. Mater.* **27**, 7957-7968 (2015).

11 Hososhima, S., Yuasa, H., Ishizuka, T., Hoque, M. R., Yamashita, T., Yamanaka, A., Sugano, E., Tomita, H. & Yawo, H. Near-infrared (NIR) up-conversion optogenetics. *Sci. Rep.* **5**, 16533 (2015).

12 Wu, X., Zhang, Y., Takle, K., Bilsel, O., Li, Z., Lee, H., Zhang, Z., Li, D., Fan, W., Duan, C., Chan, E. M., Lois, C., Xiang, Y. & Han, G. Dye-sensitized core/active shell upconversion nanoparticles for optogenetics and bioimaging applications. *ACS Nano* **10**, 1060-1066 (2016).

13 de Wild, J., Meijerink, A., Rath, J. K., van Sark, W. G. J. H. M. & Schropp, R. E. I. Upconverter solar cells: Materials and applications. *Energy Environ. Sci.* **4**, 4835-4848 (2011).

14 Lee, S.-M., Li, W., Dhar, P., Malyk, S., Wang, Y., Lee, W., Benderskii, A. & Yoon, J. High-performance flexible nanostructured silicon solar modules with plasmonically engineered upconversion medium. *Adv. Energy Mater.* **5**, 1500761 (2015).

15 Gargas, D. J., Chan, E. M., Ostrowski, A. D., Aloni, S., Altoe, M. V. P., Barnard, E. S., Sanii, B., Urban, J. J., Milliron, D. J., Cohen, B. E. &

Schuck, P. J. Engineering bright sub-10-nm upconverting nanocrystals for single-molecule imaging. *Nat. Nanotech.* **9**, 300-305 (2014).

16 Mi, Z., Zhang, Y., Vanga, S. K., Chen, C.-B., Tan, H. Q., Watt, F., Liu, X. & Bettiol, A. A. Subwavelength imaging through ion-beam-induced upconversion. *Nat. Commun.* **6,** 8832 (2015).

17 Xie, X., Gao, N., Deng, R., Sun, Q., Xu, Q.-H. & Liu, X. Mechanistic investigation of photon upconversion in $Nd^{3+}$-sensitized core–shell nanoparticles. *J. Am. Chem. Soc.* **135**, 12608-12611 (2013).

18 Gai, S., Li, C., Yang, P. & Lin, J. Recent progress in rare earth micro/nanocrystals: Soft chemical synthesis, luminescent properties, and biomedical applications. *Chem. Rev.* **114**, 2343-2389 (2014).

19 Li, X., Zhang, F. & Zhao, D. Lab on upconversion nanoparticles: Optical properties and applications engineering *via* designed nanostructure. *Chem. Soc. Rev.* **44**, 1346-1378 (2015).

20 Liu, B., Chen, Y., Li, C., He, F., Hou, Z., Huang, S., Zhu, H., Chen, X. & Lin, J. Poly(acrylic acid) modification of $Nd^{3+}$-sensitized upconversion nanophosphors for highly efficient UCL imaging and pH-responsive drug delivery. *Adv. Funct. Mater.* **25**, 4717-4729 (2015).

21 Chen, Y., Liu, B., Deng, X., Huang, S., Hou, Z., Li, C. & Lin, J. Multifunctional $Nd^{3+}$-sensitized upconversion nanomaterials for synchronous tumor diagnosis and treatment. *Nanoscale* **7**, 8574-8583 (2015).

22 Zou, W., Visser, C., Maduro, J. A., Pshenichnikov, M. S. & Hummelen, J. C. Broadband dye-sensitized upconversion of near-infrared light. *Nat. Photon.* **6**, 560-564 (2012).

23 Thompson, N. J., Wilson, M. W. B., Congreve, D. N., Brown, P. R., Scherer, J. M., Bischof, Thomas S., Wu, M., Geva, N., Welborn, M., Voorhis, T. V., Bulović, V., Bawendi, M. G. & Baldo, Marc A. Energy harvesting of non-emissive triplet excitons in tetracene by emissive PbS nanocrystals. *Nat. Mater.* **13**, 1039-1043 (2014).

24 Wu, X., Lee, H., Bilsel, O., Zhang, Y., Li, Z., Chen, T., Liu, Y., Duan, C., Shen, J., Punjabi, A. & Han, G. Tailoring dye-sensitized upconversion nanoparticle excitation bands towards excitation wavelength selective imaging. *Nanoscale* **7**, 18424-18428 (2015).

25 Wu, M., Congreve, D. N., Wilson, M. W. B., Jean, J., Geva, N., Welborn, M., Van Voorhis, T., Bulović, V., Bawendi, M. G. & Baldo, M. A. Solid-state infrared-to-visible upconversion sensitized by colloidal nanocrystals. *Nat. Photon.* **10**, 31-34 (2016).

26 Hwang, S.-W., Tao, H., Kim, D.-H., Cheng, H., Song, J.-K., Rill, E., Brenckle, M. A., Panilaitis, B., Won, S. M., Kim, Y.-S., Song, Y. M., Yu, K. J., Ameen, A., Li, R., Su, Y., Yang, M., Kaplan, D. L., Zakin, M. R., Slepian, M. J., Huang, Y., Omenetto, F. G. & Rogers, J. A. A physically transient form of silicon electronics. *Science* **337**, 1640-1644 (2012).

27 Uphoff, S., Holden, S. J., Le Reste, L., Periz, J., van de Linde, S., Heilemann, M. & Kapanidis, A. N. Monitoring multiple distances within a single molecule using switchable FRET. *Nat. Methods* **7**, 831-836 (2010).

28 Xu, S., Zhang, Y., Jia, L., Mathewson, K. E., Jang, K.-I., Kim, J., Fu, H., Huang, X., Chava, P., Wang, R., Bhole, S., Wang, L., Na, Y. J., Guan, Y., Flavin, M., Han, Z., Huang, Y. & Rogers, J. A. Soft microfluidic assemblies of sensors, circuits, and radios for the skin. *Science* **344**, 70-74 (2014).

29 Son, D., Lee, J., Qiao, S., Ghaffari, R., Kim, J., Lee, J. E., Song, C., Kim, S. J., Lee, D. J., Jun, S. W., Yang, S., Park, M., Shin, J., Do, K., Lee, M., Kang, K., Hwang, C. S., Lu, N., Hyeon, T. & Kim, D.-H. Multifunctional wearable devices for diagnosis and therapy of movement disorders. *Nature Nanotech.* **9**, 397-404 (2014).

30 Sekitani, T., Zschieschang, U., Klauk, H. & Someya, T. Flexible organic transistors and circuits with extreme bending stability. *Nat. Mater.* **9**, 1015-1022 (2010).

31 Sekitani, T., Yokota, T., Zschieschang, U., Klauk, H., Bauer, S., Takeuchi, K., Takamiya, M., Sakurai, T. & Someya, T. Organic nonvolatile memory transistors for flexible sensor arrays. *Science* **326**, 1516-1519 (2009).

32 Kim, J., Son, D., Lee, M., Song, C., Song, J.-K., Koo, J. H., Lee, D. J., Shim, H. J., Kim, J. H., Lee, M., Hyeon, T. & Kim, D.-H. A wearable multiplexed silicon nonvolatile memory array using nanocrystal charge confinement. *Sci. Adv.* **2,** e1501101 (2016).

33 Grispos, G., Storer, T. & Glisson, W. B. A comparison of forensic evidence recovery techniques for a windows mobile smart phone. *Digital Investigation*, **8**, 23-36 (2011)

34 Son, D., Lee, J., Lee, D. J., Ghaffari, R., Yun, S., Kim, S. J., Lee, J. E., Cho, H. R., Yoon, S., Yang, S., Lee, S., Qiao, S., Ling, D., Shin, S., Song, J.-K., Kim, J., Kim, T., Lee, H., Kim, J., Soh, M., Lee, N., Hwang, C. S., Nam, S., Lu, N., Hyeon, T., Choi, S. H. & Kim, D.-H. Bioresorbable electronic stent integrated with therapeutic nanoparticles for endovascular diseases. *ACS Nano* **9**, 5937-5946 (2015).

35 Bettinger, C. J. & Bao, Z. Organic thin-film transistors fabricated on resorbable biomaterial substrates. *Adv. Mater.* **22**, 651-655 (2010).

36 Huang, X., Liu, Y., Hwang, S.-W., Kang, S.-K., Patnaik, D., Cortes, J. F. & Rogers, J. A. Biodegradable materials for multilayer transient printed circuit boards. *Adv. Mater.* **26**, 7371-7377 (2014).

37 Kang, S.-K., Murphy, R. K. J., Hwang, S.-W., Lee, S. M., Harburg, D. V., Krueger, N. A., Shin, J., Gamble, P., Cheng, H., Yu, S., Liu, Z., McCall, J. G., Stephen, M., Ying, H., Kim, J., Park, G., Webb, R. C., Lee, C. H., Chung, S., Wie, D. S., Gujar, A. D., Vemulapalli, B., Kim, A. H., Lee, K.-M., Cheng, J., Huang, Y., Lee, S. H., Braun, P. V., Ray, W. Z. & Rogers, J. A. Bioresorbable silicon electronic sensors for the brain. *Nature* **530,** 71-76 (2016).

38 Hwang, S.-W., Park, G., Cheng, H., Song, J.-K., Kang, S.-K., Yin, L., Kim, J.-H., Omenetto, F. G., Huang, Y., Lee, K.-M. & Rogers, J. A. 25th anniversary article: Materials for high-performance biodegradable semiconductor devices. *Adv. Mater.* **26**, 1992-2000 (2014).

39 Selvin, P. R. The renaissance of fluorescence resonance energy transfer. *Nat. Struct. Mol. Biol.* **7**, 730-734 (2000).

40 Lakowicz, J. R. *Principles of fluorescence spectroscopy*, Ed.3, Chap. 13, Springer, New York, USA (2006)

41 Shen, J., Chen, G., Ohulchanskyy, T. Y., Kesseli, S. J., Buchholz, S., Li, Z., Prasad, P. N. & Han, G. Tunable near infrared to ultraviolet upconversion luminescence enhancement in (α-NaYF4:Yb,Tm)/$CaF_2$ core/shell nanoparticles for *in situ* real-time recorded biocompatible photoactivation. *Small* **9**, 3213-3217 (2013).

42 Kim, J., Lee, M., Shim, H. J., Ghaffari, R., Cho, H. R., Son, D., Jung, Y. H., Soh, M., Choi, C., Jung, S., Chu, K., Jeon, D., Lee, S.-T., Kim, J. H., Choi, S. H., Hyeon, T. & Kim, D.-H. Stretchable silicon nanoribbon electronics for skin prosthesis. *Nat. Commun.* **5** (2014).

43 Hernandez, H. L., Kang, S.-K., Lee, O. P., Hwang, S.-W., Kaitz, J. A., Inci, B., Park, C. W., Chung, S., Sottos, N. R., Moore, J. S., Rogers, J. A. & White, S. R. Triggered transience of metastable poly(phthalaldehyde) for transient electronics. *Adv. Mater.* **26**, 7637-7642 (2014).

# Chapter 4. High-resolution spin-on-patterning of perovskite thin films for optoelectronic device array.

## 4.1 Introduction

A pixel in the high-resolution optoelectronic device (*e.g.* Light emitting diode and photodiode) array is composed of an active electronic component and a photodetecting unit, which are generally made up of single-crystalline silicon. The ideal properties for a photodetecting unit, which determine the quality of the obtained images[1], include the high gain, low noise[2], infrared (IR) blindness[3], and tunable absorption[4-6]. The deformability of an image sensor array provides additional innovative advantages[7-9]. Although silicon is considered as one of the best materials for the current image sensor arrays, it has several drawbacks as a material for image sensing devices: i) A thick silicon active layer is required to absorb sufficient photons owing to the inefficient photoabsorption originated from its indirect bandgap nature. ii) The brittleness of a bulk silicon wafer and its high processing temperature make the fabrication of image sensor arrays on deformable substrates challenging. iii) The relatively high noise level decreases the signal-to-noise

ratio. iv) An IR-filter is required to remove the undesired signals by absorption of photons in the range of 750–1200 nm. v) Color filters are necessary to distinguish between red, green, and blue light. Compound semiconductors may partially solve these problems. However, they are much more expensive than silicon, although several novel processing approaches have lowered the cost.

Solution-processed perovskite thin film have attracted significant attention as efficient photo-absorption layer and promising alternatives to bulk silicon[10,11]. Compared to silicon photodetectors, perovskite photodetecting units show higher gains[12], lower noise levels[3,13], IR blindness[3], and tunable absorption[4-6]. Perovskite materials also allow for the low temperature fabrication on plastic substrates[14,15], which is important for future flexible devices[16,17], and for the production of cheaper modules than those based on silicon and compound semiconductors. Although perovskite solar cells have stability issues related to the humidity and temperature[10,11], perovskite photodetectors are quite free from these stability problems because image sensor arrays work under relatively moderate conditions compared to solar cells. Moreover, recent studies have reported a dramatic enhancement in the stability of perovskite optoelectronic devices[15,18].

Despite the above-mentioned extinctive properties, most of the solution-

processed perovskite thin film devices have demonstrated as large and bulk cells not as patterned arrays. The high-resolution patterning of the solution-processed thin film is necessary for electrical isolation between adjacent cells in the sensor array. Moreover, integration of patterned photodetecting unit[19,20] with the active component[21,22] has been highly demanded for individual cell addressing but challenging. This is mainly because of the instability of perovskite materials in almost all polar and protic solvents (*e.g.,* water, alcohol, acetone, and other solvents for photolithography.

Here, we report a novel high-resolution spin-on-patterning (SoP) process for perovskite thin films. The dewetting of the perovskite precursor solution during the spin-coating process enabled the simple but reliable patterning of perovskite thin films up to the resolution of 1 μm and below[23]. The SoP process was found to be compatible with various solution-processed perovskite deposition techniques reported so far[24-27] as well as the conventional microfabrication processes used for the mass production of image sensor arrays in the industry.

## 4.2 Result and Discussion

### 4.2.1. Characterization of spin-on-patterning of perovskite thin film

**Figures 4.1** i)–vi) illustrate the SoP process developed in this work. Briefly, i) a densely packed hydrophobic self-assembled monolayer (SAM; *e.g.*, *n*-octadecyltrichlorosilane (ODTS)) was deposited on the entire surface of oxide substrates (*e.g.,* $SiO_2$, $TiO_2$ and ITO). ii) The photoresist (PR; S1805, Microchem, USA) was spin-coated and patterned. The PR-patterned oxide substrate was then treated with the oxygen plasma using a reactive ion etcher (RIE) to selectively remove the SAM, expose the oxide, and make that region hydrophilic. The removal of the PR defined a pattern with two different surface energies (hydrophilic oxide region and hydrophobic SAM-modified region). Then, iii) the solution of perovskite precursors was spin-coated (**Figure 4.2a**), which iv) form a thin solution film (**Figure 4.2b**). v) The decrease in the solution thickness by the spin coating resulted in spontaneous dewetting of the solution from the hydrophobic region and its migration onto the hydrophilic region (**Figure 4.2c**). The residual solution was removed from the substrate by the centrifugal force. vi) Finally, the patterned solid-state perovskite film was obtained after thermal annealing (**Figure 4.2d**).

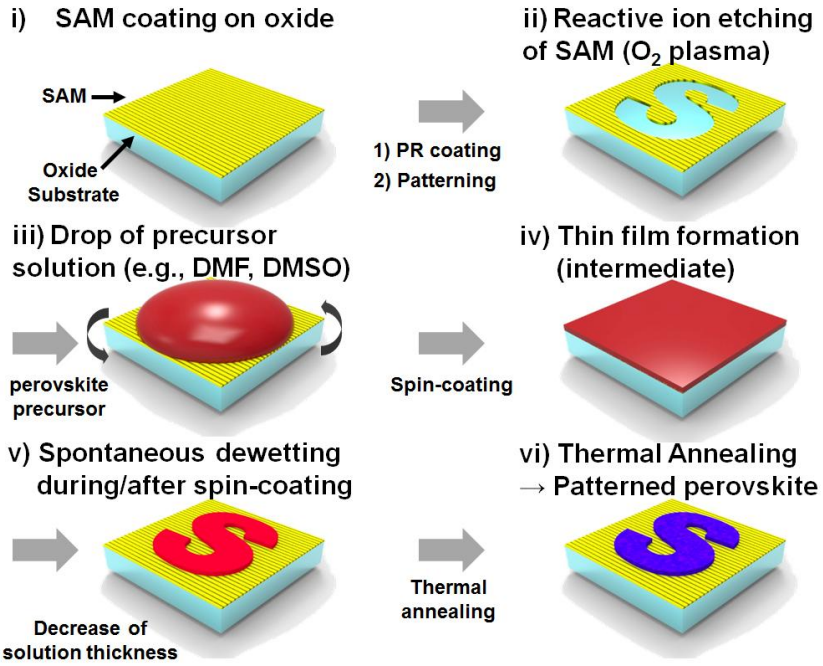


**Figure 4.1 Schematic illustration of the spin-on-patterning process**

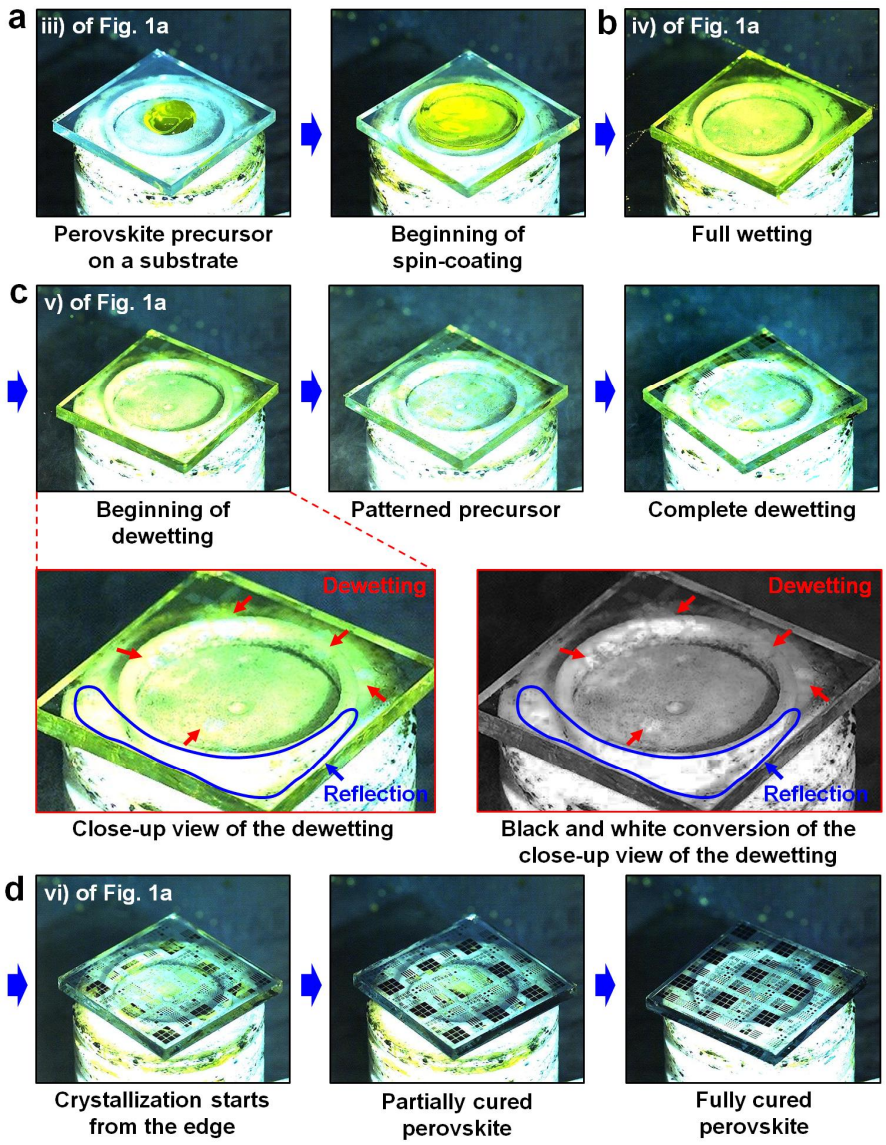


**Figure 4.2 Snapshot images at various states of the SoP process captured from a slow-motion video**

(a) Initial states, (b) full wetting state, (c) dewetting states, and (d) crystallization states.

Dimethylformamide (DMF), dimethylsulfoxide (DMSO), and γ-butyrolactone, which are responsible for the complete and partial wetting on the hydrophilic and hydrophobic surfaces, respectively, were used as the solvents for perovskite precursors (Contact angle measurements are in **Table 4.1**).

Examples of patterned perovskite films are shown in **Figure 4.3**. We chose $CH_3NH_3PbI_3$, which is a well-known inorganic–organic hybrid perovskite material, as a representative material. **Figures 4.3a** i)–iii) show the optical and scanning electron microscopy (SEM) images of the patterned perovskite film at different magnifications. **Figure 4.3a** iv) shows an atomic force microscopy (AFM) image of the patterned perovskite film (magnified view of the green dotted box in **Figure 4.3** iii)). The perovskite film was deposited only in the hydrophilic oxide region. The X-ray diffraction (XRD) peaks of the patterned and bulk perovskite films coincided, indicating that they had the same crystal structure (**Figure 4.4**). **Figure 4.3b** and its insets (magnified views) show the "line and space" patterns of the perovskite film. The line widths were between 600 nm and 20 μm.

**a, $TiO_2$ NPs-coated substrate**

| Contact angle | DMSO | DMF | γ-butyrolactone |
|---|---|---|---|
| **ODPA** | 68.3 | 47.55 | 55.22 |
| **ODTS** | 75.92 | 58.06 | 71.59 |
| **Oxygen plasma** | ~0 | ~0 | ~0 |

**b, ITO substrate**

| Contact angle | DMSO | DMF | γ-butyrolactone |
|---|---|---|---|
| **ODPA** | 63.9 | 44.22 | 47.26 |
| **ODTS** | 62.31 | 52 | 76.95 |
| **Oxygen plasma** | ~0 | ~0 | ~0 |

**c, $SiO_2$ substrate**

| Contact angle | DMSO | DMF | γ-butyrolactone |
|---|---|---|---|
| **ODPA** | 37.36 | 26.56 | 39.77 |
| **ODTS** | 76.96 | 59.56 | 67.19 |
| **Oxygen plasma** | ~0 | ~0 | ~0 |

**d, FTO substrate**

| Contact angle | DMSO | DMF | γ-butyrolactone |
|---|---|---|---|
| **ODPA** | 76.55 | 62.31 | 76.96 |
| **ODTS** | 73.63 | 68.3 | 74.88 |
| **Oxygen plasma** | ~0 | ~0 | ~0 |

**Table 4.1 Contact angle measurements of representative solvents (DMSO, DMF, and γ-butyrolactone) on various substrates treated by the ODPA (n-octadecylphosphonic acid), ODTS (n-octadecyltrichlorosilane), and oxygen plasma.**

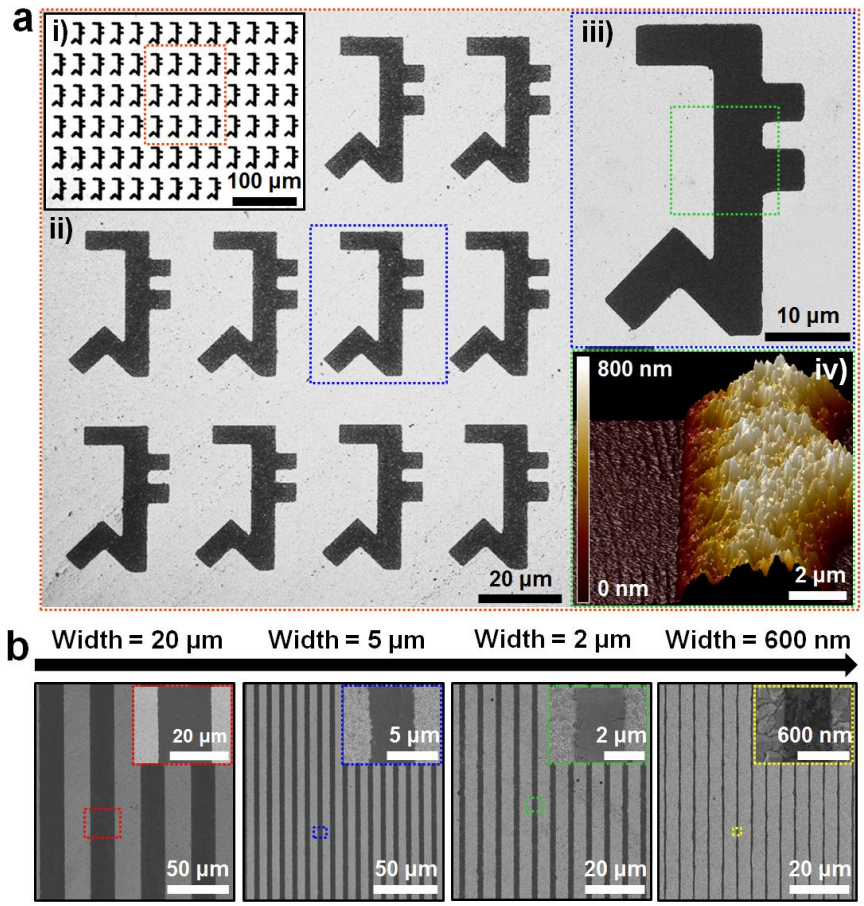


**Figure 4.3 Patterned perovskite thin film**

(a) i) Optical microscope image of the patterned perovskite film on an ITO substrate, ii) its magnified SEM image (red dotted box), iii) another magnified SEM view (blue dotted box), and iv) AFM image of the green dotted box. **c,** SEM images of the patterned perovskite films on an ITO substrate with different widths and spacings. The line pattern width ranges from 20 µm (left) to 600 nm (right). The insets show the magnified image of each dotted box.

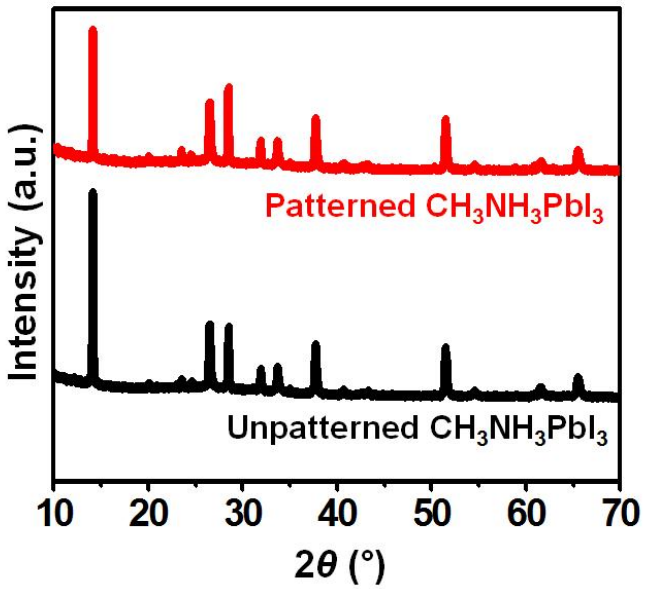


**Figure 4.4 X-ray diffraction (XRD) data of the patterned (red) and unpatterned (black) on the FTO substrate.**

### 4.2.2. Optimization and modelling of SoP process and patterned perovskite films

To maximize patterning yield of the desired shape (see Experimental section for the yield calculation), we optimized the SoP process by modulating the spin-coating rate and temperature of the perovskite precursor solution ($CH_3NH_3PbI_{3-x}Cl_x$ in DMF). The reason why we chose spin-coating rate and temperature for optimization factors is that the SoP process is fundamentally based on the time-dependent dewetting of the perovskite precursor solution during its spin-coating on the pre-patterned hydrophilic/hydrophobic surface. According to a simple 2D thermodynamic dewetting model, the spin-coating rate and temperature were revealed as important parameters, between which the spin-coating rate is a more dominant factor (**Figure 4.5a**). Almost all patterns (~95% yield) were successfully defined at low solution temperatures and high spin-coating rates.

The SoP process was analyzed using a thermodynamic dewetting model (**Figure 4.5b**). At the initial state, the entire surface is covered by thin liquid film with a height of $H'$. After the dewetting step, the liquid–vapor interfacial area per unit width increases by $2S - L_{SAM} - L_{OX}$ (**Figure 4.6a**). The liquid–solid interfacial area decreases by $L_{SAM}$, and the solid–vapor interfacial area

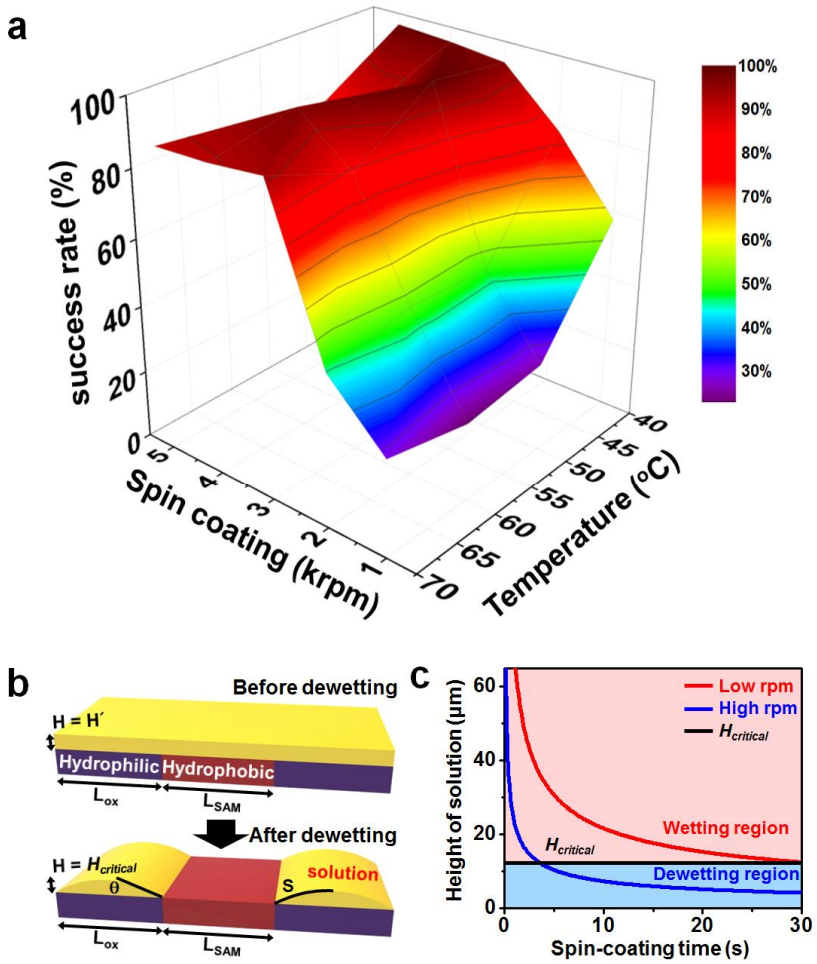


**Figure 4.5 Optimization and modelling of the SoP process.**

(a) Patterning yields at different spin-coating rates and solution temperatures on an SAM-patterned ITO substrate. (b) Schematic illustration of the dewetting model for the SoP process. (c) Plot of the height of the spin-coated solution versus the spin-coating time during the SoP process at a high (3,000 rpm) and low (1,000 rpm) spin-coating rate.

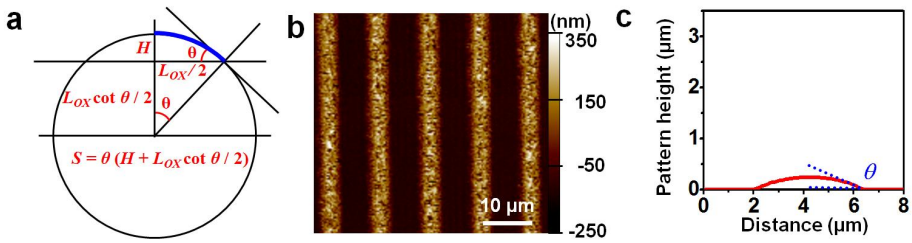


**Figure 4.6 Modelling of the SoP**

(a) Determination of $\boldsymbol{S}$ (blue) in terms of $\boldsymbol{H}$, $\boldsymbol{\theta}$ and $\boldsymbol{L_{ox}}$. (b) AFM image of 5 μm 'line and space' pattern. (c) Cross-sectional profile of the patterned perovskite film to determine $\boldsymbol{\theta}$.

increases by $L_{SAM}$. For a completely separated pattern, the total interfacial energy difference ($\Delta G_{dewet}$) per unit width during the dewetting step should be less than 0. Therefore,

$$(2S - L_{SAM} - L_{OX})E_{LV} - L_{SAM}E_{LS} + L_{SAM}E_{SV} \Delta G_{dewet} \leq 0 \quad \text{(Eq.1)}$$

where $E_{LV}$, $E_{LS}$, and $E_{SV}$ are the liquid–vapor, liquid–solid, and solid–vapor interfacial energies, respectively. In this modified dewetting model, $S$ can be expressed as a function of the contact angle at the hydrophilic surface ($\theta$), the length of the hydrophilic region ($L_{OX}$), the length of the hydrophobic region ($L_{SAM}$), the height of the solution ($H$), and the contact angle at the hydrophobic surface $\beta$. By using the Taylor series of $\cot\theta$ ($\theta$ is defined in **Figure 4.6a** and calculated from the height profile measured from the atomic force microscope; **Figure 4.6b** and **Figure 4.6c**),

$$2S = 2\theta H + L_{OX}\theta\cot\theta \quad 2\theta H + L_{OX} - \frac{1}{3}\theta^2 L_{OX} \quad \text{(Eq. 2)}$$

Substitute this into Eq. 1 to get

$$2\theta H - L_{SAM} - \frac{1}{3}\theta^2 L_{OX} \leq -L_{SAM}\cos\beta \quad \text{(Eq. 3)}$$

The height when Eq. 3 meets the equivalence can be defined as the critical dewetting height ($H_{critical}$), Eq. 3 can be modified as:

$$H \le \frac{(1-\cos\beta)L_{SAM} + \frac{1}{3}\theta^2 L_{OX}}{2\theta} = H_{critical} \quad \text{(Eq. 4)}$$

Meanwhile, the height of the solution decreases with time during the SoP process. We employed a theoretical spin-coating model,

$$H = h_0\left(1 + \frac{4h_0^2\rho w^2 t}{3\eta}\right)^{-\frac{1}{2}} \text{(Eq. 5)}$$

By combining Eqs. 4 and 5, we can state that the dewetting step occurs when the height of the solution is lower than the critical dewetting height (**Figure 4.5c**). In the case of the high spin-coating rate, the thickness of the solution reaches the critical dewetting thickness quickly, and therefore, the yield increases. The subsequent annealing of the solution produces the patterned film.

Figure 2c shows the plot of the solution height versus time in the case of $L_{OX}$ = 5 μm, $L_{SAM}$ = 5 μm, $\theta$ = 8°, and $\beta$ = 70°. For the calculation of the height of the solution during the spin coating, we assumed an initial solution volume of 50 μL, a solution density of $1.1 \times 10^3$ kg/m$^3$, a viscosity of $1.99 \times 10^{-3}$ kg/m·s, and a low rpm of 1,000 rpm and a high rpm of 3,000 rpm.

As thickness of the coated solution decreases below the critical solution thickness ($H_{critical}$; **Figure 4.5c**), the dewetting occurs spontaneously to minimize the total surface energy during the spin-coating process. Under

critical thickness, surface energy reaches critical value, which results in a transition from wetting to dewetting. As the rate of spin-coating increases, the film thickness reaches the critical dewetting thickness more rapidly, thus making the dewetting easier. This tendency corresponds to the experimental results, *i.e.* higher patterning yields at faster spin-coating rates (**Figure 4.5a**).

The local grain diameter of the patterned perovskite film depended mainly on deposition methods and the distance from the pattern edge. In case of the hot casting method, which induces large grain growth, the average diameter of the grains increased linearly until the distance from the pattern edge reached 5 μm and remained constant at distances greater than 5 μm (**Figure 4.7a**). In the case of the mixed-precursor deposition method, on the other hand, which induces the growth of smaller grains the average diameter of the grains was less dependent on the distance from the pattern edge. In addition to deposition method, as the distance from the pattern edge increases, the average diameter of the grains increases and becomes steady. Upon dewetting, the precursor solution was confined within the hydrophilic region and formed an arch-like shape (**Figure 4.6c**). The volume of the precursor solution at the pattern edge was thereby smaller than that at the center of the pattern, which resulted in insufficient grain growth. Accordingly, the average grain size decreased, as the area of the small square-shaped patterns (area < 2,500 $\mu m^2$) decreased,

owing to the edge effect, while the average grain size in the large patterns (area > 2,500 $\mu m^2$) was independent of the pattern area (**Figure 4.7b**).

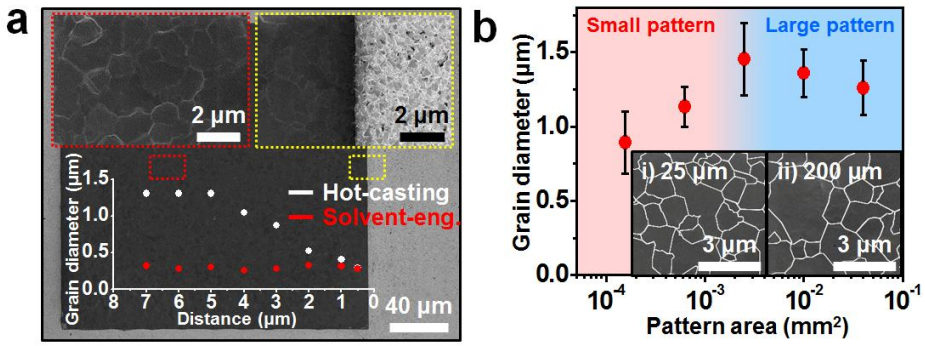


**Figure 4.7 Effect of the distance from the pattern edge and the pattern area on the grain size**

(a) Effect of the distance from the pattern edge on the grain size by using hot-casting method (white) and solvent engineering method (red). The blue dotted box (left) corresponds to the center of a square pattern, and the yellow dotted box (right) corresponds to the pattern edge. (b) Effect of the area of the square patterns on the average grain diameter. The insets show the grain shape of the square patterns with the areas of i) 25×25 $\mu m^2$ and ii) 200×200 $\mu m^2$.

### 4.2.3. Fabrication of patterned perovskite photodiode by the SoP process

Based on the optimized patterning technique, we fabricated patterned perovskite photodiode array employing the device structure compatible with low temperature processes[29] (**Figure 4.8a**). The ITO and Au film served as a bottom and top electrode (BE and TE) of the perovskite photodiode, respectively. Uniformly spin-coated Y doped $TiO_2$ (Y:$TiO_2$) NPs were used as an electron transport layer, spiro-OMeTAD was used as a hole transport layer, and a 150 nm $CH_3NH_3PbI_3$ film was used as a photo-absorption layer. The device showed typical characteristics of a photodiode (**Figure 4.8b**). The energy level of each layer is appropriate for photo-absorbing devices (**Figure 4.9**). **Figure 4.8b** shows the current density–voltage (*J–V*) characteristics of the patterned (blue) and unpatterned (red) perovskite device, measured under the dark (off) and illuminated (on; AM1.5G, 100 mA $cm^{-2}$) conditions. The on/off ratio, rectification ratio, and dark current density of the patterned perovskite photodiode at −1.5 V were $1.0 \times 10^3$, $3.1 \times 10^2$, and $1.1 \times 10^{-2}$ $mA/cm^2$, respectively. The *J-V* characteristics and frequency response of the perovskite photodiode are appropriate for the image sensor applications[30] (**Figure 4.10**).

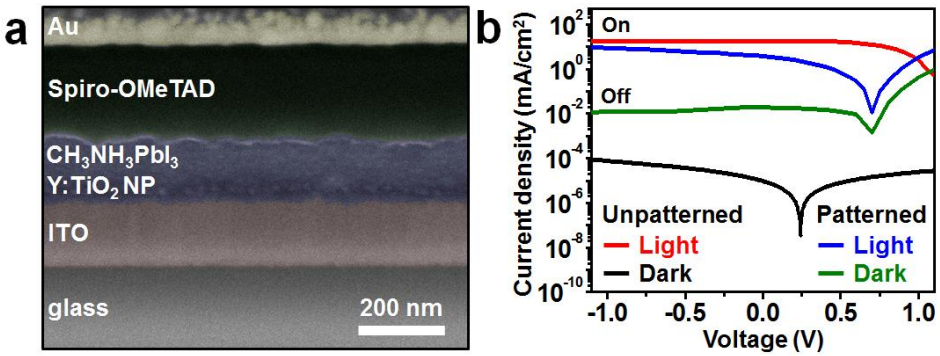


**Figure 4.8 Patterned perovskite photodiode**

(a) Cross-sectional SEM image of the perovskite photodiode. (b) Current density–voltage (*J–V*) plot of the patterned and unpatterned perovskite photodiodes under the illuminated (On) and dark (Off) conditions.

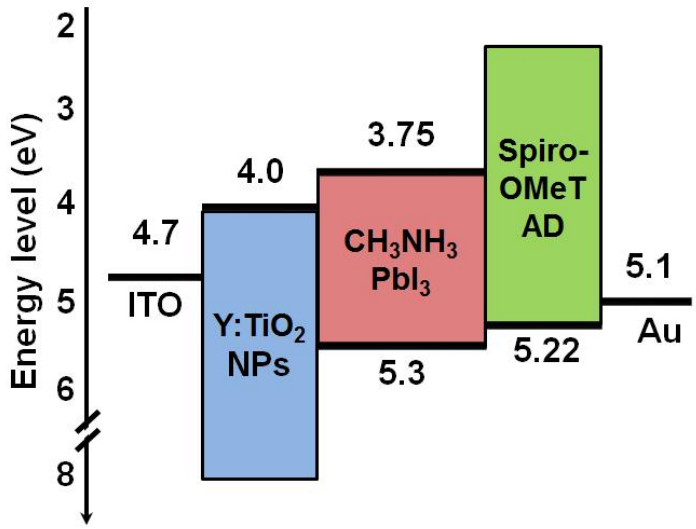


**Figure 4.9 Energy level diagram of the patterned perovskite photodiode**

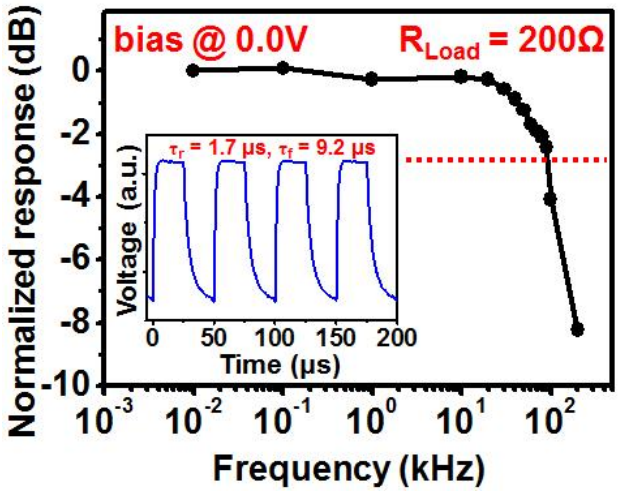


**Figure 4.10 Frequency response of the patterned perovskite photodiode**

Upper red dot line shows a valid range of perovskite photodetector, where normalized response is less than -1 dB. The transient photocurrent change at the frequency of 20 kHz is shown in the inset.

Notably, the patterned perovskite photodiode exhibited much higher current density than theoretical value of the single-crystalline silicon device with the same thickness (**Figure 4.11**) because of its higher photo-absorption coefficient[10]. Additionally, perovskite photodiodes based on different halide compositions can be used for the filter-less and color-tunable photodetectors[4,5] without the IR noise. The absorption edge can be tuned from ~790 nm ($CH_3NH_3PbI_3$) to ~450 nm ($CH_3NH_3PbBrCl_2$), which correspond to the IR and blue light (**Figure 4.12a**), respectively[31]. The device made up of $CH_3NH_3PbI_3$ absorbs photons in the entire visible range and is responsive to the red, green, and blue light, while that based on $CH_3NH_3PbBr_2Cl$ showed responses only to the green and blue light (**Figure 4.12b**). The device based on $CH_3NH_3PbBrCl_2$ was selectively responsive to the blue light (**Figure 4.12b**). All the devices show minimal IR noise.

## 4.3 Conclusion

The SoP process proposed in this work enabled a facile, reliable, and high-resolution patterning of inorganic–organic hybrid perovskite thin films. The developed process could be applied to a variety of mixed halide perovskite materials formed by various solution-processed deposition methods on different types of substrates. By using this SoP process, we successfully developed a perovskite-based patterned photodiode array featured with the high-performance, ultrathin thickness, lightweight, and deformable characteristics. Based on the results obtained in this study, we state that the SoP process has a high potential to become a versatile tool for fabricating perovskite-based high-resolution optoelectronic device arrays, such as the next-generation image sensors, light emitting diodes, and micro-solar cells.

## 4.4 Experimental

### 4.4.1 Materials and Methods

All the materials were used as purchased unless stated. The ITO glass (10 $\Omega/cm^2$, 0.7 mm thick, transmittance >85%) was purchased from SJ (Korea). The FTO glass was purchased (7 $\Omega/cm^2$, 2.2 mm thick, transmittance >81%) from WooyangGMS (Korea). Yttrium chloride (99.99%), titanium diisopropoxide bis(acetylacetonate) (~75 wt.% in IPA), titanium chloride (>99.995%), lead chloride (99.999%), *n*-octadecyltrichlorosilane (>90%), *n*-octadecylphosphonic acid (~97%), hydrobromic acid (~48%), hydrochloric acid (~37%), hydriodic acid (~57 wt.% in water), bis(trifluoromethane)-sulfonimide lithium salt (>99.95%), and 4-*tert*-Butylpyridine (96%) were purchased from Sigma Aldrich (USA). *n*-octyltrichlorosilane (97%), *n*-decyltrichlorosilane (97 %), *n*-dodecyltrichlorosilane (96%), lead iodide (99.999%), and lead bromide (99.999%) were purchased from Alfa Aesar (USA). Methylamine (~40.0 to 43.0%) was purchased from Tokyo chemical industry (Japan), and spiro-OMeTAD (> 99.9%) was purchased from Merck (Germany).

### 4.4.2 Synthesis of $TiO_2$ and Y:$TiO_2$ NPs

The synthesis of the $TiO_2$ and Y:$TiO_2$ NPs were carried out according to the

previous report[26]. The reaction proceeded under $N_2$ atmosphere in the glove box. The $YCl_3$ powder was dissolved in 2 mL of absolute ethanol and stirred at 80 °C. Then, 0.5 mL $TiCl_4$ was slowly injected into the vial and 10 mL benzyl alcohol was added in sequence. The solution was constantly heated at 80 °C and stirred for 8 h until a milky suspension was obtained. The $TiO_2$ NPs were synthesized by following the same procedure without the addition of $YCl_3$. 12 mL diethyl ether was added to 1 mL of the resulting solution. The reaction mixture was centrifuged at 4,000 rpm for 10 min. The precipitate was dissolved into the desired amount of absolute ethanol. 1.5% v/v of titanium diisopropoxide bis(acetylacetonate) was added to the resulting solution before using it.

### 4.4.3 Synthesis of inorganic–organic hybrid perovskite materials

To synthesize $CH_3NH_3I$, 20 mL methylamine solution was injected into an argon filled 250 mL round-bottom flask and put on the ice bath. An equimolar solution of hydriodic acid was slowly injected into the flask, and the mixed solution was then stirred at 0 °C for 4 h. The solvent was then removed using a rotary evaporator yielding a white precipitate. The precipitate was dissolved in 100 mL absolute ethanol, and a small amount of diethyl ether was slowly added into the solution. The solution was cooled down to 20 °C for the growth

of $CH_3NH_3I$ crystals. After 3 days, white $CH_3NH_3I$ crystals were obtained, filtered, and dried under vacuum at 60 °C for 48 h. For the synthesis of $CH_3NH_3Br$ and $CH_3NH_3Cl$, equimolecular solutions of hydrobromic acid and hydrochloric acid were used instead of hydriodic acid, respectively, and the other steps were exactly the same as those for the synthesis of $CH_3NH_3I$.

### 4.4.4 Electrical characterization of the device

All the device measurements were carried out at 20 °C and 20% humidity. The current density–voltage (*J–V*) characteristics of the photodiode were measured by using a semiconductor device parameter analyzer, Keithley 2400 (Tektronix, USA) or a B1500A (Agilent, USA) under the light incidence of 100 mW/cm$^2$, AM 1.5 G illumination with solar simulator (Newport, USA).

### 4.4.5 Optical, structural, and morphological characterization of the perovskite film

The diffuse reflectance spectra were collected using a Cary 5000 UV-Vis-NIR spectrophotometer (Varian, USA). The XRD spectra were obtained using a D8 Advance X-ray diffractometer (Bruker, USA) with an operating voltage of 40 kV. The surface morphology of the film was measured using a field emission scanning electron microscope (FE-SEM, JSM-6330F, JEOL, Japan)

in SE2 mode and SE1 mode using an in-lens detector. Atomic force microscope (AFM, Dimension Icon, Bruker, USA) in tapping and non-contact mode was also used for topographic measurements. The cross-sectional structure of the photodiode was obtained using an FE-SEM equipped with a focused ion beam system (Helios 650, FEI, USA).

### 4.4.6 Measurement of contact angles of solvents on oxide substrates

To prepare a substrate coated with the $TiO_2$ NPs, the solution of $TiO_2$ NPs was spin-coated on a bare glass at 3,000 rpm for 30 s and annealed at 120 °C for 30 min. The NPs were coated onto the glass substrate and forms a uniform film. The oxide substrates such as ITO, $SiO_2$, FTO, and $TiO_2$ NP film were deposited and coated on the glass and washed with DI water, IPA, acetone, and chloroform in sequence. They were then treated with an oxygen plasma using RIE ($O_2$, 100 sccm, 0.1 Torr, 1 min) for 30 min. The contact angles of dimethyl sulfoxide (DMSO), dimethylformamide (DMF), and γ-butyrolactone on the **a,** $TiO_2$ NPs, **b,** ITO, **c,** $SiO_2$, and **d,** FTO substrate which were treated with UV/ozone, *n*-octadecylphophonic acid (ODPA) or *n*-octadecyltrichlorosilane (ODTS) were measured by the charge-coupled device (CCD) camera.

### 4.4.7 Determination of the grain diameter by using the American Society for Testing and Materials (ASTM) intercept procedure

The average diameters of the grains were calculated by the ASTM E112 intercept procedure. The grain diameter varied exponentially with the grain size number ( $G$ ) according to Eq. 6 given below

$$G = 6.643856 \log_{10} \frac{P_i}{L/M} - 3.288 \quad \text{(Eq. 6)}$$

where $G$ is the grain size number, $P_i$ is the total number of intercepts of one random line, $L$ is the length of the test line, and $M$ is the magnification of the obtained image.

## 4.5 References


1 Fossum, E. R. CMOS image sensors: electronic camera-on-a-chip. *IEEE Trans. Elec. Dev.* **44**, 1689-1798 (1997).

2 Koppens, F. H. L., Mueller, T., Avouris, P., Ferrari, A. C., Vitiello, M. S. & Polini, M. Photodetectors based on graphene, other two-dimensional materials and hybrid systems. *Nat. Nanotech.* **9**, 780-793 (2014).

3 Lin, Q., Armin, A., Lyons, D. M., Burn, P. L. & Meredith, P. Low noise, IR-blind organohalide perovskite photodiodes for visible light detection and imaging. *Adv. Mater.* **27**, 2060-2064 (2015).

4 Lin, Q., Armin, A., Burn, P. L. & Meredith, P. Filterless narrowband visible photodetectors. *Nat. Photon.* **9**, 687-694 (2015).

5 Fang, Y., Dong, Q., Shao, Y., Yuan, Y. & Huang, J. Highly narrowband perovskite single-crystal photodetectors enabled by surface-charge recombination. *Nat. Photon.* **9**, 679-686 (2015).

6 Sutter-Fella, C. M., Li, Y., Amani, M., Ager, J. W., Toma, F. M., Yablonovitch, E., Sharp, I. D. & Javey, A. High photoluminescence quantum yield in band gap tunable bromide containing mixed halide perovskites. *Nano Lett.* **16**, 800-806 (2016).

7 Ko, H. C., Stoykovich, M. P., Song, J., Malyarchuk, V., Choi, W. M., Yu, C.-J., Geddes Iii, J. B., Xiao, J., Wang, S., Huang, Y. & Rogers, J. A. A

hemispherical electronic eye camera based on compressible silicon optoelectronics. *Nature* **454**, 748-753 (2008).

8 Jung, I., Xiao, J., Malyarchuk, V., Lu, C., Li, M., Liu, Z., Yoon, J., Huang, Y. & Rogers, J. A. Dynamically tunable hemispherical electronic eye camera system with adjustable zoom capability. *Proc. Nat. Acad. Sci.* **108**, 1788-1793 (2011).

9 Song, Y. M., Xie, Y., Malyarchuk, V., Xiao, J., Jung, I., Choi, K.-J., Liu, Z., Park, H., Lu, C., Kim, R.-H., Li, R., Crozier, K. B., Huang, Y. & Rogers, J. A. Digital cameras with designs inspired by the arthropod eye. *Nature* **497**, 95-99 (2013).

10 Green, M. A., Ho-Baillie, A. & Snaith, H. J. The emergence of perovskite solar cells. *Nat. Photon.* **8**, 506-514 (2014).

11 Gao, P., Gratzel, M. & Nazeeruddin, M. K. Organohalide lead perovskites for photovoltaic applications. *Energy Environ. Sci.* **7**, 2448-2463 (2014).

12 Dou, L., Yang, Y., You, J., Hong, Z., Chang, W.-H., Li, G. & Yang, Y. Solution-processed hybrid perovskite photodetectors with high detectivity. *Nat. Commun.* **5** (2014).

13 Fang, Y. & Huang, J. Resolving weak light of sub-picowatt per square centimeter by hybrid perovskite photodetectors enabled by noise

reduction. *Adv. Mater.* **27**, 2804-2810 (2015).

14 Docampo, P., Ball, J. M., Darwich, M., Eperon, G. E. & Snaith, H. J. Efficient organometal trihalide perovskite planar-heterojunction solar cells on flexible polymer substrates. *Nat. Commun.* **4** (2013).

15 Kaltenbrunner, M., Adam, G., Glowacki, E. D., Drack, M., Schwodiauer, R., Leonat, L., Apaydin, D. H., Groiss, H., Scharber, M. C., White, M. S., Sariciftci, N. S. & Bauer, S. Flexible high power-per-weight perovskite solar cells with chromium oxide-metal contacts for improved stability in air. *Nat. Mater.* **14**, 1032-1039 (2015).

16 Kaltenbrunner, M., Sekitani, T., Reeder, J., Yokota, T., Kuribara, K., Tokuhara, T., Drack, M., Schwodiauer, R., Graz, I., Bauer-Gogonea, S., Bauer, S. & Someya, T. An ultra-lightweight design for imperceptible plastic electronics. *Nature* **499**, 458-463 (2013).

17 Sekitani, T., Zschieschang, U., Klauk, H. & Someya, T. Flexible organic transistors and circuits with extreme bending stability. *Nat. Mater.* **9**, 1015-1022 (2010).

18 Bella, F., Griffini, G., Correa-Baena, J.-P., Saracco, G., Grätzel, M., Hagfeldt, A., Turri, S. & Gerbaldi, C. Improving efficiency and stability of perovskite solar cells with photocurable fluoropolymers. *Science* (**advanced online publication**) (2016) DOI: 10.1126/science.aah4046.

19 Briseno, A. L., Mannsfeld, S. C. B., Ling, M. M., Liu, S., Tseng, R. J., Reese, C., Roberts, M. E., Yang, Y., Wudl, F. & Bao, Z. Patterning organic single-crystal transistor arrays. *Nature* **444**, 913-917 (2006).

20 Liu, S., Becerril, H. A., LeMieux, M. C., Wang, W. M., Oh, J. H. & Bao, Z. Direct patterning of organic-thin-film-transistor arrays via a "Dry-Taping" approach. *Adv. Mater.* **21**, 1266-1270 (2009).

21 Someya, T., Kato, Y., Shingo, I., Noguchi, Y., Sekitani, T., Kawaguchi, H. & Sakurai, T. Integration of organic FETs with organic photodiodes for a large area, flexible, and lightweight sheet image scanners. *IEEE Trans. Elec. Dev.* **52**, 2502-2511 (2005).

22 Fan, Z., Ho, J. C., Jacobson, Z. A., Razavi, H. & Javey, A. Large-scale, heterogeneous integration of nanowire arrays for image sensor circuitry. *Proc. Nat. Acad. Sci.* **105**, 11066-11070 (2008).

23 Spivak, A., Teman, A., Belenky, A., Yadid-Pecht, O. & Fish, A. Low-voltage 96 dB snapshot CMOS image sensor with 4.5 nW power dissipation per pixel. *Sensors* **12**, 10067 (2012).

24 Kojima, A., Teshima, K., Shirai, Y. & Miyasaka, T. Organometal halide perovskites as visible-light sensitizers for photovoltaic cells. *J. Am. Chem. Soc.* **131**, 6050-6051 (2009).

25 Burschka, J., Pellet, N., Moon, S.-J., Humphry-Baker, R., Gao, P.,

Nazeeruddin, M. K. & Gratzel, M. Sequential deposition as a route to high-performance perovskite-sensitized solar cells. *Nature* **499**, 316-319 (2013).

26 Jeon, N. J., Noh, J. H., Kim, Y. C., Yang, W. S., Ryu, S. & Seok, S. I. Solvent engineering for high-performance inorganic–organic hybrid perovskite solar cells. *Nat. Mater.* **13**, 897-903 (2014).

27 Nie, W., Tsai, H., Asadpour, R., Blancon, J.-C., Neukirch, A. J., Gupta, G., Crochet, J. J., Chhowalla, M., Tretiak, S., Alam, M. A., Wang, H.-L. & Mohite, A. D. High-efficiency solution-processed perovskite solar cells with millimeter-scale grains. *Science* **347**, 522-525 (2015).

# Bibliography

**1. Ultra-Wideband Multi-Dye-Sensitized Upconverting Nanoparticles for Information Security Application**

**Jongha Lee**[⊥], Byeongjun Yoo[⊥], Hakyong Lee[⊥], Gi Doo Cha, Hee-Su Lee, Youngho Cho, Sang Yeon Kim, Hyunseon Seo, Woongchan Lee, Donghee Son, Myungjoo Kang, Hyung Min Kim, Yong Il Park, Taeghwan Hyeon*, Dae-Hyeong Kim* ([⊥]equal contribution)

*Advanced Materials (Advanced Online Publication, DOI: 10.1002/adma.201603169)*

**2. Bioresorbable Electronic Stent Integrated with Therapeutic Nanoparticles for Endovascular Diseases**

Donghee Son[⊥], **Jongha Lee**[⊥], Dong Jun Lee, Roozbeh Ghaffari, Sumin Yun, Seok Joo Kim, Ji Eun Lee, Hye Rim Cho, Soonho Yoon, Shixuan Yang, Seunghyun Lee, Shutao Qiao, Daishun Ling, Sanghun Shin, Jun-Kyul Song, Jaemin Kim, Taeho Kim, Hakyong Lee, Jonghoon Kim, Min Soh, Nohyun Lee, Cheol Seong Hwang, Sangwook Nam, Nanshu Lu, Taeghwan Hyeon*, Seung Hong Choi*, and Dae-Hyeong Kim*, ([⊥]equal contribution)

*ACS Nano*, 9, 5937-5946 (2015)

**3. Multifunctional Wearable Devices for Diagnosis and Therapy of Movement Disorders**

Donghee Son[⊥], **Jongha Lee[⊥]**, Shutao Qiao, Roozbeh Ghaffari, Jaemin Kim, Ji Eun Lee, Changyeong Song, Seok Joo Kim, Dong Jun Lee, Samuel Woojoo Jun, Shixuan Yang, Minjoon Park, Jiho Shin, Kyungsik Do, Mincheol Lee, Kwanghun Kang, Cheol Seong Hwang, Nanshu Lu, Taeghwan Hyeon*, and Dae-Hyeong Kim* ([⊥]equal contribution)

*Nature Nanotechnology*, 9, 397-404 (2014) (Highlights in *nature*)

# 초 록 (Abstract in Korean)

## 삽입형 의료 장치 및 광전자 소자를 위한 차세대 유연 물질의 설계와 제작

최근 개발된 유연 전자 소자는 바이오메디컬 및 광전자 분야에 있어 기존의 단단하고 휘어지지 못하는 전자 소자들로는 구현할 수 없는 새로운 형태의 응용 가능성을 열었다. 기존의 전자 기기들과 달리, 유연 전자 소자는 구불구불한 생체 표면 위에서도 높은 정확도로 전기 신호를 측정할 수 있으며 광전자 소자 자체가 휘어짐으로써 들어오는 빛을 조절할 수 있는 가능성을 지닌다. 본 논문에서는 생흡수성 및 페로브스카이트 물질의 설계와 합성을 통해 유연 바이오메디컬 소자 및 광전자소자를 제작하는 것을 목표로 한다. 먼저, 기존의 치료 방법으로는 치료하기 어려웠던 악성 뇌교종 치료를 위한 생흡수성 소자에 대해 다룬다. 이러한 소자는 무선 히터, 온도 센서 및 약물 전달 패치로 이루어져 있으며 뇌 표면에 임플란트되어 지엽적이고, 투과적이며 조절 가능한 약물 전달을 가능하게 한다. 이러한 생흡수성 전자 소자의 제작 기술을 넓은 범위의 빛 자극에 의해 저장되어 있는 데이터가 지워질 수

있는 정보 보안을 위한 소자에 대해 보고한다. 이러한 시스템은 저항 메모리를 업컨버젼 나노입자 및 광산 발생제를 통합함으로써 제시될 수 있으며 방위 산업 또는 프라이버시 보호 소자로 활용될 수 있다. 마지막 목표는 위의 소자 제작 기술을 기반으로 한 유무기 하이브리드 페로브스카이트 패터닝이다. 유무기 하이브리드 페로브스카이트는 빛에 매우 민감하게 반응하며, 이 때 생성된 전자 및 정공의 모빌리티가 높아 기존의 실리콘을 대체할 수 있는 물질로 각광 받고 있다. '스핀온패터닝'이라는 새로운 기술의 개발을 통해 유기 용매상에서 불안정하여 포토리소그래피를 통해 패터닝할 수 없었던 페로브스카이트 박막을 패터닝하는데 성공하였다. 이러한 패턴된 페로브스카이트 박막을 활용하여 패턴된 포토다이오드를 제작하는 데 성공하였으며, 이는 페로브스카이트를 활용한 매우 얇은 이미지 센서 어레이의 개발에 활용될 수 있다.

**주요어: 유연한, 전자 소자, 생흡수성, 바이오메디컬, 임시적인, 페로브스카이트**

**학 번:** 2012-31300